UNIVERSITY OF EXETER

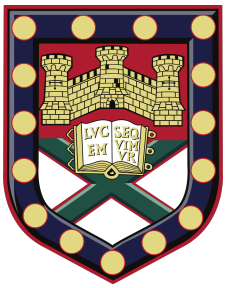

DOCTORAL THESIS

Strong Coupling of Molecular Vibrational Resonances

Author:

Kishan S. Menghrajani

Supervisors:

Prof. William L. Barnes

Prof. Geoffrey R. Nash

A thesis submitted in fulfillment of the requirements

for the degree of Doctor of Philosophy

August 2019

Declaration of Authorship

This thesis titled 'Strong Coupling of Molecular Vibrational Resonances' was submitted by MENGHRAJANI KISHAN S to the University of Exeter in fulfilment of the requirements for the degree of Doctor of Philosophy, in August 2019.

This thesis is available for Library use on the understanding that it is copyright material and that no quotation from the thesis may be published without proper acknowledgement.

I certify that all material in this thesis which is not my own work has been identified and that no material has previously been submitted and approved for the award of a degree by this or any other University.

I acknowledge financial support from the Engineering and Physical Sciences Research Council (EPSRC) of the United Kingdom, via the EPSRC Centre for Doctoral Training in Metamaterials (Grant No. EP/L015331/1).

Signed:

_____

Date:

_____

Abstract

Strong coupling of molecules placed in an optical microcavity may lead to the formation of hybrid states called polaritons; states that inherit characteristics of both the optical cavity modes and the molecular resonance. This is possible for both excitonic and vibrational molecular resonances. Previous work has shown that strong coupling may be used to hybridize different excitonic resonances, this can be achieved when more than one molecular species is included in the cavity. In this thesis I show that under suitable conditions different molecular vibrational resonances of the same molecular unit may also be coupled together, the resulting polariton having characteristics of all vibrational resonances. I will also demonstrate strong coupling between surface plasmon resonances and molecular vibrational resonances of polymethylmethacrylate (PMMA) molecules in the mid-infrared range through the use of grating coupling, complimenting earlier work using microcavities and localised plasmon resonances. Many experiments involving strong coupling make use of metal-clad microcavities, ones with metallic mirrors. Metal-clad microcavities are well known to support coupled plasmon modes in addition to the standard microcavity mode. However, the coupled plasmon modes associated with an optical microcavity lie beyond the light-line and are thus not probed in typical experiments on strong coupling. I will investigate, through experiment and numerical modelling, the interaction between molecules within a cavity and the coupled plasmon mode and I will show that such modes do undergo strong coupling, making use of grating coupling to provide an experimental demonstration. Overall, light-matter hybridization offers many new opportunities for the molecular and materials sciences. It works in the absence of light, it is simple to implement, and its full potential is waiting to be explored.

Contents

List of Figures

List of Tables

List of publications

Research publications

Journal papers

Kishan Menghrajani, William Barnes, *Strong coupling beyond the light-line*, *under-review* (2019).

Kishan Menghrajani, Henry Fernandez, Geoffery Nash, William Barnes, *Hybridization of multiple vibrational modes via strong coupling using confined light fields*, **Adv. Opt. Mater.** *1900403* (2019).

Kishan Menghrajani, Geoffery Nash, William Barnes, *Strong coupling of surface plasmons to molecular vibrational resonances on gold gratings and the presence of surface plasmon stop bands*, **ACS Photonics** *9b00662* (2019).

Published conference papers

Kishan Menghrajani, Geoffery Nash, William Barnes,*S*trong coupling of molecular vibrational resonances in a metal-clad microcavity, OSA Technical Digest (online) (Optical Society of America, 2018), paper NoW3D.7 , (2018).

Kishan Menghrajani, Geoffery Nash, William Barnes,*S*trong Coupling of Vibrational Modes: an Investigation using Infrared and Raman Spectroscopy, OSA Technical Digest (online) (Optical Society of America, 2016), paper W3A.27, (2016).

Book Reviews

Kishan Menghrajani, *F*ibre-optic Fabry- Perot sensors: an introduction, Contemporary Physics, 59:4, 402-403 , 2018

Kishan Menghrajani, *E*xcitations in organic solids, by Vladimir M. Agranovich, Contemporary Physics, 58:2, 202, 2017

Conference participation

Oral presentations

Vibrational strong coupling with surface plasmons and the presence of surface plasmon stop bands , London Plasmonics Forum, June 14, 2019, King's College, London, UK

Strong coupling of molecular vibrational resonances in a metal-clad microcavity below cut-off, Molecular Plasmonics workshop, May 23 - 25, 2019, Jena, Germany

Strong coupling between plasmonic and vibratonal resonances in the mid infrared range, OSA advanced photonics, July 4-6, 2018, ETH Zurich, Switzerland

Strong coupling of molecular vibrational resonances in a metal-clad microcavity, SCOM18, April 16-18, 2018, Einhoeven, Netherlands

Poster presentations

Strong coupling between vibrational modes and optical micro-cavity modes: the challenges of combining infrared and Raman spectroscopy, SCOM16, San Sebastian, Spain, 2016

Chapter 1

Introduction, Outline and Motivation

The physics of the light-matter interaction is frequently defined in either weak or strong coupling. In strong coupling, new light-matter hybrid states are created as energy is exchanged between light and mater on a time scale faster than any decay process exchange energy faster than any decay process. The new hybrid states formed in this way are known as polaritons, and the splitting in energy between the polariton levels is referred as Rabi splitting. This is possible for both excitonic and vibrational molecular resonances. Previous work has shown that strong coupling may be used to hybridize different excitonic resonances. Here I show that under suitable conditions different molecular vibrational resonances of the same molecular unit or of different molecular units may also be coupled together, the resulting polariton having characteristics of all of the vibrational resonances. The important condition which determines vibrational strong coupling is, $\sqrt{\frac{N}{V}}$, where N is total number of molecules and V is the mode volume of the system. However the molecule couple with light is not just inherent to the chemical properties of the molecule. In this thesis these aspects of strong coupling are explained:

1. Strong coupling involving multiple vibrational modes of the same molecular species.
2. Vibrational strong coupling involving surface plasmons and the presence of surface plasmon stop bands.
3. Vibrational strong coupling involving the coupled plasmon mode in below cut-off cavities.

I have divided my thesis into 8 chapters.

Chapter 2 is focused on an introduction to the basics of light-matter interactions.

Chapter 3 is focused on the different experimental i.e. Fourier Transform Infrared Spectroscopy (FTIR), Electron Beam Lithography (EBL), Thermal evaporation, Atomic Force Microscopy (AFM) and computational techniques i.e COMSOL used in the work represented in this thesis.

In chapter 4, I will discuss my results on strong coupling of multiple vibrational resonances of the same molecular unit with confined light fields. The results indicate opening a path to greater control of molecular systems and molecular processes via vibrational strong coupling.

Chapter 5 is dedicated to show strong coupling of molecular surface plasmons and to the presence of surface plasmon stop bands. In this chapter, I will present experimental and numerical results which show that surface plasmon modes provide convenient open cavities for vibrational strong coupling experiments. Further I will show that surface plasmon stop bands which are formed under appropriate conditions also strong coupling.

Chapter 6 is focused on vibrational strong coupling in a metal clad microcavity below cut-off. Metal-clad microcavities support a coupled surface plasmon

mode, which appears to have been ignored in previous work on strong coupling, probably because it exists beyond the light-line. In this chapter, through the addition of a grating to the microcavity structure, I show that this coupled plasmon mode also interacts with molecular resonances to produce hybrid polariton modes.

Chapter 7 discuses strong coupling involving photochromatic system. Shinning UV light converts spiropyan to merocyanine. So, strong coupling can be switched from no coupling to strong coupling by just shinning UV light. I will also talk about our initial results of strong coupling using Raman spectroscopy.

In Chapter 8, I will conclude with a discussion on manipulate vibrational resonances in a richer and subtler way than previously considered, opening a path to greater control of molecular systems and molecular processes via vibrational strong coupling.

This chapter provides an introduction to the basics of light-matter interactions relevant to the work carried out for this thesis. In this chapter, I will focus on light-matter vibrational strong coupling. I will present brief background of strong coupling and will talk about the important stages in the emergence of this field. In strong coupling, the interaction between light and matter is such that new hybrid states are formed, part light and part matter, these hybrid states are called polaritons- see Figure 1.3 below.

Experimental results on strong coupling of light with vibrational modes will be a particular focus, highlighting the need to explore this area further for both applications as well as for the fundamental science. Intra-molecular vibrational motions can be described as a superposition of simple harmonic vibrations, so called molecular normal modes.

1.1 Light-matter strong coupling

Hybrid system of light and matter coupling modifies the behaviour and physical properties of the matter. The quasi-bosonic nature of the polaritons has guided researcher towards low threshold lasers and photoluminescent devices [1, 2].

1.1.1 Exciton-polariton

One type of strong coupling is when energy is exchanged between excitons and a confined light field, in this case the polaritons are called exciton-polaritons.

To allow this energy exchange, the system has to have a low energy loss rate. The energy loss rate can be calculated from the absorption peak width of the exciton transition. If the peak width is small, the energy loss will also be low. Most of the experiments done in the past involved narrow absorption exciton

peaks, thus excitons make exciton good candidates for hybridisation involving exchanging of energy with a confined field.

As an example recently H. Fernandez *et al.* [3] has showed electrical control over the energy exchange between exciton state and cavity polaritons at the room temperature. They designed a tunable Fabry-Perot microcavity and placed WS_2 and MoS_2 monolayers in it. They showed strong modulation of the Rabi splitting that modifies excitonic and photonic nature of exciton-polariton by tuning the free carrier density in the WS_2.

To understand the light-matter interactions better, let us discuss light field confinement and the conditions under which this could happen.

1.1.2 Light field confinement

Hybrid light-matter is formed when there is an energy exchange between an electromagnetic light field and material resonance. The energy exchange rate between the two has to be faster than rate at which the total energy of the system dissipates. To have a higher energy exchange rate, there are two factors which play the important role. First is quality factor Q of the system and the other is the confined mode volume V.

The first and foremost condition for higher energy exchange is the quality factor. The quality factor of the system is defined by $Q = \frac{\omega_c}{\Delta\omega_c}$ where $\Delta\omega_c$ is the full width half maximum of the resonant frequency ω_c. It can be calculated from the transmission/reflection of an infrared source. The higher the Q factor the lower the losses. By depositing good smooth quality mirrors, the Q of the system can be improved.

The second parameter is the mode volume V of the system. It depends on confining the electromagnetic field to a smaller volume, such as in the localised

field i.e. optical microcavity or in structured array i.e plasmonic array. In the confined light fields associated with metallic nanoparticles, the mode volume is less but the energy losses are higher and in some photonic crystals, the energy loss is low but the mode volume is high. Therefore microcavities are considered a reasonable compromise as I can confine field the inside the microcavity tightly, and by depositing smooth metal layers, we can reduce the losses of the system as well.

1.2 Study of molecular vibrations

Infrared radiation may cause some molecular bonds to vibrate. Any molecule above absolute zero vibrates. If there is an electronegativity difference across this bond then by definition, there must be a dipole. So, if the molecule vibrates, the dipole moment will change. A changing dipole moment will result in an oscillating electric field and that's how the molecular vibration couples to the electromagnetic field.

A sketch of the structure of a A=B molecule is shown in figure 1.1 (a).

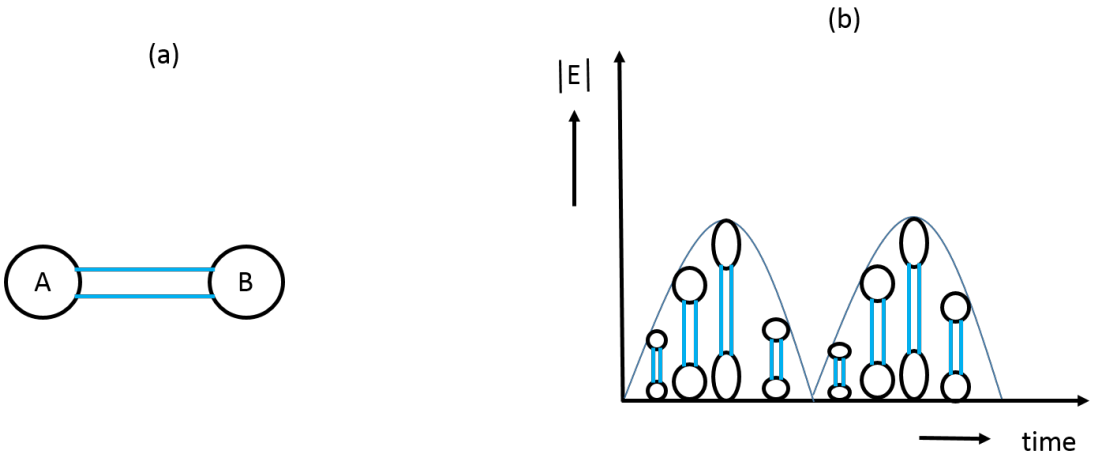

FIGURE 1.1: (a) molecule A=B in equilibrium state (b) when molecule couples with electromagnetic field

Molecule vibration is a stretching or the bending or changing shape of the molecule in question. When the molecule comes into contact with the electromagnetic wave and if the molecule vibrates then it may stretch or bend depending on direction of the electric field intensity as shown in figure 1.1 (b).

When the molecule is not in contact with the electromagnetic field (figure 1.2 (a)) then it remains in the ground state and there is no change in the shape or the size of the molecule, shown in figure 1.2 (b). If the molecule comes in contact with the electromagnetic field (figure 1.2 (c)) then the size or shape of the molecule changes and that means that it has gained energy and has moved to the excited state as shown in figure 1.2 (d).

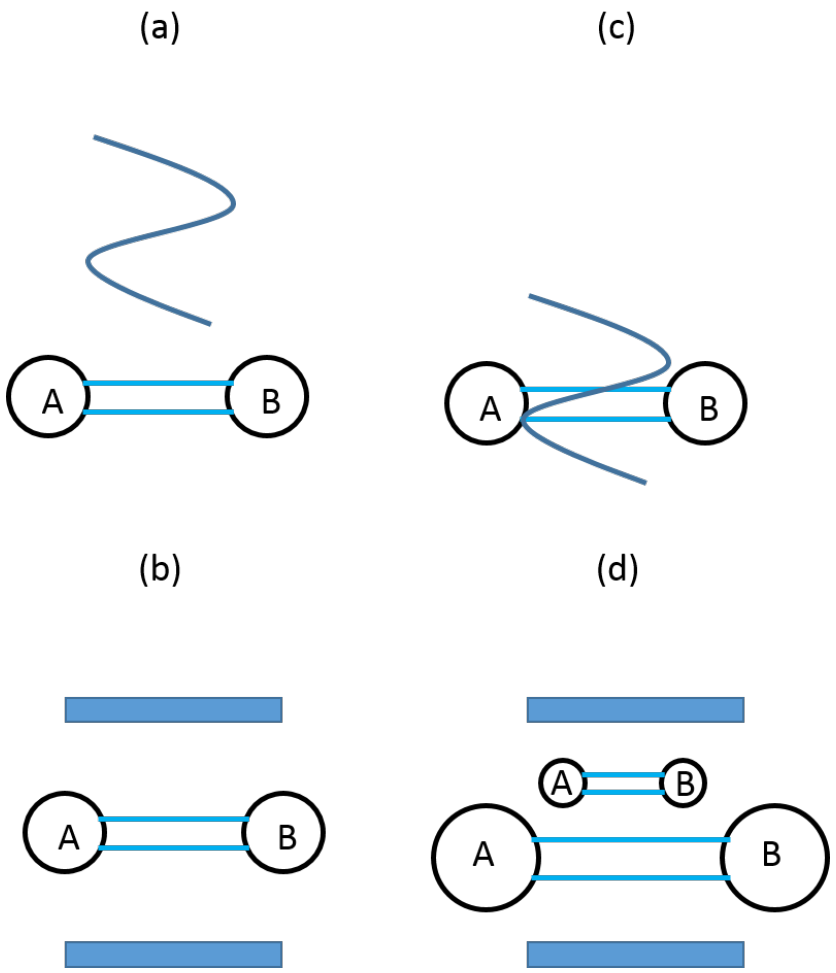

FIGURE 1.2: Molecular vibrations dynamics. (a) when electromagnetic light is not in contact with molecule (b) the molecule inside the microcavity remains in the same position (c) when electromagnetic source interacts with the molecule (d) the change in the molecule position is observed.

When the energy of the molecule changes that means the dipole moment of the molecule has changed. The dipole moment provides information about the size and direction of the charge separation. If atoms in huge number comes in contact with electromagnetic field then it will be excited, it's the same for the molecule vibration but in the infrared regime. Now, infrared doesn't carry the energy to excite electronic states, however it does carry enough energy to excite vibrational states. The molecule can be excited to a very specific energy level thus only specific wavelengths of the infrared radiation will interact. The

specific wavelengths are equal to the difference between the ground state and the specific energy level. Thus, molecular vibration is caused by infrared light whereas the atomic excitation is caused by UV/visible light. Now to understand this better, we will look at the energy level diagram for a hybrid system.

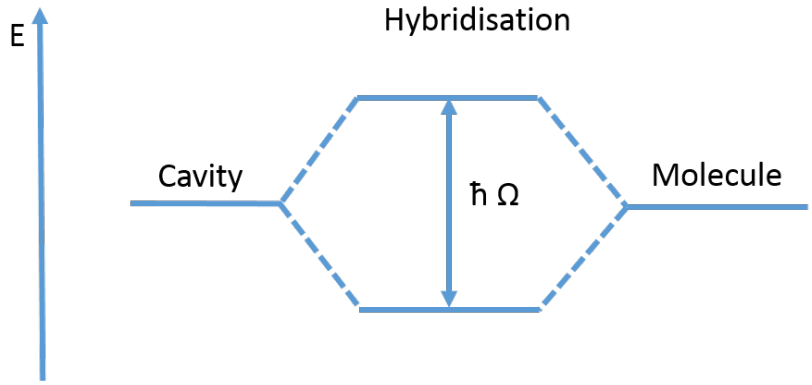

FIGURE 1.3: Energy levels in hybrid system of cavity photons and molecule vibrational mode.

Figure 1.3 shows schematic of hybrid system where cavity photons and molecule vibrations both have the same energy level and they start exchanging energy. If the energy exchange is faster than the decay rate of the overall system then it leads to the formation of hybrid states called polaritons; states that inherit characteristics of both the optical cavity modes and the molecular resonance [4]. The electromagnetic field concentrated in the single mode of a resonator provides in-phase oscillations of all molecular or atomic transitions in this mode. This leads to the formation of a collective dipole. The eigenvalues of the Hamiltonian show an increase in the value of splitting according to the equation

$$h\Omega_R = h\Omega\sqrt{N} \tag{1.1}$$

where N is the number of the coupled oscillators and h Ω_R is the contribution of each of them. Consequently,

$$h\Omega_{\mathrm{R}} \propto \sqrt{\frac{N}{V_{\mathrm{m}}}} = \sqrt{C} \tag{1.2}$$

where C is the concentration of matter in the mode volume. Thus, an increase in concentration can enhance the coupling strength significantly and make it much easier to observe Rabi splitting experimentally. Thus, although the coupling strength of a single emitter in a cavity is rather small, the strong coupling regime can be reached in the cases of both a single emitter and many emitters in various cavities.

1.3 Strong coupling in an optical microcavity structure

Strong coupling is attracting increasing attention, in part because of exciting prospects for modifying chemistry [5–10]. There are two key features associated with this kind of strong coupling that underlie the surge of recent interest. First, strong coupling may change molecular energy levels leading, for example, to modified chemical landscapes [11, 12], and control over photochemistry [13]. Second, strong coupling results in coherent coupling of the molecules, with prospects, for example, of changing exciton transport [14]. In addition, strong coupling can be used to modify the transfer of energy between two species of molecule in a cavity, both where the species are intermixed [15–17] and where the two species are spatially separated [17, 18]. In the visible regime a potentially more radical step is to use strong coupling to hybridize excitonic resonances associated with two different species [17, 19, 20]. Hybridization of

different vibrational overtones of an excitonic resonance of a single molecular species has also been achieved [21, 22].

Strong coupling of vibrational modes was first explored using a planar cavity filled with the polymer polymethyl-methacrylate (PMMA) where the cavity mode was strongly coupled to the C=O vibrational resonance in the polymeric material [5, 23]. Several further investigations have since been reported [24–31], involving vibrational resonances in liquids [32], transition metal complexes [31] and liquid crystals [33]. Strong coupling of vibrational resonances has also been reported to help catalyse and inhibit chemical reactions [34] and to control the nonlinear optical response in the infrared [35]. Two-dimensional spectroscopy of molecular vibrations in an optical microcavity have also been explored [36, 37]. Detailed version of this type of system is discussed in chapter 4.

1.4 Strong coupling in plasmonic structure

Recent work has highlighted the important role played by the sub-band of vibrational states in strong coupling involving excitonic resonances [38]. In addition to their important role in excitonic strong coupling, vibrational resonances may themselves undergo strong coupling. This may be accomplished by placing the molecules in a confined light field that has a resonance at a suitable infrared frequency. This has already been demonstrated using planar microcavities [5, 23], and using surface plasmon resonances, both propagating [28] and localized [39] to produce confined light fields.

In this thesis I will investigate the strong coupling of vibrational molecular resonances with the infrared surface plasmon modes associated with metal surfaces. I will make use of periodic grating structures to probe (momentum match to) the hybrid polariton modes that arise from such strong coupling. In

addition to allowing momentum matching, the grating nature of the metallic surface also modifies the dispersion of the surface plasmon modes, introducing surface plasmon stop-bands [40–42]. This extra degree of freedom allows me to make a first exploration of the interaction of surface plasmon stop bands and hybrid vibro-polariton states produced via strong coupling.

Most experiments on strong coupling with ensembles of molecules involve planar microcavities, the molecules being placed between two mirrors that are either metallic [43] or based on distributed Bragg reflectors [44]. Whist very effective in producing strong coupling, planar microcavities do not allow easy access to the molecules they contain. The edges of such cavities can be accessed [45], but it would be preferable to gain fuller access to the molecules involved. Surface plasmons provide an excellent alternative confined light field for strong coupling [46], one that is broad-band in nature. Although strong coupling of surface plasmon modes to excitonic molecular resonances is well explored, indeed it goes back many years [47], strong coupling of vibrational resonances with the surface plasmon modes of planar metal films is much less explored [28]. Through a combination of experiment and numerical modelling, I will show how surface plasmon modes may be strongly coupled with vibrational molecular resonances. Detailed version of this type of system is discussed in chapter 5.

1.5 Applications

Light-matter hybridization offers new opportunities for the molecular and materials sciences. It works in the absence of light and it is simple to implement which guides many of the applications, a few of them are listed below.

1.5.1 Enhanced IR absorption

Enhanced IR absorption Strong coupling in micro cavity in the MIR spectral region have wide applications, including exploration of energy transfer between light and matter, and are ideal for tunable MIR sources. Recently George *et al.* [32] have shown that liquid phase strong coupling can be simply achieved provided peak absorption has sufficient strength to overcome dephasing time. They have shown that strong coupling could be used to regulate chemical physical properties and precisely control energy states for each molecule [48].

1.5.2 Resonant Raman scattering

Resonant Raman scattering Raman is inelastic scattering between light and a medium. When a particular laser frequency irradiates the sample surface, the material absorbs energy and then scatters the light to a lower frequency. Molecules with different structures and vibration modes have specific Raman spectra, the frequency change is thus specific to the scattering material. Thus, Raman scattering spectra are called fingerprint spectra, identifying molecular material types according to this principle [49].

In the next chapter I will focus on fundamentals. I will mainly talk about surface plasmon modes, surface plasmon polariton modes, dispersion plots.

Chapter 2

Background theory

In this chapter, I will discuss the backgroun theory used in the thesis. On the theoretical side includes the Lorentz model to account for the optical response of a dielectric that includes a resonant absorption. Let's start with surface plasmon.

2.1 Surface plasmon

Surface plasmons are electromagnetic excitations that propagate along the interface between dielectric and metal. When it comes to metals, the plasma frequency is in the UV range, depending on the metal band structure. To understand the principle of measurements, we will start with Kretschmann's configuration.

The schematic for the Kretschmann's configuration is shown in Fig. 2 (a). The setup consists of a monochromatic beam of Transverse Magnetic (TM) polarized light from a laser with vaccum (with relative permittivity of ε_d) wave vector $\overrightarrow{k_d}$ incident on a face of a dielectric prism (shown in light blue color) of permittivity ε, and $\varepsilon_s > \varepsilon_d$. Due to the change in permittivity from ε_d to ε_s, the wave vector of the light inside the dielectric prism changes from $\vec{k}_d$ to $\vec{k}_s$ as shown in Fig.

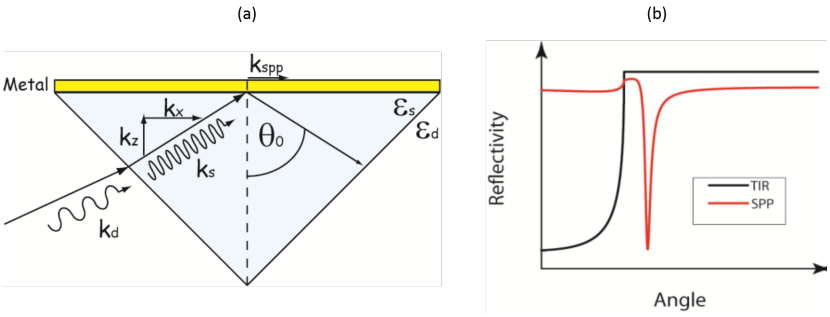

FIGURE 2.1: (a) Shows the schematic of Kretschmann's configuration for the excitation of surface plasmons. (b) Possible reflected intensity profile when the dielectric prism is not coated with a thin layer of metal (Black curve) and coated with a thin layer of metal (Red curve).

$2(a)$. Let the wave vector of the light inside the dielectric prism be decomposed into two Cartesian components k_x along the x -axis and k_x along the z -axis. If the dielectric prism (shown in light blue color) is coated with a very thin metal of permittivity of ε_m shown in yellow in Fig. 2 (a), such that the thickness of the metal layer (in z-direction) is relatively small compared to the wavelength of the incident light, then, tunneling of light across the metal layer occurs leading to a portion of light traveling to the top interface between the metal and vacuum. By starting with an electromagnetic wave having $\left(E_x, H_y, E_z\right)$ components corresponding to the TM polarization, one can apply the continuity boundary condition at the top metal/vacuum interface, according to which the parallel components of the E and H fields are continuous. This will lead to the relationships $\frac{k_{x(\text{ cemal})}}{\varepsilon_{\text{mal}}} = \frac{k_{\text{scemaum}}}{\varepsilon_d}$ and $k_{x(\text{ metreet reach}}\Big) = k_d\sqrt{\frac{\varepsilon_x\varepsilon_d}{\varepsilon_m+\varepsilon_d}}$. The $k_{x(\text{ read-temed}}\Big)$ corresponds to the x -component of the wave vector of fields setup at the top interface between metal and vacuum, and physically, this corresponds to the wave vector of surface plasmon resonance at that interface. The actual meaning of the relationship is that if the x-component of the wave vector, namely k_x of the incident monochromatic is changed (k_x may be changed by changing the angle of . incidence of monochromatic beam of light thereby changing the

Cartesian components k_x and k_x while maintaining the same total wave vector $\hat{k}_x$), for some value of k_x, the light may be coupled to collective oscillations of the electron cloud on the top interface between metal and vacuum. It can be proven that, for such a coupling between incident TM polarized monochromatic beam of light and collective oscillations of electron cloud to occur, the angle at which the light arrives at the interface of dielectric prism and metal layer, should be greater than the critical angle of incidence at the interface of dielectric prism and vacuum (assuming that the metal layer is not present).

An experimental setup corresponding to the Kretschmann's configuration may consist of a laser source producing the incident beam of monochromatic light, that illuminates a dielectric prism coated with a thin layer of metal. A photodetector can be used to measure the intensity of the reflected beam. The angle of incidence can be changed by moving the laser and correspondingly, the angle of reflection changes following the law of reflection. In order to record the intensity of the reflected light, the photodetector should also be correctly positioned at the correct angle of reflection. This means that, in a real time experiment, the laser and photodetector would move such that angle of incidence varies and the angle of reflection at all instances of time should be equal to the angle of incidence. Fig. $2(b)$ shows the possible intensities detected by the photodetector for two cases. The curve in black shows the intensity profile of the reflected beam that would be recorded by the photodetector, when the dielectric prism is not coated with a metal. The curve indicates that upto the critical angle, almost all of the light is transmitted and beyond the critical angle, almost all the light is reflected to the photodetector. The red curve of Fig. $2(b)$ shows the possible intensity profile that would be recorded by the photodetector, when the dielectric prism is coated with a thin layer of metal. For almost all the angles of incidence, the entire light is reflected back in this case,

except for a small range of angles of incidence, wherein a drop in reflectivity is observed. This drop in reflectivity at a small range of angles of incidence, when the dielectric prism is coated with a metal, is attributed to the coupling of light to collective oscillations of the electron cloud or Plasmons at the metalvacuum interface.

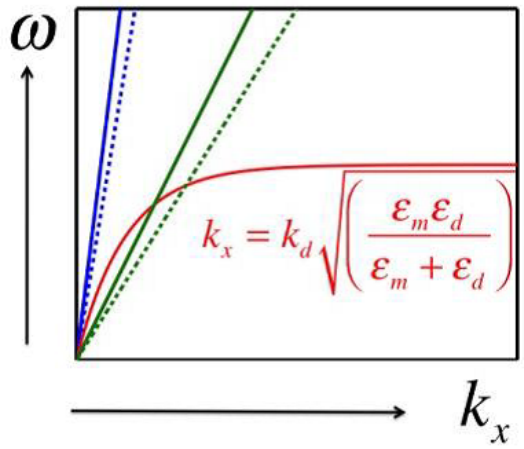

FIGURE 2.2: Dispersion characterisations of SPP (red curve), dielectric (green curves), and vacuum (blue curves). The dotted curves do not account for the angle of incidence while calculating k_x whereas the solid curves take into account the angle of incidence while calculating k_x.

Fig. 2.3 shows the calculated dispersion characteristics (ω vs k_x) for different cases. The dotted blue curve in Fig. 2.3 corresponds to the dispersion curve of vacuum (or free space) and is calculated simply using $\omega = ck_x$, where c is the velocity of light in vacuum. The solid blue curve is the calculated dispersion curve of vacuum considering some angle of incidence in vacuum and this angle changes the $\times$ component of the wave vector namely k_x. The solid blue curve is calculated using $\omega = ck_x \sin\theta$, where θ is some angle of incidence. Note that the maximum possible value of ω occurs for the case when the incident wave vector is directed along x axis or equivalently, $\sin\theta = 1$, implying grazing incidence at the interface. The solid red curve in Fig. 2.3 is the dispersion relationship calculated from the expression obtained above

$k_{x(\text{ (mat-mace)}} = k_d \sqrt{\frac{\varepsilon_m \varepsilon_d}{\varepsilon_m + \varepsilon_d}}$. It can be seen that as k_x continues to increase beyond a value, the angular frequency ou stabilizes to a fixed value and this value of the angular frequency corresponds to the resonance frequency (ω_∇) of the metal/vacuum interface. This curve is a little interesting in the sense that for a fixed resonance frequency say ω_∞, the value of the wave vector in the x -direction can be very high and considering the relationship $\lambda_x = \frac{2\pi}{k_x}$, the wavelength of the collective electron cloud oscillations can be extremely small. The resonance frequency for most naturally occurring metals is in the visible and UV frequencies. This implies that at visible frequencies, under resonance, extremely small wavelengths much smaller than the diffraction limit of the incident wave can be obtained. Hence these resonances pave way for interesting opportunities in sub-wavelength diffraction unlimited imaging or focusing systems. Looking at the red curve and blue curves in Fig. 2.2. we can see that the blue and red curves do not intersect at any point except at origin. The intersection of curves is very important in order to understand the term Coupling. When dispersion curves of two material systems intersect each other at specific point, energy transfer can occur from one material system to another and this intersection point is called as Wave Vector Matching (or equivalently Momentum Matching). It should be noted that the blue curves and red curve of Fig. 2.2, do not intersect at any point other than the origin. This signifies that no energy transfer can occur or no coupling can occur from a wave traveling in vacuum to the plasmons on the metallvacuum interface. The dotted and solid green curves in Fig. 2.2 indicate dispersion relationship of a dielectric medium with permittivity higher than vacuum, without and with consideration of angles of incidence respectively. In this case, permittivity was assumed to be that of glass (corresponding to the dielectric prism in our earlier discussion). It is immediately apparent from Fig. 2.2 that the green dotted curve intersects the

red solid curve, which means that at the point of intersection, wave vectors are matched and energy transfer (or coupling) can occur. In the prior discussion about Kretschmann's geometry, the main requirement for the coupling from incident light to plasmons are therefore firstly, the permittivity of the prism should be higher than that of vacuum and secondly, the thickness of the metal layer on top of the prism should be smaller than the penetration depth of the evanescent field at the dielectric/vacuum interface.

2.1.1 Excitation of SPP

There have been different way in which we can excite the surface plasmon polariton. Here we will mainly focus on two types, 1) Prism Coupling and 2 Grating Coupling.

2.1.1.1 Prism coupling

The prism coupling which is also known as attenuated internal reflection which involves the coupling of the SPP to the electro magnetic evanescent field which is formed because of the total internal reflection of the light beam at the surface.

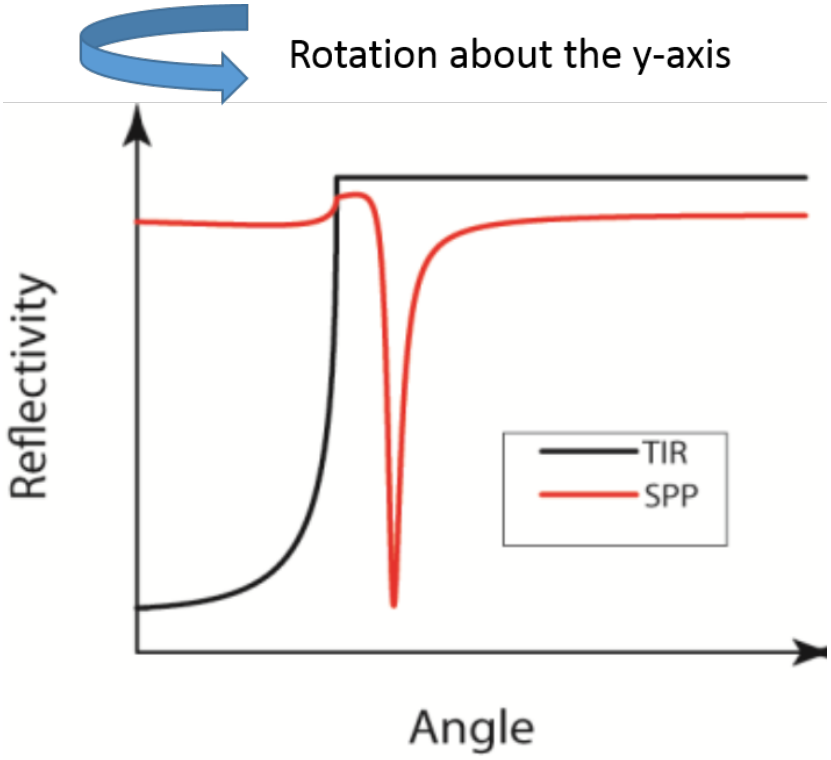

FIGURE 2.3: Reflection characteristics on glass/dielectric intertace (Black curve) and on glassfimetaldielectric intertace (Red curve)

Consider the reflectivity curve shown in Figure 2.3 where the red curve corresponds to the excitation of plasmons. This curve is valid for a particular point on the dielectric/metal interface, whereas in the experimental work performed,

$\sim$ 2D layer of gold was deposited on the glass substrate. The reflectivity for such a layer could then be obtained by rotating the red curve in Fig.2.3 about the y -axis by 360 degrees. This would than mean that in the Kretschmann's configuration, normally one would observe a dark ring in a bright background. A dark ring in a bright background is extremely difficult to observe and study, since the signal to noise (here signal means dark region corresponding to plasmons and noise means bright region not associated with plasmons) is very poor.

2.1.1.2 Grating coupling

When there is the mismatch in the wavevector between β and in place momentum, then it can be overcome by using diffraction effects on grating pattern on the metallic surface.

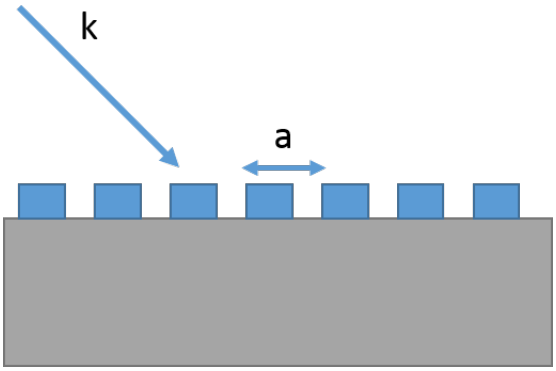

FIGURE 2.4: (a) Grating pattern with incident wavevector k and pitch as a.

The condition $\beta = k \sin\theta \pm nG$ has to be fulfilled where, $G = 2\pi/a$ is the reciprocal vector of the grating and n is the positive integer. The SPP dispersion of the SPP is replicated at interval of G, the grating period. Detailed study of SPP and dispersion plots will be discussed in chapter 4. Now, we will move to the Lorentz model of the permittivity in next section.

2.2 Optical response of materials and model parameters

2.2.1 Lorentz model of the permittivity

The Lorentz model is a classical theory for the interaction between bound charges and an electric field. In the Lorentz model, matter is considered to be composed of point-like electric dipoles [50]. The dipoles respond harmonically to an applied oscillating EM field, for example the confined filed associated with an optical microcavity. Supposing that each electron of charge -e, in a medium is displaced a distance r from its equilibrium position, the resulting macroscopic polarization density P of the medium [51] is given by,

$$P = -\frac{N}{V}er \tag{2.1}$$

where $\frac{N}{V}$ is the number of dipoles per unit volume . If the local field of the dipoles is neglected, the equation of motion for a bound electron is,

$$\left(\frac{\mathrm{d}^2 r}{\mathrm{d}t^2} + \gamma\frac{\mathrm{d}r}{\mathrm{d}t} + \omega_0^2 r\right) = -\mathrm{e}E(r,t) \tag{2.2}$$

where ω_0 is the frequency of the harmonic oscillator and γ is a phenomenological measure of the damping force.

If I now suppose that the applied electromagnetic field varies harmonically with time according to the usual factor $e^{i\omega t}$ then within the normal dipole approximation, the EM field is constant in r since the electron movement is small compared to the wavelength of the EM field at the scale of visible/IR light, so that,

$$m\left(-\omega^2 - i\omega\gamma + \omega_0^2\right) r = -\mathrm{e}E \tag{2.3}$$

here m is the mass of electron. Consequently, the polarization in equation 3.1, is given by,

$$P = \frac{Ne^2}{Vm}\frac{1}{\omega_0^2 - \omega^2 - i\omega\gamma}E \tag{2.4}$$

The linear polarization is defined as,

$$P = \varepsilon_0 \chi E, \tag{2.5}$$

where ϵ_0 is the vacuum permittivity,and χ is the macroscopic electric susceptibility. I thus obtain,

$$\chi(\omega) = \frac{A}{\omega_0^2 - \omega^2 - i\omega\gamma}, \tag{2.6}$$

where I have denoted $A = \frac{Ne^2}{V\varepsilon_0 m}$. Since I will often need the permittivity, I note that the permittivity of the medium is associated with the susceptibility through,

$$\varepsilon(\omega) = 1 + \chi(\omega) \tag{2.7}$$

Considering my experimental cases, the momentum-energy $k - \omega$ dispersion [52, 53], e.g. of a transverse EM wave in a Fabry-Perot cavity discussed in chapter 4, or propagating on the metal surface discussed in chapter 5, can be written as,

$$k = \frac{\omega}{c}\sqrt{\varepsilon(\omega)} \tag{2.8}$$

In terms of the reduced momentum, $\kappa = kc$, then,

$$\kappa^2 = \omega^2\varepsilon(\omega) = \omega^2\left(1 + \frac{A}{\omega_0^2 - \omega^2 - i\omega\gamma}\right) \tag{2.9}$$

For the case that ω is close to ω_0, an approximate version of above equation can be obtained,

$$(\kappa - \omega)\left(\omega_0 - \omega - i\frac{\gamma}{2}\right) = \frac{A}{4} \tag{2.10}$$

This equation is the well-known dispersion relation for coupling between material dipoles and and EM field [52]. The two solutions of equation 3.10 correspond to two new normal modes of the system, they are ω_+ and ω_-, given by,

$$\omega_\pm = \frac{\kappa}{2} + \frac{\omega_0}{2} - i\frac{\gamma}{4} \pm \frac{1}{2}\sqrt{A + \left(\kappa - \omega_0 + i\frac{\gamma}{2}\right)^2} \tag{2.11}$$

At resonance, κ=ω_0, so that,

$$\omega_\pm = \omega_0 - i\frac{\gamma}{4} \pm \frac{1}{2}\sqrt{A - \frac{\gamma^2}{4}} \tag{2.12}$$

This result neglects dissipation of the optical mode. To include such dissipation, κ can be replaced with $\kappa = \frac{-i\gamma_{OM}}{2}$ so as to include the losses associated with the optical mode [52].

$$\omega_\pm = \omega_0 - i\frac{\gamma}{4} - i\frac{\gamma_{OM}}{4} \pm \frac{1}{2}\sqrt{A - \left(\frac{\gamma}{2} - \frac{\gamma_{OM}}{2}\right)^2} \tag{2.13}$$

The energy gap between ω_+ and ω_- known as the Rabi frequency or Rabi splitting, is given by,

$$\Omega_R = \sqrt{A - \left(\frac{\gamma}{2} - \frac{\gamma_{OM}}{2}\right)^2} \tag{2.14}$$

If the damping and losses of both the material resonance and the optical mode can be neglected, i.e. in the γ = 0 andγ_{OM} = 0 limit, then the Rabi frequency

becomes,

$$\Omega_R = \sqrt{A} = \sqrt{\frac{N}{V}} \frac{e}{\sqrt{\varepsilon_0 m}} \tag{2.15}$$

This last result is important, it shows how the Rabi splitting depends on the mode volume and the number density of dipoles (molecules) within the mode volume. More specifically it shows that to increase the Rabi splitting, i.e. to increase the strength of the interaction, the number density of resonators (molecules) within the mode volume needs to be as high as possible [47, 54].

At this point it is useful to make the Lorentz model more specific to the molecular resonance material of choice in this thesis, the C=O bond in PMMA.

2.2.1.1 Permittivity associated with vibrational mode

To model the optical response of the C=O vibrational mode in PMMA, I make use of the Lorentz model, and include in a phenomenological way the oscillator strength f so as to account for the strength of the C=O transition.

For the PMMA I used a model based on C=O Lorentz oscillator, with parameters shown in Table 3.1, and with ε_∞ taken to be 1.99.

$$\varepsilon(\omega) = \varepsilon_\infty + \sum_j \frac{\omega_{j,0}^2 f_j}{\omega_{j,0}^2 - \omega^2 - i\gamma_j \omega}, \tag{2.16}$$

For PMMA, the following parameters were found to provide a good match to the experimentally determined transmittance of PMMA, see figure 3.3,

vibrational mode	f_j	$\omega_j(\ rad\ s^{-1})$	$\gamma_j(\ rad\ s^{-1})$
C=O (j=1)	0.0165	3.26248×10^{14}	5×10^{12}

TABLE 2.1: Lorentz model parameters for the C=O PMMA vibrational mode

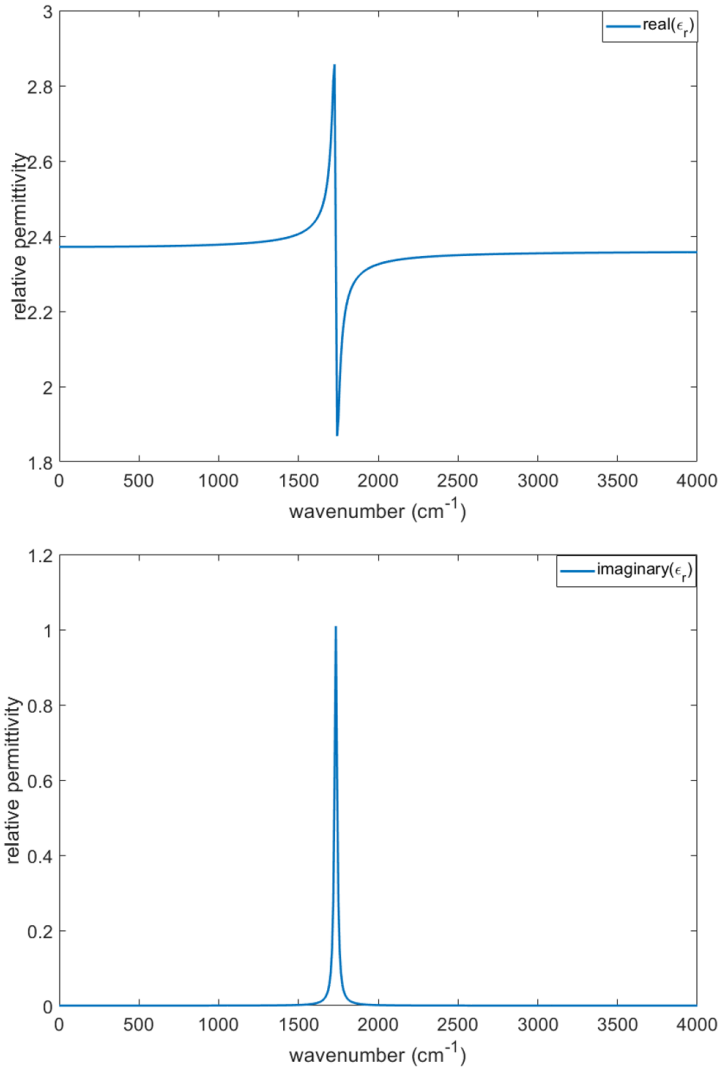

FIGURE 2.5: PMMA permittivity in infrared regime (top) real part (bottom) Imaginary

With these parameters, the permittivity of PMMA with respect to wavenumber is shown in Figure 2.5.

2.2.1.2 Permittivity of metal

In this thesis much use is made of metal mirrors. For metals there is no resonance frequency since the electrons are free to move i.e. $\omega_0 = 0$. The permittivity

given by the Lorentz model, equation 3.9, thus becomes,

$$\varepsilon(\omega) = \varepsilon_b - \frac{\omega_p^2}{\omega^2 + i\gamma\omega}, \tag{2.17}$$

which is also known as Drude-Lorentz model of permittivity.

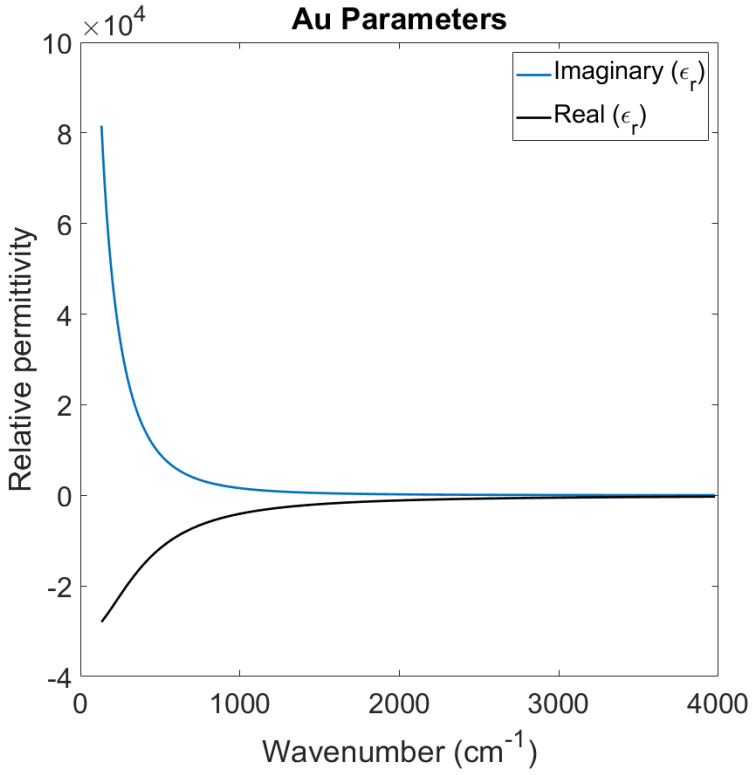

FIGURE 2.6: Au permittivity in infrared frequency regime

For the material parameters, I made use of a Drude-Lorentz model for the optical response of the gold, with parameters taken from Olmon *et al.* [55], specifically, $\omega_p = 1.29 \times 10^{16}\ rad\ s^{-1}$, and $\gamma = 7.30 \times 10^{13}\ rad\ s^{-1}$, with $\varepsilon_b = 1.0$.

With these parameters, the permittivity of gold with respect to wavenumber is plotted in Figure 2.6, and shows the real (black) and the imaginary (blue) components of the permittivity.

2.2.1.3 Optical parameters for substrates

The parameters for silicon in the infrared are based on data compiled by Edwards [56] and are taken to be, $\varepsilon = 11.76 + 0.001i$, whilst for air I took $\varepsilon = 1.0$. Finally, for CaF_2, data were taken from Malitson [57], at 5.0 μm the refractive index is $n = 1.40$.

2.3 Summary

In this chapter, I focused on the fundamentals. I started with surface plasmon then surface plasmon polariton. I also discussed derivation for Lorentz' model. Finally, I ended chapter with providing Lorentz parameters for gold and PMMA material, about which I will mention in details in the next chapter.

Chapter 3

Experimental and computational techniques

I will discuss a number of different experimental techniques used in this thesis, including Fourier transform infrared spectroscopy, electron beam lithography, atomic force microscopy, and thermal evaporator techniques. Finally, I will highlight the computational techniques and numerical modelling used, with a special focus on the use of the commercial package; COMSOL.

Here I discuss the major experimental techniques used in this thesis.

3.1 FTIR (Fourier Transform Infra-Red spectroscopy)

Figure 3.1 shows a schematic of the FTIR set up used for much of the work in this thesis. Infrared radiation from the source is first incident on a beam splitter that divides it into two beams. One beam is is reflected from a moving mirror (that oscillates back and forth) the other is reflected from a stationary mirror. Both reflected beams are directed back towards the beam splitter and recombined. The resulting beam then passes through the sample to the detector. To convert the detected signal into a spectrum, a fast Fourier transform algorithm is carried

out [58]. FTIRs are capable of high resolution because the resolution limit is an inverse of the achievable optical path difference (OPD). Therefore, a 4 cm OPD instrument can reach a 0.25 cm^{-1} resolution.

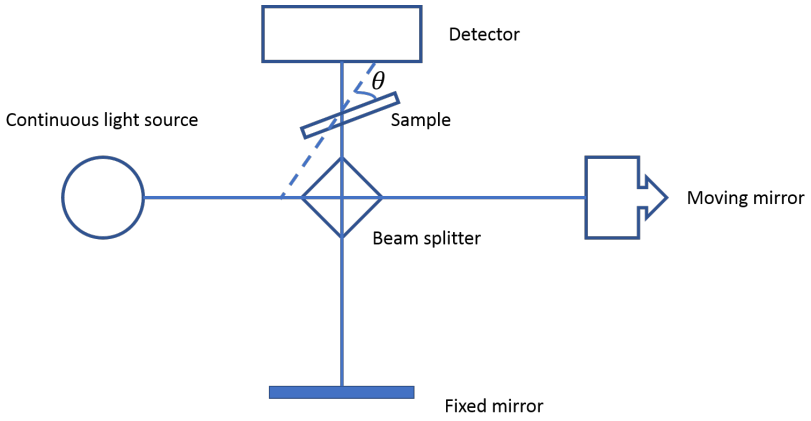

FIGURE 3.1: Schematic of FTIR set-up

A photograph of the FTIR set-up is shown in figure 3.2. A sample holder is placed on a rotatory stage so as to allow the angle of incidence to be controlled. All measurements were carried out under vacuum conditions.

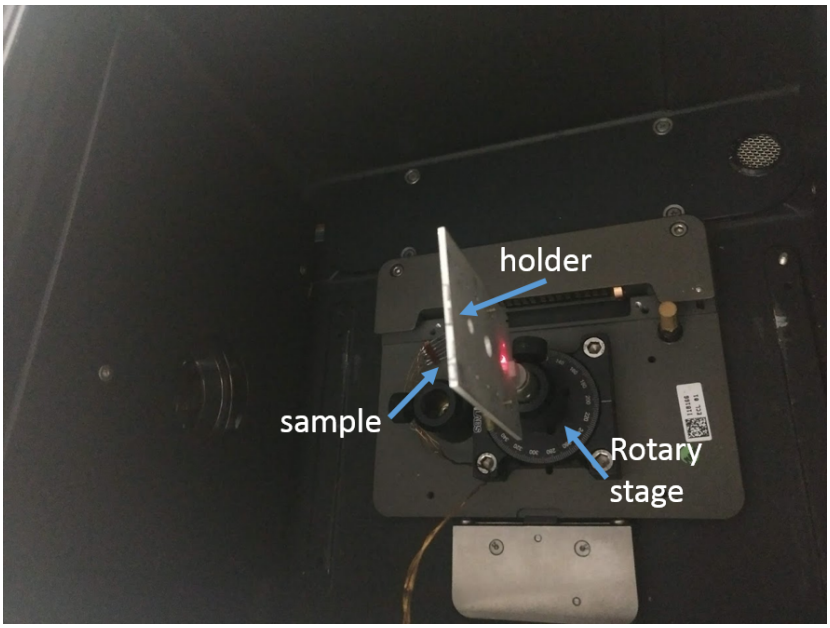

FIGURE 3.2: Photograph of FTIR set-up

In order to produce normalised data, first, a (reference) spectrum is acquired with the sample holder in placed, but without a sample being present. Second, the sample mounted into the sample holder and a second (signal) spectrum acquired. To produce a normalised spectrum the signal spectrum is divided by the reference spectrum. The rotatory stage allowed steps of 2° to be achieved, and the spot size of the beam was around 2 mm. The red light in the figure is only used to determine the position of the source and not used for the experiment purpose. Figure 3.3 shows the FTIR transmission spectrum of a PMMA film in solid black line and calculated transmission spectra is shown in blue dashed line. The PMMA is spin coated on Si substrate. The film thickness is 2 um. Here, all the measurements were taken in terms of wavenumber. The sharp dip at 1730 cm^{-1} shows the strong presence of the C=O bond.

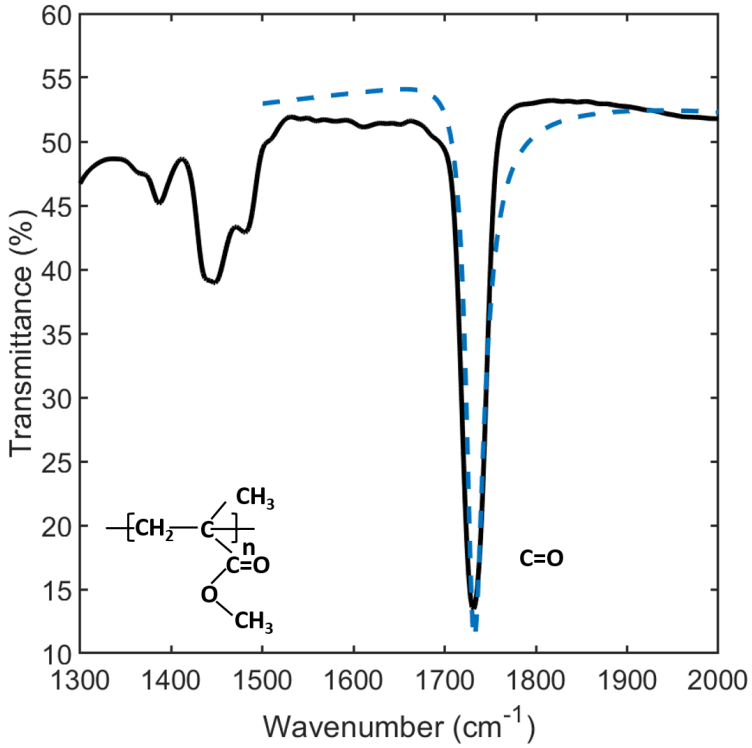

FIGURE 3.3: FTIR transmission spectra of PMMA molecule in solid black line and calculated transmission spectra in blue dashed line. The strong presence of C=O bond can be seen at 1732 cm^{-1}

For the measurements at non-zero angles of incidence, angles up to 60°-70° could be used, but at higher angles most of the most signal was blocked. Where data were acquired so as to provide a dispersion diagram, data were acquired for several angles. Examples of dispersion plots are shown in chapter 4, 5 and 6. To acquire the data presented in this thesis a careful choice of substrates and of the metals that form the cavity mirrors was required. The vibrational modes those I am interested are in in the mid-infrared range and as silicon substrate has higher transmission in the mid-infrared range, it makes silicon a good candidate for the study, also gold reflects infrared frequency strongly - with choices the coupling between molecular resonances and a cavity field could be demonstrated. The signature of the strong coupling between the C=O band and the first cavity mode can be observed in data such as those presented in Chapter 4.

3.2 Electron beam lithography

Electron beam lithography (EBL) is a powerful technique to create nano-structures which are too small to fabricate with conventional photo-lithography. Feature sizes down to a few nanometers can be achieved. A highly focused electron beam is scanned over a sample to write out a pattern, designed with suitable CAD tools.

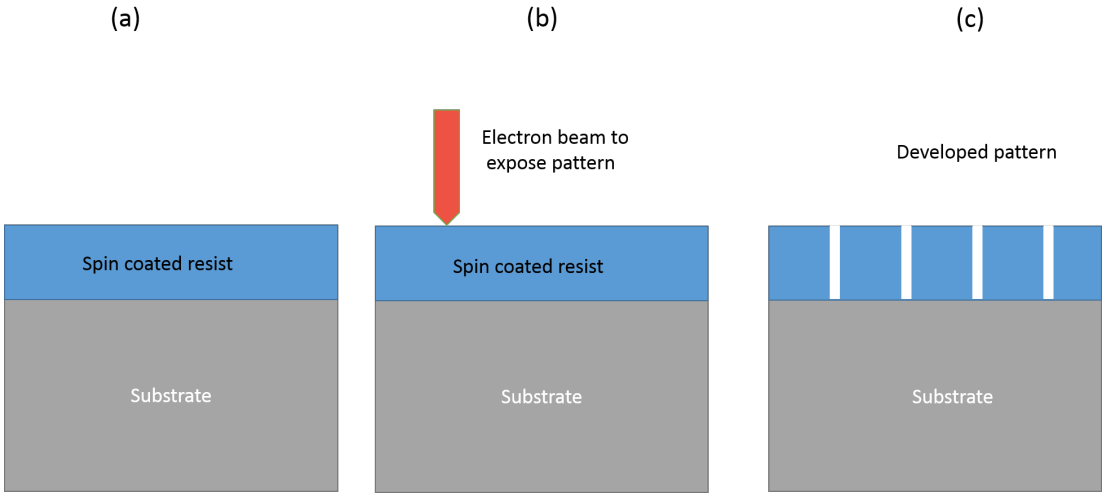

FIGURE 3.4: Process of EBL (a) the resist is spin coated on substrate (b) the desired pattern is written using electron beam current (c) with the help of the developers, the sample is developed.

The pattern is written on an electron sensitive resist deposited on the sample before exposure by spin coating. The electron beam induces a change in solubility of the resist film and in the molecular structure. Once the resist is exposed to the electron beam, it is developed in a suitable solvent to selectively dissolve either the exposed or unexposed areas of the resist depending on the technique which is selected while writing the pattern.

Figure 3.4 shows schematics of the electron beam lithography process. First the resist is spun on the substrate. The thickness of the resist is chosen to be appropriate for the desired thickness of the metal film. The ratio of PMMA to the metal thickness is kept at around 2:1 so as to facilitate the lift-off process.

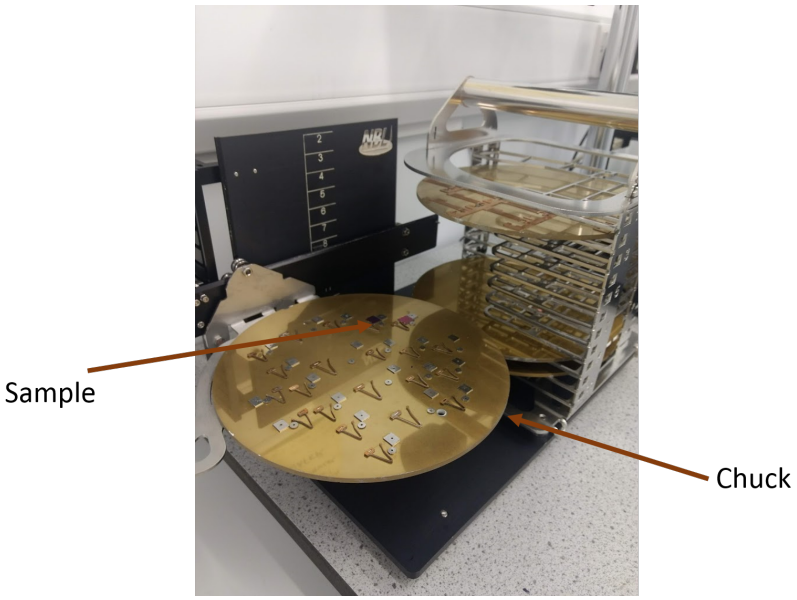

FIGURE 3.5: Photograph of electron beam lithgraphy set-up

For spinning the resist the substrate is mounted on a chuck. Different chuck heights can been seen in figure 3.5 Depending on the size of the sample, the chuck is chosen. Once, the sample perfectly fits in the chuck then the chuck is loaded on the stage and the system is the pumped down. A photograph of the electron beam lithography system is shown in figure 3.5. Once the system reaches the desired pressure ($2x10^7$ mbar), the pattern is written on the substrate. The beam current of the machine is chosen according to the smallest feature size required in the pattern. The pattern is prepared in CAD file. Then, for development, a mixture of Isopropyl Alcohol (IPA), Methyl isobutyl ketone (MIBK) and Methyl Ethyl Ketone (MEK) in 15:5:1 is used.

3.3 Thermal evaporator

The thermal evaporation of materials under vacuum is a powerful technique which provides to make the thin films that were required. In the evaporation process a given material is heated under vacuum until the materials boils. The

resulting vapour then condenses on the substrate to form a thin film. The film may be from a few nanometers to thousands of nm thick. Thermal evaporation is usually carried out at under high vacuum, typically 2x10^{-6} mbar.

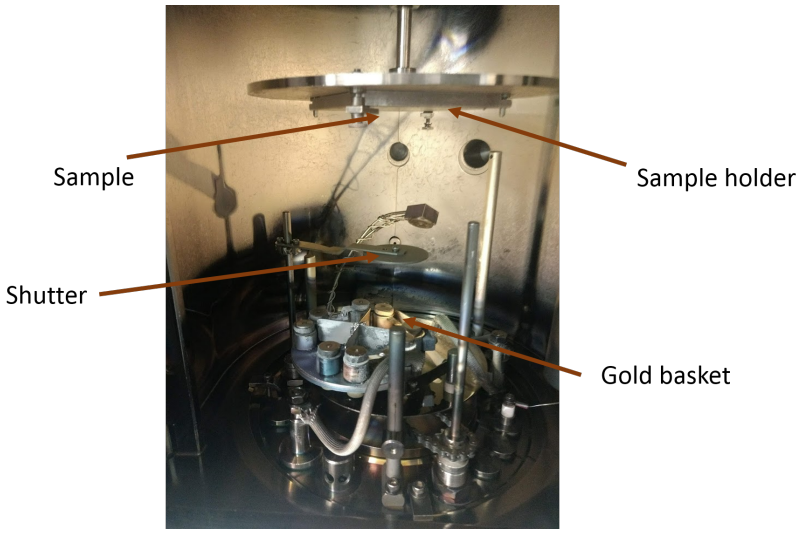

FIGURE 3.6: Photograph of thermal evaporator set-up

In the thermal evaporation process, the sample is mounted upside down on the stage as shown in figure 3.6. The shutter is opened while depositing the gold. The deposition rate is selected according to the behaviour of each material, in particular with regard to film roughness. Too low a deposition rate sometimes creates an island effect. For all the samples used in this thesis, I used a deposition rate at around 0.9 Angstrom/second. Pumping down the vacuum chamber takes around 3-4 hours.

3.4 Atomic Force Microscopy

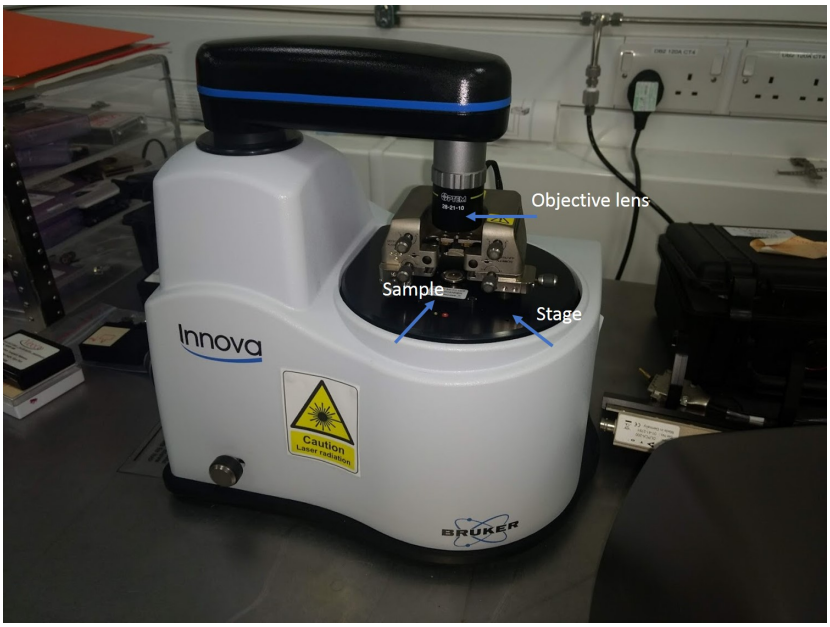

FIGURE 3.7: Photograph of AFM set-up

To determine the topology of some of the samples used, especially those based on electron-beam lithography , atomic-force microscopy (AFM) was used. The photograph of AFM set up is shown in figure 3.7

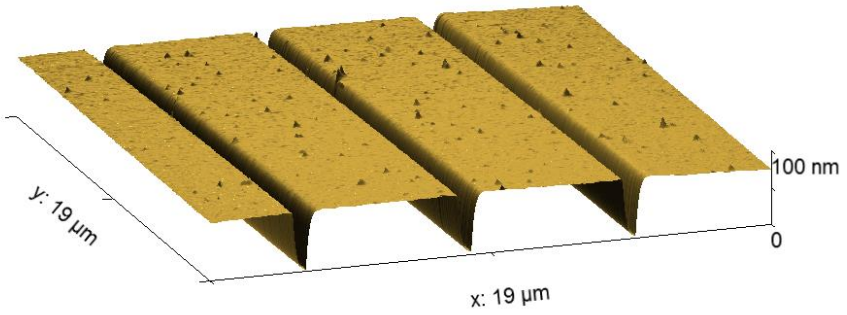

FIGURE 3.8: An example of AFM showing 100 nm 1D grating structure with pitch 4.7 μm and gap of 1 μm.

Atomic force microscopy allows information of the surface topography of two dimensional materials to be determined by measuring the deflection of a cantilever as the cantilever is raster scanned over the sample. The AFM used here was a Bruker Innova AFM system in contact mode, employing a standard Aluminium coated Si cantilever with a spring constant of roughly 35 N/m, and having a tip radius of ~ 7 nm. Further, an AFM was used in this thesis as an additional, independent method to determine gold thickness of the samples shown in chapter 4. An example showing 100 nm gold thickness of the grating sample is shown in figure 3.8

3.5 Computational technique

3.5.1 COMSOL

COMSOL is a powerful numerical package that allows electromagnetic simulations to be carried out using the finite-element method. A full description of COMSOL's working is beyond the scope of this thesis. A key factor is using such an approach is the correct selection of boundary conditions. The most relevant boundary conditions of COMSOL used in the modelling of light-matter systems in this thesis are discussed in this section, followed by some brief comments on meshing.

Throughout this thesis, a numerical technique called the Finite Element Method (FEM) was used to design and test the electromagnetic response of various sample systems, via computational simulations. These simulations helped to build a better understanding of the infrared response of the devices developed in this thesis and to validate the experimental results. The commercial FEM software package "COMSOL Multiphysics" is used [59] . COMSOL solves the time-harmonic electromagnetic wave equation by implementing Maxwell's equations subject to the material properties and the geometry used in the models. It employs several boundary conditions to help describe the geometric entities in the modelled system which exploit properties like symmetry and repetition [60].

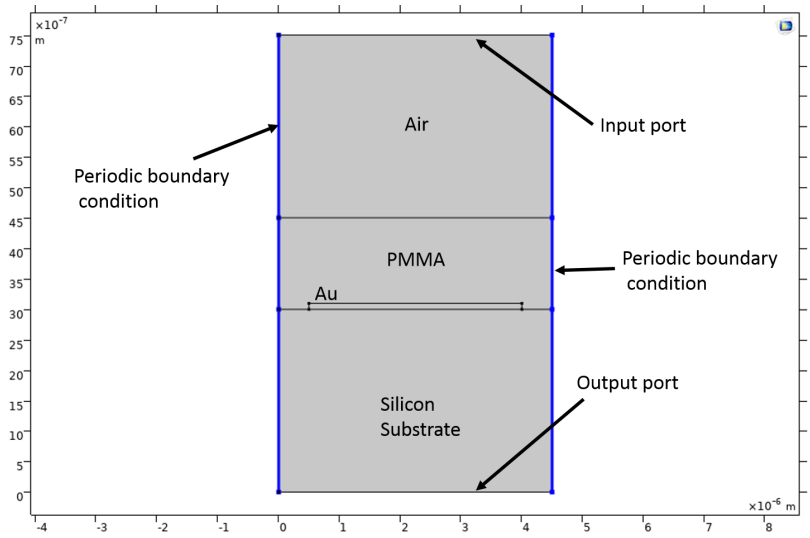

FIGURE 3.9: Graphical representation of unit cell of one dimensional grating structure. To simulate the infinite periodic medium in the x-direction, periodic condition is applied at the edge of the unit cell, shown in as blue lines.

A graphical representation of one of the example that I used for my study (more details are in Chapter 4) is shown in figure 3.9. The figure shows an example COMSOL model of a single unit cell for a one dimensional grating structure designed in this work. The pitch of the structure is 4.7 um and the gap is 1 μm on each side. The gold thickness is 30 nm and the PMMA on the top is 1.5 μm thick. The top layer is air and the bottom layer is a silicon substrate. To simulate the infinite periodic grating structure in the x-direction, a periodic boundary condition is applied at the edge of the unit cell. The blue lines at the edge represent these periodic boundary conditions. It is often necessary to solve several variations of a model to find optical design parameters. Parametric sweeps could be used to evaluate the device's response for a wide variety of geometrical parameters, allowing optimal designs to be easily selected.

Ports: In the FEM model, a port is a boundary where the electromagnetic energy either enters or leaves. For this thesis, the input port is set to launch the TM mode of the computational region and the output port at the other end of

the computational region is a 'listener' port, which collects the electromagnetic energy in the TM mode. The ports support the calculation of S-parameters that can be compared to those experimentally obtained using FTIR. S_{21}/S_{12} used for transmission measurements and S_{11}/S_{22} for reflection measurements.

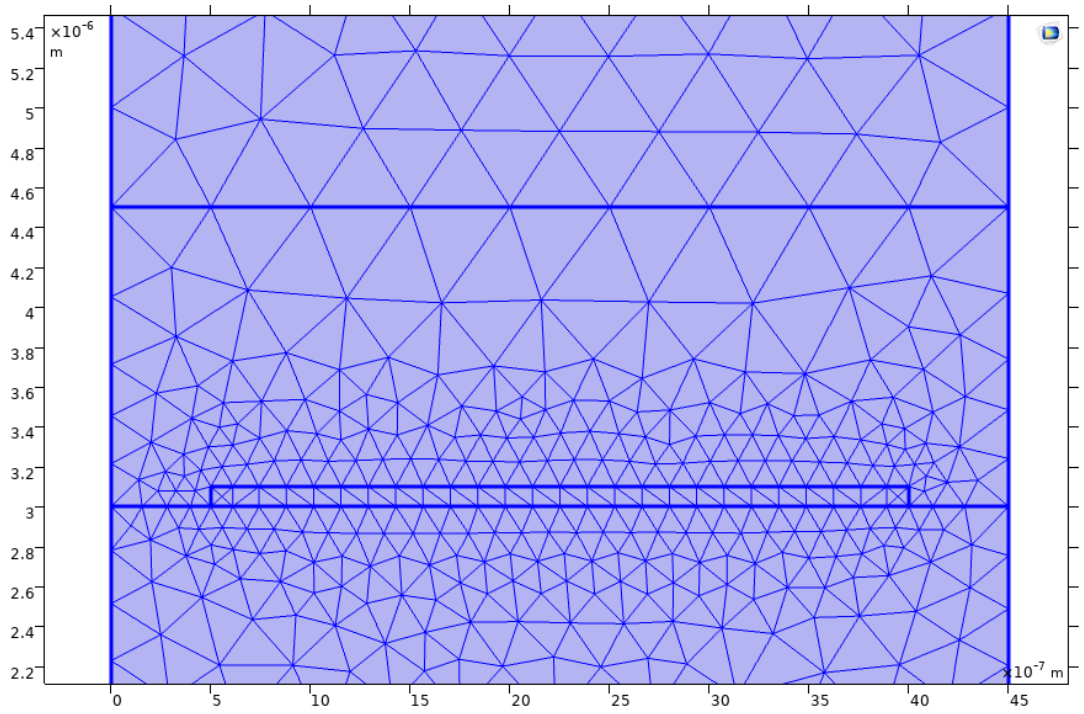

FIGURE 3.10: An example of COMSOL mesh showing one dimension grating structure, meshed with triangular elements.

Meshing: Once the geometry is constructed in COMSOL and all the necessary boundary conditions are applied, then the geometry is discretized into finite mesh elements. Maxwell's equations are solved at the nodes of the mesh elements with the appropriate boundary conditions taken into account. Figure 3.10 shows a portion of the meshed geometry of a one dimensional grating model used to compute the triangular elements employed in COMSOL. The accuracy of the results can be improved by tailoring the mesh density throughout the model geometry to include more mesh elements in regions of high field gradient.

Here's the example of bare PMMA on Si substrate. Figure 3.11 shows the calculated transmission spectra of 2μm bare PMMA film on silicon substrate at angle .

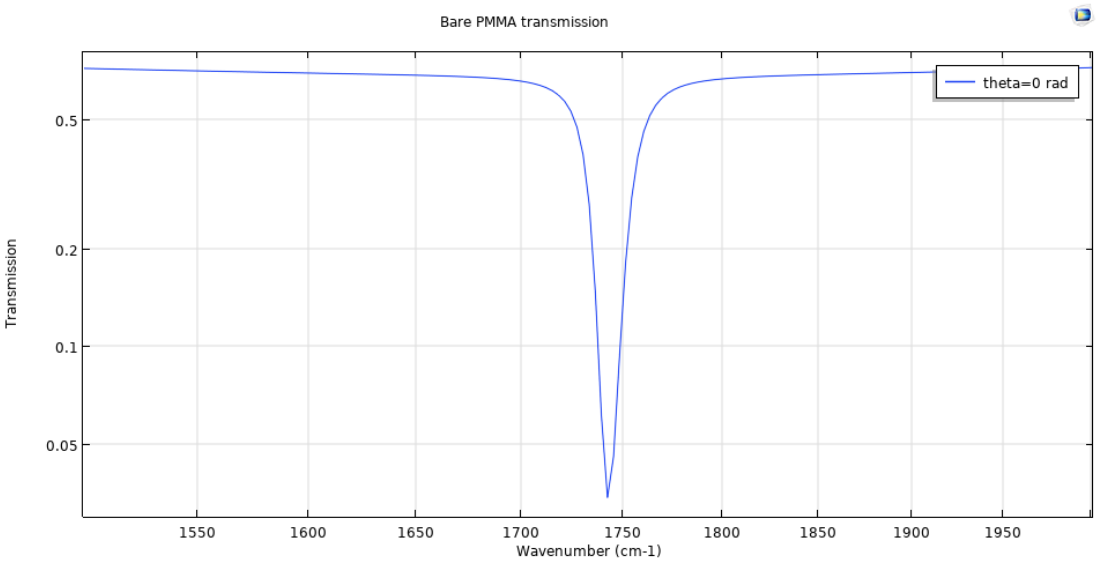

FIGURE 3.11: Transmission spectra of bare pmma on si substrate

PMMA material properties such as background permittivity, oscillator strength, resonance frequency, damping rate are defined using Drude Lorentz's model. The value of Si substrate is fixed refractive index value. For the calculations, electromagnetic frequency domain is chosen.

3.6 summary

In this chapter, I mentioned about working of all major experimental techniques used in this thesis. Later, I also focused specially on the use of COMSOL with an example.

In the next chapter, I will discuss about hybridization of multiple vibrational modes in cavity as well as in plasmonic structures.

Chapter 4

Hybridization of multiple vibrational modes

In this chapter, I will focus on strong coupling of multiple vibrational modes of different species with confined light fields, i.e. optical microcavity, plasmon mode. As in chapter 2 I introduced dispersion plots and the SPP, now I will talk more in detail about two systems, 1) optical microcavity 2) plasmon mode.

4.1 Introduction

In the infrared regime, hybridization of vibrational resonances associated with two distinct molecular species has also been reported recently [44, 61]. However, as far as I am aware, hybridization of different vibrational resonances of a single molecular species has not so far been reported. In this chapter, I present results of experiments that demonstrate such hybridization, thereby adding a potentially important component in the strong coupling toolbox, one that may further the degree of control possible over molecular vibrational states in any future polaritonic chemistry.

In this chapter, I have made use of two different types of confined light field. First I use the well-established planar optical microcavity, second I make use of the surface plasmon mode associated with a single metal surface. Surface plasmons on planar metal films have momenta that cannot be accessed easily by incident light, I employ grating coupling to overcome this problem, an approach previously explored for strong coupling of excitonic resonances [62]. In what follows I briefly describe the sample structure and material properties. The main probe I use to explore the coupling between vibrational resonances and the optical modes of confined light fields is to determine the dispersion of the polaritons involved. I describe how these data are acquired and present results from both types of cavity. I then discuss the modelling I have undertaken, both numerical and analytical, before summarising the findings.

I have divided this chapter into two sections. In the first section, I will focus on molecular vibrational mode study with an optical microcavity mode. Second section will focus on molecular vibrational mode study with a plasmon mode.

4.2 Optical microcavity mode

A schematic of the structure I used is shown in Figure 4.1. The optical microcavity was based on two gold mirrors 12 *nm* thick, the space between them being filled with PMMA so as to form a PMMA-filled planar microcavity.

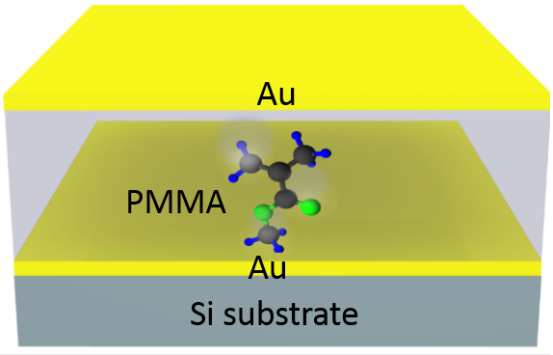

FIGURE 4.1: Schematics of the confined light field structures. An optical microcavity formed of two gold mirrors separated by a cavity-filling layer of the polymer PMMA, the substrate is a silicon wafer.

A thickness of 2 μm was chosen for the cavity thickness so as to ensure that the lowest order cavity resonance was close to the molecular vibrational resonances of interest.

To study interaction of the vibrational mode with the microcavity mode, I will first focus on a single vibrational mode and later on multiple vibrational modes.

4.2.1 single vibrational mode study

I chose the polymer PMMA as the molecular material. A sample infrared transmittance spectrum, acquired at normal incidence using FTIR, for a 1.0 μm film of PMMA on a silicon wafer substrate is shown in Figure 4.2.

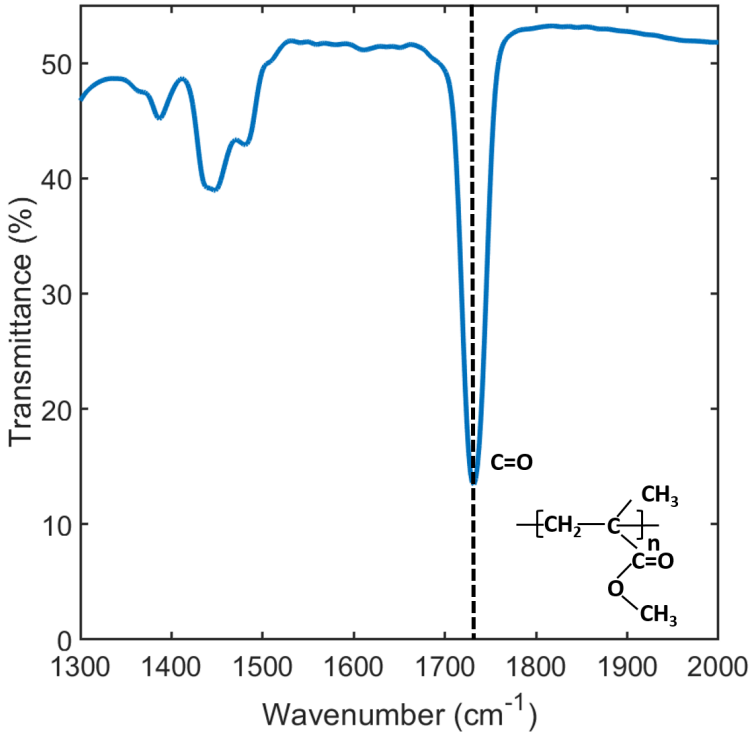

FIGURE 4.2: Normal incidence FTIR transmission spectra. The blue solid shows the measured transmittance of bare PMMA on a Si substrate. The dashed black lines represents C=O vibrational mode.

Setting the oscillator strength of the vibrational resonance in the PMMA to zero, a transmission dispersion plot of the resulting microcavity was calculated using COMSOL and is shown in Figure 4.3.

Strong absorption due to the C=O stretching mode is clearly seen at 1732 cm^{-1} [63, 64]. Although other resonance features are present, C=O has strong presence. The C=O stretch has a measured Gaussian Full Width Half Maximum (FWHM) of $\sim 30\ cm^{-1}$.

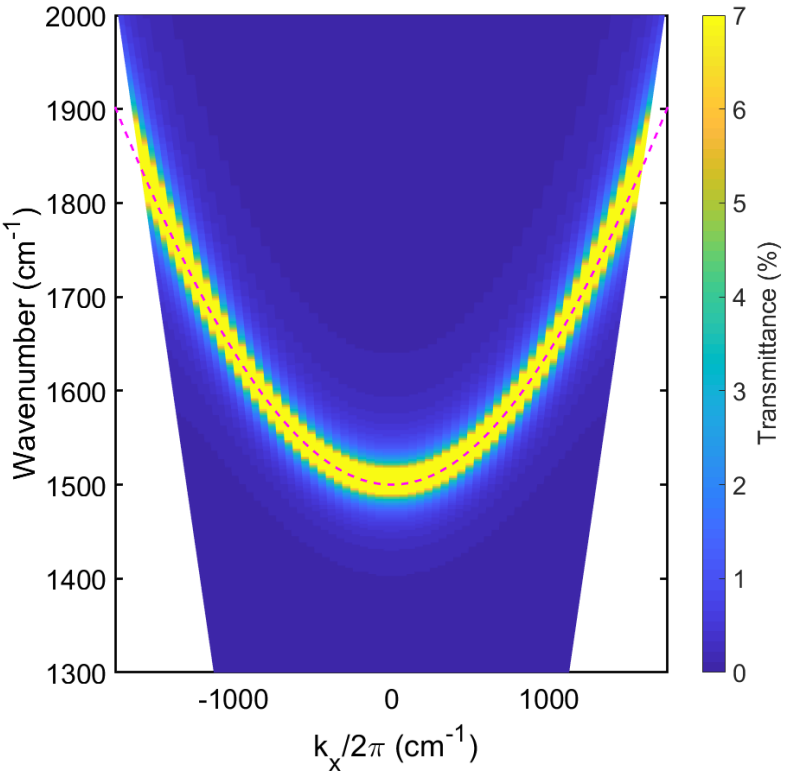

FIGURE 4.3: Numerically calculated dispersion plot for the bare cavity. Calculations were performed using COMSOL with the same parameters as in the main text except that here the oscillator strengths were set to zero.

The oscillator strength of the vibrational resonance in the PMMA was later added (Parameters and details in Chapter 3). The data in figure 4.4 show a clear anti-crossing at an angle of θ=0°, indicative of strong coupling between the C=O (1732 cm^{-1}) and the cavity mode. The Rabi splitting comes around 150 cm^{-1}. This provides clear evidence of strong coupling between the cavity mode and the molecular resonance.

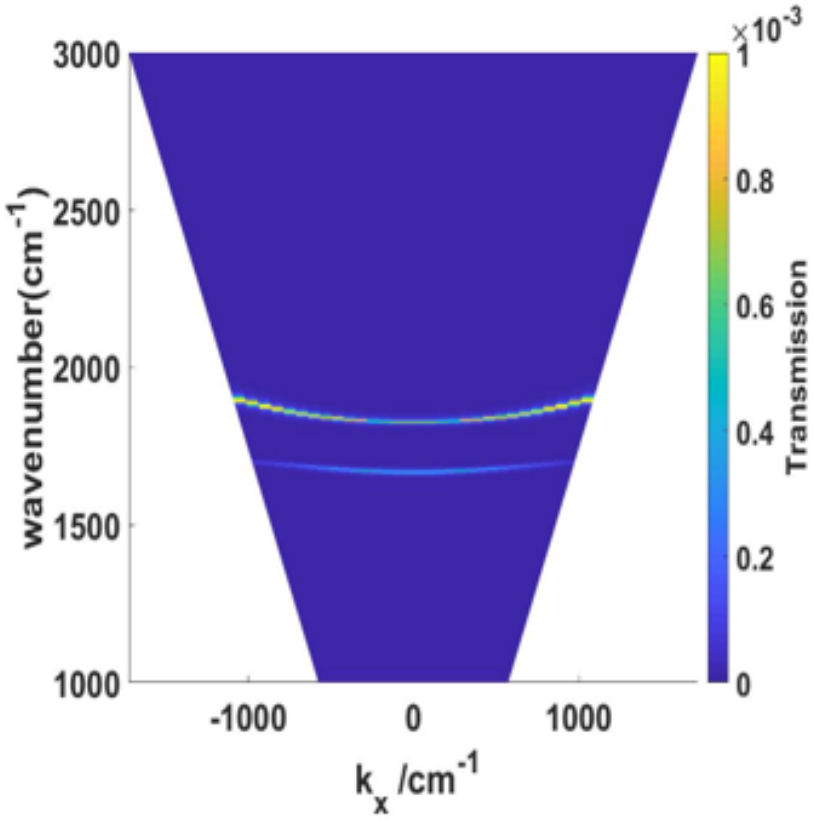

FIGURE 4.4: Dispersion plot calculated using COMSOL Multiphysics. Calculated transmittance is shown using a colour scale, and plotted as a function of wavenumber and in-plane wavevector k_x.

The electric field distribution of the C=O vibrational mode hybridised with the optical microcavity mode is shown in figure 4.5. For this calculation, the thickness of the gold films was chosen to be 12 nm and the thickness of the PMMA slab was 2 μm, the parameters used for the PMMA are again given in Table 4.1 The z value (y-axis) is the distance across the total sample in nanometers. The electric field profile is calculated for normal incidence. These data provide us with information about how much the electric field is confined in the cavity. In figure 4.5, the electric field is strong at the centre of the cavity and fades away towards the edges.

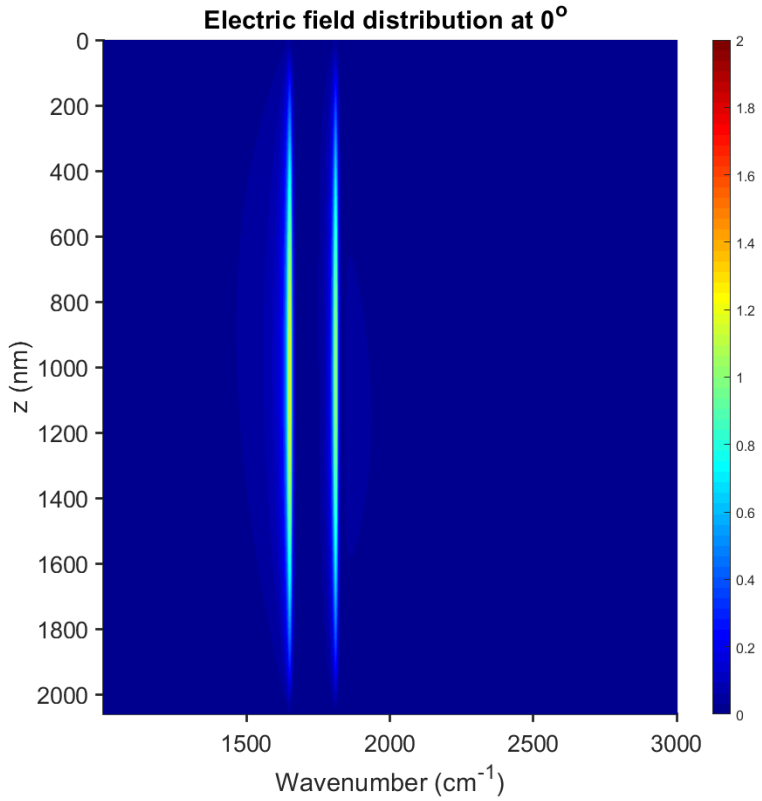

FIGURE 4.5: Electric field distribution in microcavity of single vibrational specie. Strong coupling between cavity and PMMA result into two hybrid modes, upper and lower mode.

4.2.2 Multiple vibrational mode

By reducing the frequency of the cavity mode it is possible to probe additional molecular resonances in the PMMA.

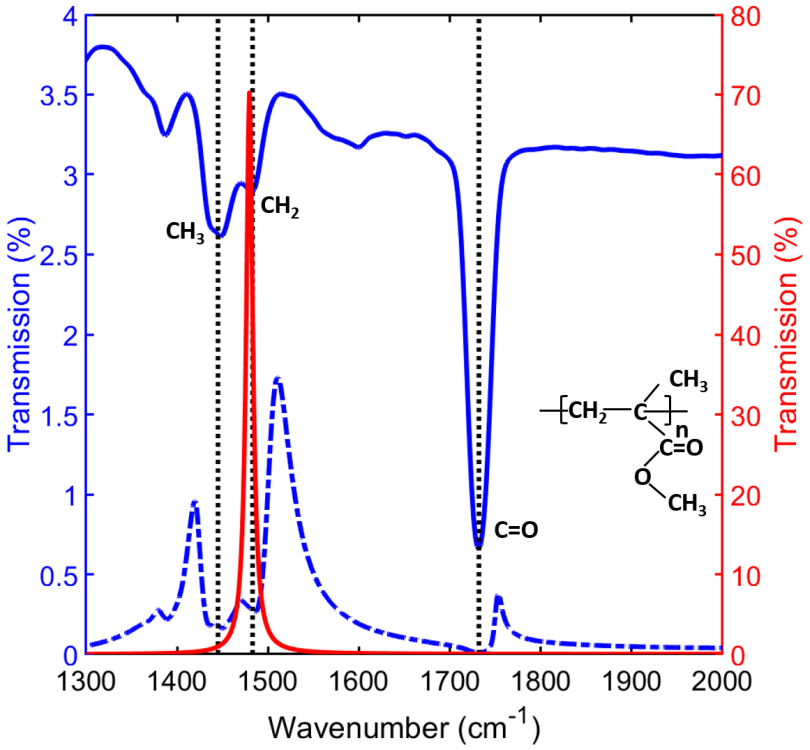

FIGURE 4.6: Normal incidence FTIR transmission spectra. The blue solid and dash-dotted curves show the measured transmittance of bare PMMA on a Si substrate and the measured transmittance of the cavity sample respectively. The red curve shows the numerically simulated transmittance of the bare cavity, as shown in Figure 4.1(a), calculated by assuming the vibrational resonances to have zero strength. The dashed black lines represent C=O, CH_2 and CH_3 vibrational modes.

In fact, many absorption features are present in the PMMA spectrum 4.6 in addition to the strong absorption due to the C=O stretching mode [63, 64]. The other features of interest in the present work are those that form the somewhat complex absorption band centred around 1445 cm^{-1}, arising primarily from a bending resonance associated with -CH_3 together with a band centred around 1481 cm^{-1}, arising primarily from a bending resonance associated with -CH_2

[63, 64]. Hereafter I will refer to these as the C=O, CH_3 and CH_2 resonances respectively.

For comparison the numerically calculated normal incidence transmittance of the bare cavity mode is also shown in figure 4.6 in red, whilst the normal incidence experimentally measured transmission of PMMA-filled cavity is shown as a blue dot-dashed curve.

To acquire dispersion plots I recorded FTIR spectra for a range of incident angles. All measurements were performed with a spectral resolution of 4 cm^{-1} and an angular resolution of 2 °. An example of a measured dispersion diagram is presented in Figure 4.7. Data were normalised with respect to a transmittance spectrum acquired with no sample present. The data in figure 4.7(a) show a clear anti-crossing at an angle of θ =50 °, indicative of strong coupling between the C=O (1732 cm^{-1}) and the cavity mode. The strength of the splitting relative to the modal widths is discussed below. Indeed, coupling of the C=O, CH_2, CH_3 modes to the same cavity mode leads to the formation of four polaritons bands: a lower polariton (L), a lower middle polariton (M1), an upper middle polariton (M2), and an upper polariton (U); these are shown as red, blue, green and magenta dashed lines in Figure 4.7a respectively.

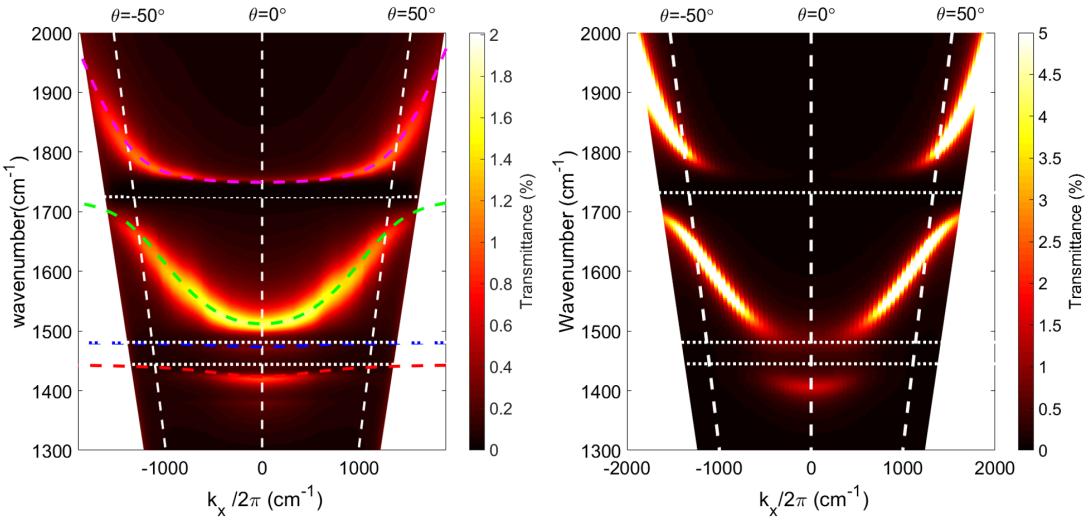

FIGURE 4.7: Dispersion plots for the cavity system. (a) Experimental data. The measured infrared transmittance of the sample shown in figure 4.1 is plotted as a function of frequency (cm^{-1}) and in-plane wavevector (k_x). The horizontal dashed grey lines indicate the energy of the C=O (1732 cm^{-1}), CH_2 (1481 cm^{-1}) and CH_3 (1445 cm^{-1}) vibrational resonances. The maximum polar angle for which these data were acquired was θ=70°. The angles of incidence equal to $\pm$ 50° are indicated as white dotted lines, and correspond to the angles at which anti-crossing of the cavity mode occurs with the C=O bond. Also shown are the calculated positions (coloured dashed lines) of the polariton branches from the coupled oscillator model: lower polariton (red), lower middle polariton (blue) upper middle polariton (green) and upper polariton (magenta). (b) Numerically modelled data using COMSOL Multiphysics. The calculated transmittance is shown as a function of frequency (cm^{-1}) and in-plane wavevector k_x.

The electric field distribution of multiple vibrational modes hybridised with the optical microcavity mode is shown in figure 4.8. For this calculation, a thickness of gold film was chosen as 12 nm and the thickness of the PMMA slab was 2.26 μm. The electric field for CH_3 is weak at the cavity centre compared to the CH_2 and CH_3 modes. This is mainly because the damping rate of the CH_3 mode is higher that of the CH_2 and C=O modes (more details in table 4.1).

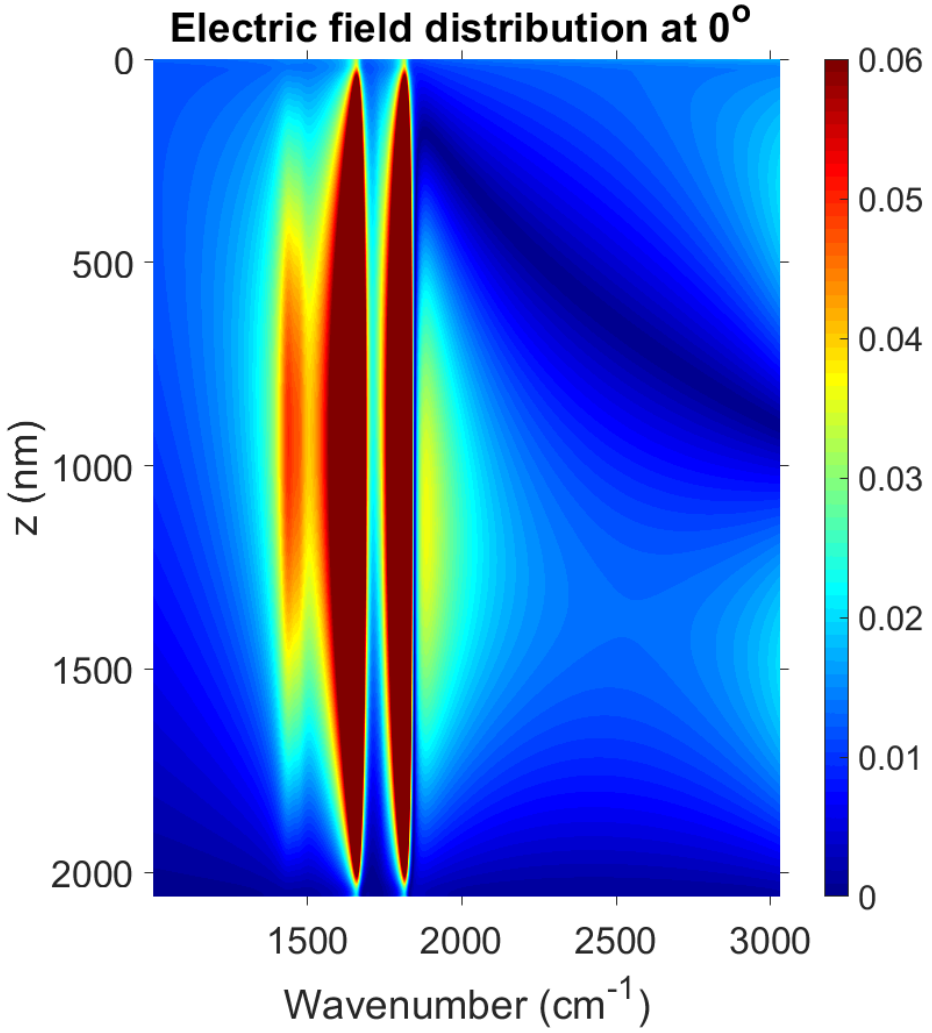

FIGURE 4.8: Electric field distribution in microcavity of multiple vibrational species. The C=O bond at 1732 cm^{-1} has strong electric field presence while CH_3 has relatively weaker electric field presence.

To gain greater insight into these data I undertook both numerical and analytical modelling. For the numerical modelling I used a commercial finite-element package (COMSOL Multiphysics[1], details in methods section below) whilst for analytical modelling we used a four coupled oscillator model.

First the numerical modelling. For the material parameters, I made use of a Drude model for the optical response of gold,

$$\varepsilon(\omega) = \varepsilon_b - \frac{\omega_p^2}{\omega^2 + i\gamma\omega}, \tag{4.1}$$

with parameters taken from Olmon *et al.* [55], specifically, $\omega_p = 1.29 \times 10^{16}\ rad\ s^{-1}$, and $\gamma = 7.30 \times 10^{13}\ rad\ s^{-1}$, with $\varepsilon_b = 1.0$. For the PMMA we used a model based on three Lorentz oscillators,

$$\varepsilon(\omega) = \varepsilon_\infty + \sum_j^3 \frac{\omega_j^2 f_j}{\omega_j^2 - \omega^2 - i\gamma_j\omega}, \tag{4.2}$$

with parameters given in table 4.1,

vibrational mode	f_j	$\omega_j(\ rad\ s^{-1})$	$\gamma_j(\ rad\ s^{-1})$
C=O (j=1)	0.0165	3.26248×10^{14}	5×10^{12}
CH_2 (j=2)	0.0047	2.7896×10^{13}	9.3×10^{12}
CH_3 (j=3)	0.0087	2.72187×10^{13}	12×10^{12}

TABLE 4.1: Lorentz oscillator model parameters for the PMMA vibrational modes

and with ε_∞ taken to be 1.99. The parameters for silicon in the infrared are based on data compiled by Edwards [56] and are taken to be, $\varepsilon = 11.76 + 0.001i$, whilst for air we took $\varepsilon = 1.0$. Finally, for CaF_2, data were taken from Malitson [57], at $5.0\mu m$ the refractive index is $n = 1.40$.

[1]COMSOL Multiphysics® v. 5.4. www.comsol.com. COMSOL AB, Stockholm, Sweden.

Employing these parameters I used COMSOL to evaluate numerically the transmittance of the structure shown in Figure 4.1a as a function of frequency and in-plane wavevector, these data are shown in Figure 4.7(b). The data show a good match to those acquired from experiment (shown in Figure 4.7(a)), giving me confidence that I have selected appropriate modelling parameters. The difference in absolute transmittance values between the experimental data, Figure 4.7(a), and the modelled data, Figure 4.7(b), is attributed to the slightly rough nature of the reverse side of the Si wafer substrate used in our experiments.

4.3 Plasmon mode

Microcavities are just one class of structure that produce confined light fields, I also explored a second type of confined light field, that associated with a surface plasmon [65]. I noted earlier that to couple to such modes with incident light requires some kind of momentum matching. In contrast with the attenuated total reflection technique employed by Memmi *et al.* [28] I made use of grating coupling [66], a technique previously used with great success by Vasa *et al.* to observe Rabi oscillations associated with excitonic strong coupling [67].

4.3.1 Single vibrational mode specie

A schematic of the sample structure I used is shown in Figure 4.9. The plasmonic surface is provided by a 100 nm gold film fabricated in the form of a grating using electron beam lithography.

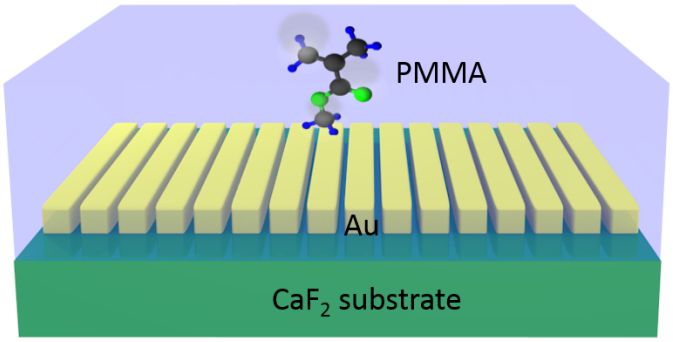

FIGURE 4.9: Schematics of the confined light field structures. A 1D metal grating supporting a surface plasmon mode, on top if a CaF_2 substrate, and overlain by a layer of PMMA.

The grating period was 7.2 μm with a 1 μm gap on a CaF_2 substrate. This choice of period was made to enable coupling of incident light to the surface plasmon mode on the Au/PMMA interface at a convenient angle of incidence.

Setting the oscillator strength of the vibrational resonance in the PMMA to zero, a transmission dispersion plot of the resulting plasmonic mode was calculated using COMSOL and is shown in figure 4.10. All the parameters chosen for PMMA are shown in Table 4.1

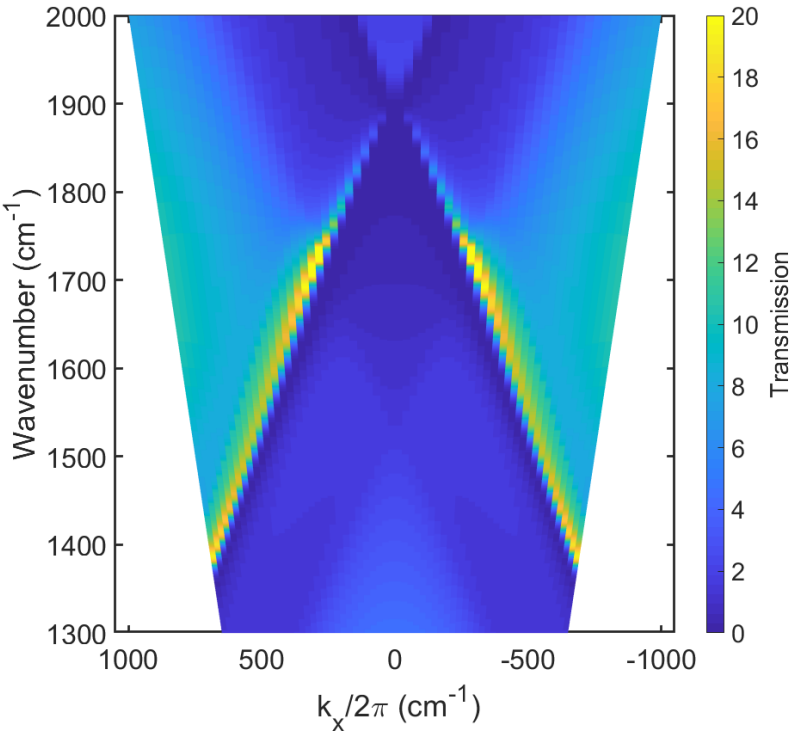

FIGURE 4.10: Numerically calculated dispersion plot for the bare grating. Calculations were performed using COMSOL with the same parameters as in the main text except that here the oscillator strengths were set to zero.

The value of oscillation strength was later set to non- zero for the calculation (Parameters details in Chapter 3). A calculated dispersion plot of the plasmonic mode for a range of incident angles was acquired and shown in figure 4.11. It shows strong coupling of C=O vibrational mode with plasmonic mode.

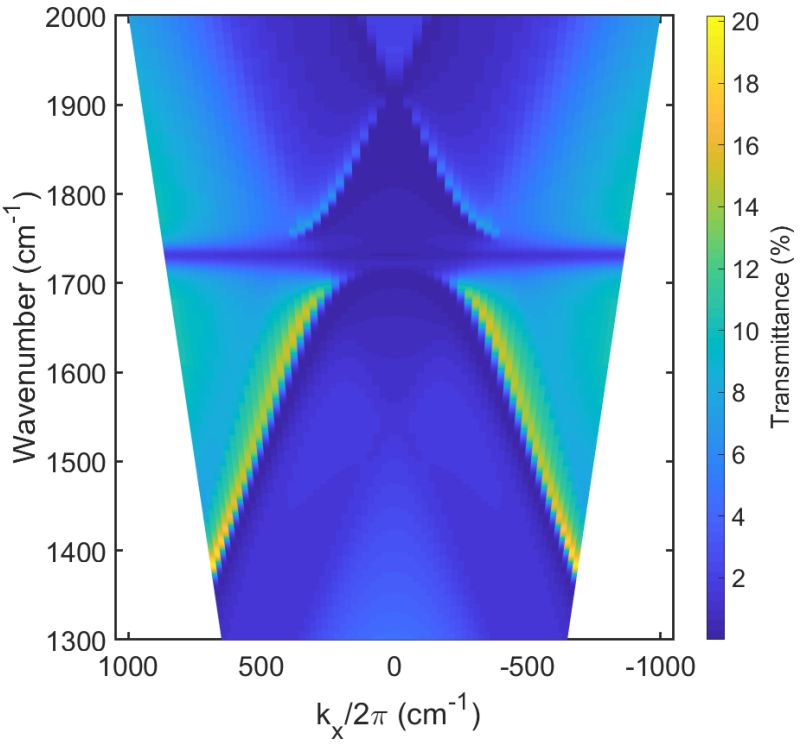

FIGURE 4.11: Dispersion plot calculated using COMSOL Multiphysics. Calculated transmittance is shown using a colour scale, and plotted as a function of wavenumber and in-plane wavevector k_x. The dispersion plot is showing coupling between vibrational mode and plasmon mode

4.3.2 Multiple vibrational mode species

FTIR spectra for a range of incident angles were acquired, the results, in the form of a dispersion plot, are shown in Figure 4.12 (a). Again, as for the microcavity, I also calculated a dispersion plot using numerical modelling, shown in Figure 4.12 (b). There is broad agreement between the numerically modelled data and the experiment, some of the differences in detail might be attributed to variations in the grating across the ∼2 mm spot size used in the FTIR measurements.

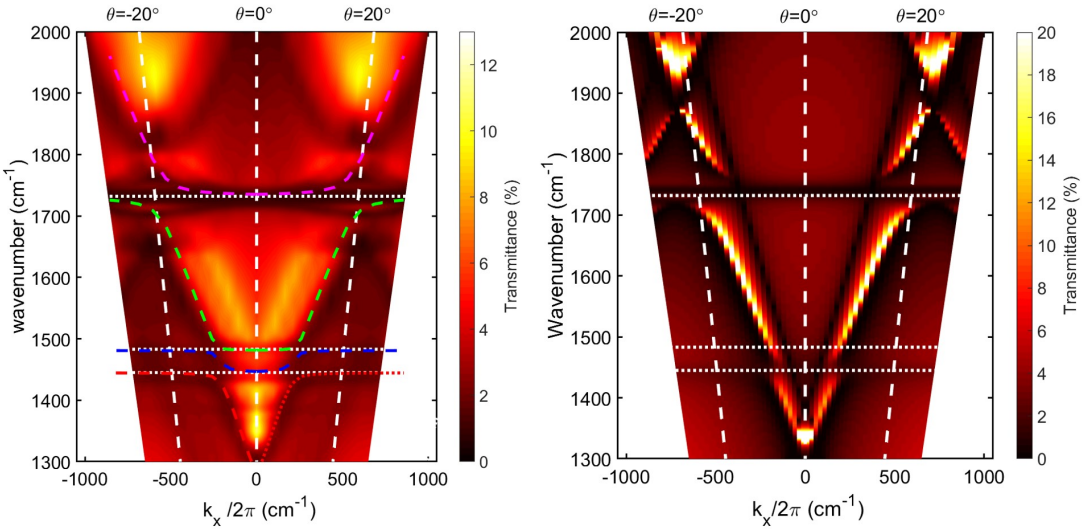

FIGURE 4.12: Dispersion plots for the plasmon system. (a) Dispersion diagram derived from experimental data. Infrared transmittance of the plasmon sample shown in Figure 4.9 are shown as a function of frequency (cm^{-1}) and in-plane wavevector (k_x). The horizontal grey dashed lines indicate the energy of the C=O (1732 cm^{-1}), CH_2 (1481 cm^{-1}), and CH_3 (1445 cm^{-1}) vibrational resonances. The maximum polar angle for which these data were acquired was θ=30°. Angles of incidence equal to $\pm$ 20° are indicated as white dotted lines, and correspond to the angles at which anti-crossing of the plasmon mode occurs with the C=O resonance. Also shown are the calculated positions (coloured dashed lines) of the polariton branches from the coupled oscillator model: lower polariton (red), middle polariton (blue) and upper polariton (magenta). (b) Numerically modelled data using COMSOL Multiphysics. Calculated transmittance is shown using a colour scale, and plotted as a function of frequency cm^{-1} and in-plane wavevector k_x.

4.4 Analytical model study

Next, for the analytical model, the four oscillators are the confined light field and the three vibrational modes, C=O, CH_2 and CH_3. The model can be captured by the following matrix equation,

$$\begin{pmatrix} E_{\mathrm{CL}} & \Omega_{\mathrm{C=O}}/2 & \Omega_{\mathrm{CH_2}}/2 & \Omega_{\mathrm{CH_3}}/2 \\ \Omega_{\mathrm{C=O}}/2 & E_{\mathrm{C=O}} & 0 & 0 \\ \Omega_{\mathrm{CH_2}}/2 & 0 & E_{\mathrm{CH_2}} & 0 \\ \Omega_{\mathrm{CH_3}}/2 & 0 & 0 & E_{\mathrm{CH_3}} \end{pmatrix} \begin{pmatrix} a_{L,M1,M2,U} \\ b_{L,M1,M2,,U} \\ c_{L,M1,M2,U} \\ d_{L,M1,M2,U} \end{pmatrix} = E_{L,M1,M2,U} \begin{pmatrix} a_{L,M1,M2,U} \\ b_{L,M1,M2,U} \\ c_{L,M1,M2,U} \\ d_{L,M1,M2,U} \end{pmatrix}, \tag{4.3}$$

where E_{CL} is the energy of the confined light field, i.e. the cavity/plasmon mode as appropriate, and is a function of the in-plane component of the wavevector, k_x. $E_{\mathrm{C=O}}$ is the energy of the C=O vibrational mode, $E_{\mathrm{CH_2}}$ is the energy of the CH_2 vibrational mode and $E_{\mathrm{CH_3}}$ is the energy of the CH_3 vibrational mode. The constants $\Omega_{\mathrm{C=O}}/2$, $\Omega_{\mathrm{CH_2}}/2$ and $\Omega_{\mathrm{CH_3}}/2$ are the coupling strength of E_{CL} with $E_{\mathrm{C=O}}$, $E_{\mathrm{CH_2}}$ and $E_{\mathrm{CH_3}}$ respectively. The eigenvalues $E_{L,M1,M2,U}$ of this matrix correspond to the lower (L), lower middle (M1) upper middle (M2), and upper (U) polariton bands. To fit these polariton bands to the measured dispersion, I set the three coupling strengths, $\Omega_{\mathrm{C=O}}$, $\Omega_{\mathrm{CH_2}}$ and $\Omega_{\mathrm{CH_3}}$ as free parameters. The composition of the polariton bands are described by the generalized Hopfield coefficients $|a_{L,M1,M2,U}|^2$, $|b_{L,M1,M2,U}|^2$, $|c_{L,M1,M2,U}|^2$ and $|d_{L,M1,M2,U}|^2$ where $|a_{L,M1,M2,U}|^2 + |b_{L,M1,M2,U}|^2 + |c_{L,M1,M2,U}|^2 + |d_{L,M1,M2,U}|^2 = 1$. The polariton bands can be written as $|a_{L,M1,M2,U}|^2 |E_{CL}\rangle + |d_{L,M1,M2,U}|^2 |E_{\mathrm{C=O}}\rangle + |b_{L,M1,M2,U}|^2 |E_{\mathrm{CH_2}}\rangle + |c_{L,M1,M2,U}|^2 |E_{\mathrm{CH_3}}\rangle$, so that the Hopfield coefficients measure the extent to which the cavity mode, the C=O mode, the CH_2 and the CH_3 modes contribute to each polariton band.

I found that the best fit to my cavity data was obtained with: $\Omega_{C=O} = 150\ cm^{-1}$, $\Omega_{CH_2} = 40\ cm^{-1}$ and $\Omega_{CH_3} = 70\ cm^{-1}$ and ; these values agree well with those seen in the experimental data, Figure 4.7a. These Rabi splittings are greater than a) the measured spectral width of the respective C=O (60 cm^{-1}), CH_2 (30 cm^{-1}), and CH_3 (30 cm^{-1}) vibrational modes respectively, and b) the width of the bare cavity mode – measured using an off-resonance cavity to be 45 cm^{-1}. These data thus indicate that my microcavity system is in the strong coupling regime [68]. The results from this coupled oscillator model are shown in Figure 4.13, in Figure 4.13(a) experimental data (circles) are also shown corresponding to the maxima of the transmittance spectra shown in Figure 4.7a. In Figure 4.13a I also show the positions of the uncoupled (bare) microcavity, and the C=O, the CH_2, the CH_3 resonances as dotted lines.

In addition to allowing extraction of the coupling strengths, the coupled oscillator model enables us to determine the contribution of the different resonances to each polariton band through the Hopfield coefficients. In particular I can use this approach to examine the contribution that the different vibrational modes make to the upper middle polariton (M2). In Figure 4.13b I show the contribution of the cavity mode, the C=O mode, the CH_2 mode, CH_3 mode to the upper middle polariton band M2 as a function of in-plane wavevector. At in-plane wavevector $k_x \sim 530\ \mathrm{cm}^{-1}$ I see that the M2 polariton has contributions of approx. 33% from the C=O, CH_2 and CH_3 modes (equal contributions of 11% each), the remaining 67% being photonic (cavity mode) in character. These data show that the upper middle polariton involves hybridization of the three different vibrational resonances associated with the same molecular unit.

Again, and as for the microcavity system, I also modelled the surface plasmon system using the four coupled oscillator model. Here the surface plasmon mode replaces the cavity mode as one of the oscillators, together with the three

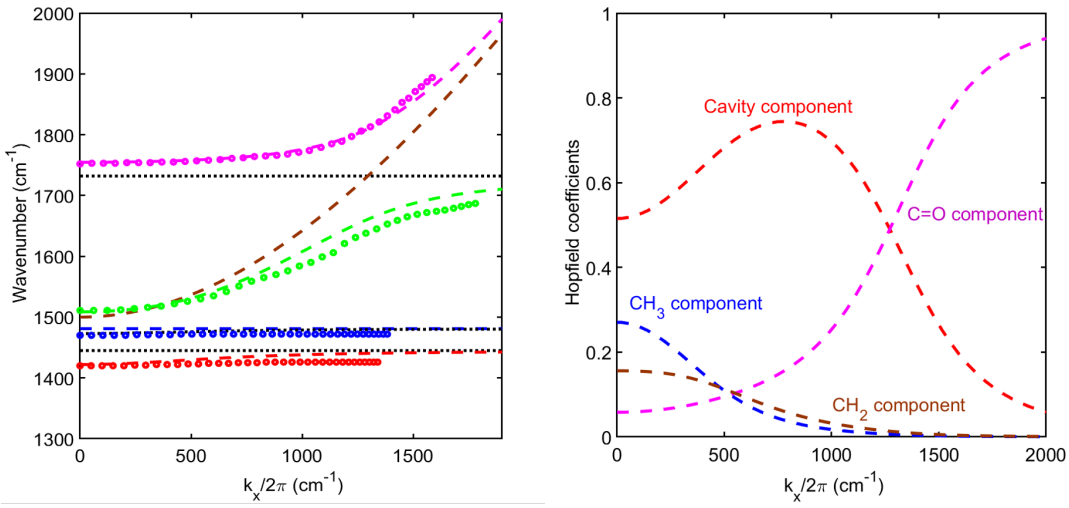

FIGURE 4.13: Coupled oscillator model for the planar cavity. (a) Comparison between experimental (circles) and coupled oscillator model (dashed lines) for: the lower polariton (L) (red), the lower middle polariton (M1) mode (blue), the upper middle polariton (M2) mode (green) and the upper polariton (U) mode (magenta) for grating mode. The horizontal dotted lines in black show the energies of the C=O, CH_2 and CH_3 vibrational modes respectively. The bare cavity mode is shown as a brown dashed line. (b) Hopfield coefficients of the upper middle polariton (M2). The contribution of the cavity mode is shown in red, the C=O mode in magenta, the CH_2 mode in brown and the CH_3 mode in blue. The data shown were found by calculating the eigenvalues and eigenvectors of equation 4.3

vibrational modes, C=O, CH_2 and CH_3. For the plasmon mode I took the uncoupled dispersion from numerically modelled data in which the oscillators strengths were set to zero. The best match between the eigenvalues obtained from this approach and those seen in the experimental data, Figure 4.12, was obtained with: $\Omega_{C=O} = 75\ cm^{-1}$, $\Omega_{CH_2} = 20\ cm^{-1}$ and $\Omega_{CH_3} = 35\ cm^{-1}$. The resulting polariton frequencies are plotted as coloured dashed lines in Figure Figure 4.12a. These splittings are approx. half those obtained from the planar microcavity, the microcavity mode appears to offer a higher (average) electric field strength [68]. Again, these splittings need to be compared to: a) the measured spectral width of the respective C=O (60 cm^{-1}), CH_2 (30 cm^{-1}), and CH_3 (30 cm^{-1}) vibrational modes respectively, and b) the width of the bare

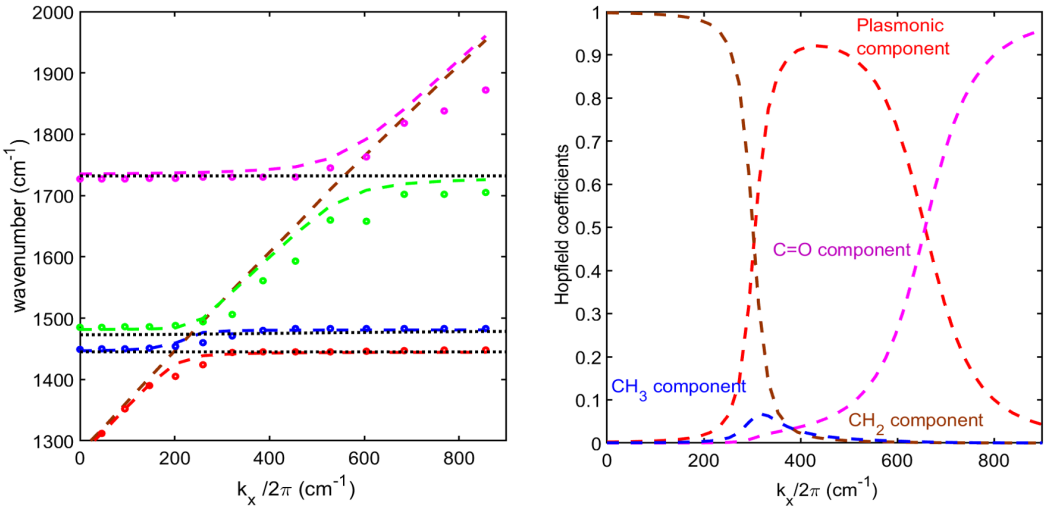

FIGURE 4.14: Coupled oscillator model for the plasmon system. (a) Comparison between experimental data (circles) and the coupled oscillator model (dashed lines) for: the lower polariton (L) (red), the lower middle polariton (M1) mode (blue), the upper middle polariton (M2) mode (green) and the upper polariton (U) mode (magenta). The horizontal dotted lines (black) show the energies of the C=O, CH_2 and CH_3 vibrational modes respectively. The bare plasmon mode is shown as a brown dashed line. (b) Hopfield coefficients of the upper middle polariton (M2). The contribution of the plasmon mode is shown in red, the CH_3 mode in blue, the CH_2 mode in brown and the C=O mode in magenta. The data shown were found by calculating the eigenvalues and eigenvectors of equation 4.3

cavity mode, 45 cm^{-1}. I see that for the plasmon system only the splitting associated with the C=O vibrational resonance fully satisfies the strong coupling condition.

In Figure 4.14 I show the calculated Hopfield coefficients for the lower middle polariton in the plasmon system. I see that although the lower middle polariton does have some character inherited from all three vibrational resonances, their contribution is relatively small, around $\sim$ 5% each. This lower contribution than for the cavity mode might also be attributed to the lower field strength of the plasmon mode as sampled by the PMMA film. It is also clear that the match between data and model for the plasmon system (Figure 6(a) is poorer than it

was for the microcavity system (Figure 4(a)). Several factors may contribute to this: first, more than one diffracted plasmon mode contributes to the data shown in Figure 5(a), for simplicity I only included one of them; second, the dispersion of the plasmon mode depends sensitively on the profile of the grating [40], for simplicity I have taken a simple rectangular profile here, and I have ignored any band distortions due to grating coupling of plasmon modes; third, determining the position of the plasmon using dispersion data from transmittance data can be problematic owing to the Fano-like character of the features involved. Despite these limitations, the coupled oscillator reproduces reasonably well the anti-crossings seen in experiment.

4.5 Summary

In summary, my results show that distinct molecular vibrational resonances, here associated with C=O, CH_2 and CH_3 may be hybridized by strong coupling each of them to the same cavity/plasmon mode. The extent to which the three vibrational resonances contribute to the upper middle polariton in the cavity system, $\sim$ 11%, is comparable to that in the first report of hybridizing two excitonic resonances via strong coupling [19]. For the case of the plasmon mode I found that only the coupling with the C=O bond fully met the strong coupling criteria, and that the associated polariton, although involving all three molecular resonances, only did so to the extent of 5%. Nonetheless, it is clear that strong coupling can hybridize multiple different molecular resonances of a single molecular unit, and that consequently strong coupling offers an interesting means by which to control molecular systems. Hybridized vibrational resonances may also be interesting in the context of vibrationally dressed states [12, 69]. A challenge for the strong coupling community is to devise means by which to increase the extent of hybridization possible. Increasing the

extent of hybridization might be achieved by employing confined light fields that exhibit greater field enhancement than the planar metal-clad cavity used here. Possible routes to achieving this include planar cavities that use dielectric stacks rather than metal mirrors [70], and localised resonances [39]. Care will be needed though since there is often a trade-off between field enhancement and cavity volume to consider [71]. An interesting alternative may be to explore a hierarchical approach that mixes plasmonic resonances and vibrational ones, much as was recently accomplished for exciton resonances by Bisht *et al.* [72].

In the next chapter, I will focus on interaction of surface plasmon and the surface plasmon stop bands with molecular vibrations.

Chapter 5

Vibrational strong coupling with surface plasmons and the presence of surface plasmon stop bands

In this chapter, I will discuss vibrational strong coupling in the context of plasmonic structures that involve modified band structures. In chapter 4 I looked at vibrational strong coupling involving the confined light fields offered by surface plasmons. In the present chapter I will explore how the periodic micro-structure used to access the plasmon mode does more than just provide access, i.e. momentum matching–as I shall see, the periodic micro-structure also modifies the plasmon, and hence polariton, bands.

5.1 Introduction

It is useful to first look at the modes supported by the structures investigate here, this is done through a numerical simulation performed using the commercial finite-element software COMSOL. Figure 5.1(a) shows a schematic of the system I consider, a 1D gold grating on a silicon substrate, overlain with a film of the

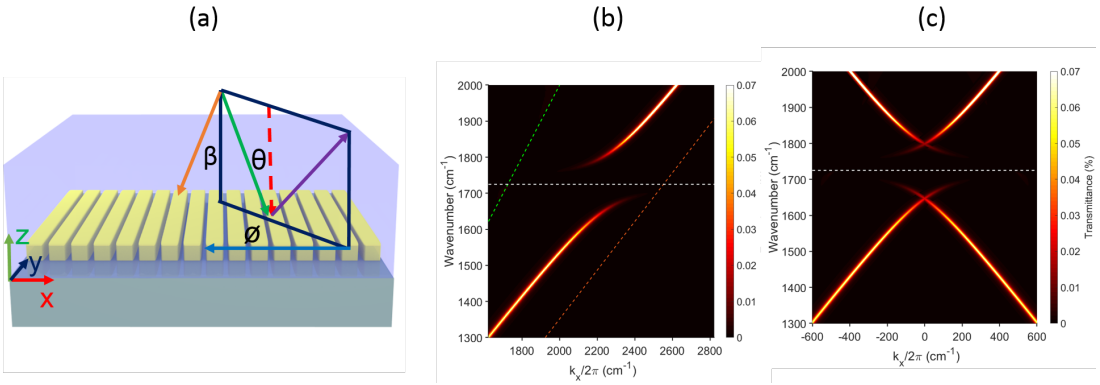

FIGURE 5.1: (a) Schematic of sample geometry shows a schematic of the gold grating samples used in this work. A gold grating was formed on top of a silicon substrate, upon which was deposited a layer of the polymer PMMA. Also shown is the plane of incidence, the green arrow represents the incident light direction, the black arrow the reflected direction. The polar angle of incidence θ and the azimuthal angle ϕ, are as shown. For all measurements and calculations the incident IR light was TM polarised, i.e. the electric field was in the plane of incidence. (b) Calculated dispersion for a planar version (no grating) of my structures; the system comprises a silicon substrate, 100 nm of gold (the plasmon-supporting metal), a 2 μm layer of the polymer PMMA and air as the superstrate. The calculated (COMSOL) transmittance is shown as a function of frequency (cm^{-1}) and in-plane wavevector on a colour scale, high transmittance indicates a mode of the system. The material parameters are given at the end of the main text. The green and red dashed lines represent the air light-line and the PMMA light-line respectively. The horizontal white dashed line at 1732 cm^{-1} represents C=O vibrational mode. Notice that the plasmon mode, and the anti-crossing with the molecular resonance, is beyond the air light-line. (c) Here I have taken the data from (b) and superimposed a shifted and folded copy so as to produce a dispersion plot to give an idea of what I expect for a grating rather than a planar structure. The grating period was taken as 4.5 μm, for which $k_x/2\pi = 1/\lambda_g = 2222\ cm^{-1}$.

polymer PMMA. Specifically I looked at the transmission of a planar stack comprising a silicon substrate, a 100 nm gold film (the plasmon-supporting metal), a 2 μm layer of the polymer PMMA, and finally air as the superstrate. The transmittance was calculated as a function of frequency and in-plane wavevector, and is plotted on a colour scale. The surface plasmon modes can be seen as peaks in the transmittance for p-polarised (TM) incident infrared light–plasmon modes on planar surfaces are p-polarised. The gold/PMMA plasmon mode is clearly seen in Figure 5.1(b) and (c), and lies, as expected, between the air and the PMMA light lines. Indeed, this plasmon mode always lies beyond the air light-line and it is for this reason that some means of momentum matching is required if this mode is to be observed in a reflection/transmission experiment. This calculation also shows the splitting of the plasmon mode at a frequency equivalent to 1732 cm^{-1}, a direct result of the interaction between the plasmon mode and the molecular vibrational resonance in PMMA.

Recently Memmi *et al.* used prism coupling to provide momentum matching and thus probe the hybridization of surface plasmons with molecular vibrational resonances [28]. Here, as in chapter 4, I adopt an alternative approach, that of grating coupling [73]. I chose to make my grating in the form of a metal stripe array, i.e. a periodic sequence of metal strips, see Figure 5.1 (a). The relevant fabrication techniques were discussed in chapter 3. To facilitate coupling to the surface plasmon mode at convenient angles of incidence, I chose a period of 4.5 μm.

It is useful first to try and model what the dispersion will look like using COMSOL. Next I wished to see the effect of the vibrational resonance on the dispersion. To do this I re-introduced the oscillator strength of the molecular (C=O) resonance into my model (more details in Chapter 3). The results of this calculation are shown in the left-hand panel of Figure 5.2 (a), hybridization

between the plasmon mode and the molecular vibrational resonance can now be seen. In addition I see that the unperturbed vibrational resonance is still clearly evident, this is the horizontal dark (low transmittance) feature at 1732 cm^{-1}. As I will see below (Figure 5.5), this is because there are many regions of the PMMA film that do not couple well to the surface plasmon mode.

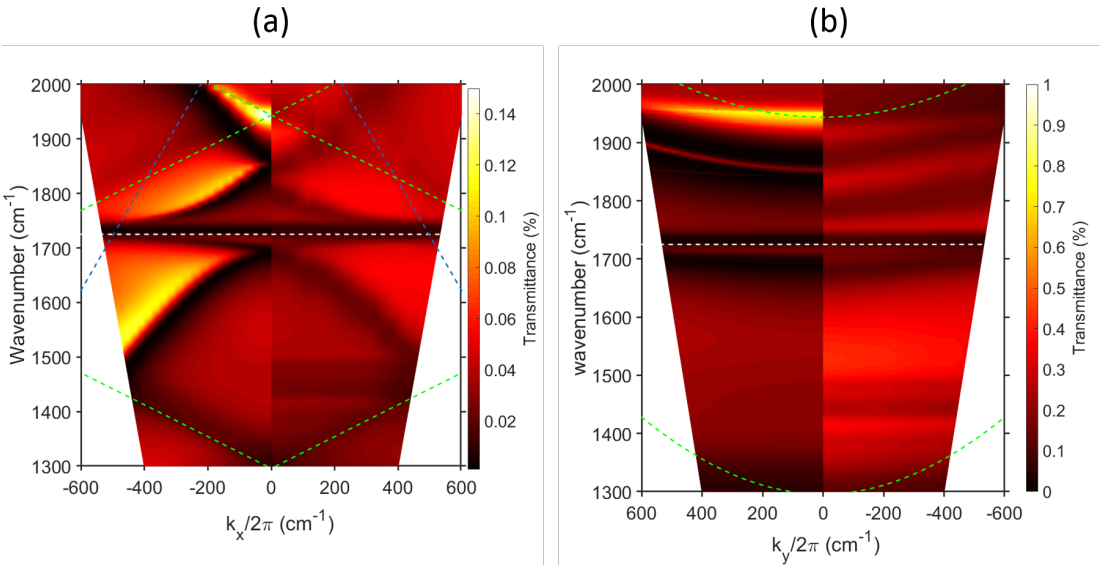

FIGURE 5.2: (a) Surface plasmon dispersion for $\phi = 0°$. On the left-hand side are numerically calculated transmittance data for TM polarised light, on the right-hand side are experimentally measured data; both show coupling between the vibrational resonance and the plasmonic mode. The maximum polar angle for these data is 18°. The period of the grating is 4.5 μm with a 1 μm gap between metal stripes. The PMMA thickness is 1.5 μm and $\theta = 1°$. The dashed blue and green lines are the ± 1 scattered air and $\pm 2, 3$ scattered silicon light-lines respectively, the white dashed line indicates the position of the C=O resonance. The calculated data have been scaled by a factor of 0.1 to allow easy comparison with the experimental data, as discussed in the text. The PMMA thickness is 1.5 μm, and $\phi = 0°$. (b) Dispersion for $\phi = 90°$. On the left-hand side are numerically calculated transmittance data for TM polarised light, on the right-hand side are experimentally measured data. Again, both show coupling between the vibrational resonance and the plasmonic mode. The maximum polar angle for these data is 18°. The period of the grating is 4.5 μm with a 1 μm gap between metal stripes. The PMMA thickness is 1.5 μm and $\beta = 1°$. The green dashed lines represents the ± 2 and ± 3 scattered Si light lines, the white dashed line indicates the position of the C=O resonance. As for Figure 5.2, the calculated data have been scaled by a factor of 0.1 to allow easy comparison with the experimental data.

Using FTIR I also acquired transmittance data from a sample nominally the same as that shown schematically in Figure 5.1 (a), in my sample the PMMA thickness was 1.5 μm. The results of these measurements are shown in Figure 5.2

(a) (right half), where again, transmittance is shown as a function of frequency (ω) and in-plane wavevector k_x. Note that in Figure 5.2 (a) the calculated data have been scaled by a factor of 0.1. This has been done to facilitate comparison of experimental and calculated data; in the experiment, the scattering nature of the rear side of the Si wafer used as a substrate reduces the overall measured transmittance. The first thing to note when comparing the experimental data with the calculated data is the broad agreement about the presence and extent of the anti-crossing of the plasmon mode with the C=O vibrational resonance.

In addition to the anti-crossing of the plasmon mode and the C=O vibrational resonance, at $k_x \sim 0$ I see an additional small splitting of the surface plasmon mode, at a frequency of $\sim 1830\ cm^{-1}$. Where scattered surface plasmon modes cross (on a dispersion diagram) stop bands may occur, their presence depending on the details of the grating profile [40]. Looking at the data in Figure 5.2 (a) it appears that a surface plasmon stop band, around $\sim 1830\ cm^{-1}$ has been produced. To further investigate this I measured the dispersion for a plane of incidence for which $\phi = 90°$; such a configuration maps out the modes for which $k_x = 0$, thus enabling the stop-band position to be tracked as a function of k_y, Figure 5.2 (b) (right half) is the result of such measurements. As a comparison, numerically calculated data for the same situation, i.e. $\phi = 90°$, are shown in Figure 5.2 (b) (left half). Both experimental data and calculated data show surface plasmon stop bands that gradually rise in frequency as $|k_y|$ is increased away from zero, tracking the expected dispersion for this configuration, as given by the third-order scattered Si light-line (shown as a green dashed line in the figure). Also evident in the experimental data in Figure 5.2 (b) (and indeed in Figure 5.2 (a)) are additional vibrational resonances for frequencies around $\sim 1460\ cm^{-1}$. These are due to CH_3 and CH_2 resonances that are not included in the model I have used here [63, 64], see also Figure 5.1b. This was earlier

discussed in chapter 4.

5.2 Surface plasmon stop bands and band gaps

A feature of surface plasmon stop bands and band gaps (a band gap implies that for some range of frequencies a stop band exists for all in-plane directions) is that coupling to the band edges is sensitive to the way the sample is illuminated [40]. To investigate this I calculated the line spectra associated with the transmittance for normal incidence, i.e. $\theta = 0°$, and near-normal incidence, $\theta = 1°$, these data are shown in Figure 5.3. For these data the azimuthal angle was $\phi = 90°$. I see that transmittance minimum at 1800 cm^{-1} and associated with the lower surface plasmon stop band is visible for off-normal incidence (red curve) but not for normal incidence (blue curve). This is consistent with the symmetry of the charge and field distributions expected in this geometry [40]. Careful observation of the data in Figure 5.3 shows that something similar happens where the scattered plasmon modes cross at $\sim$ 1670 cm^{-1}.

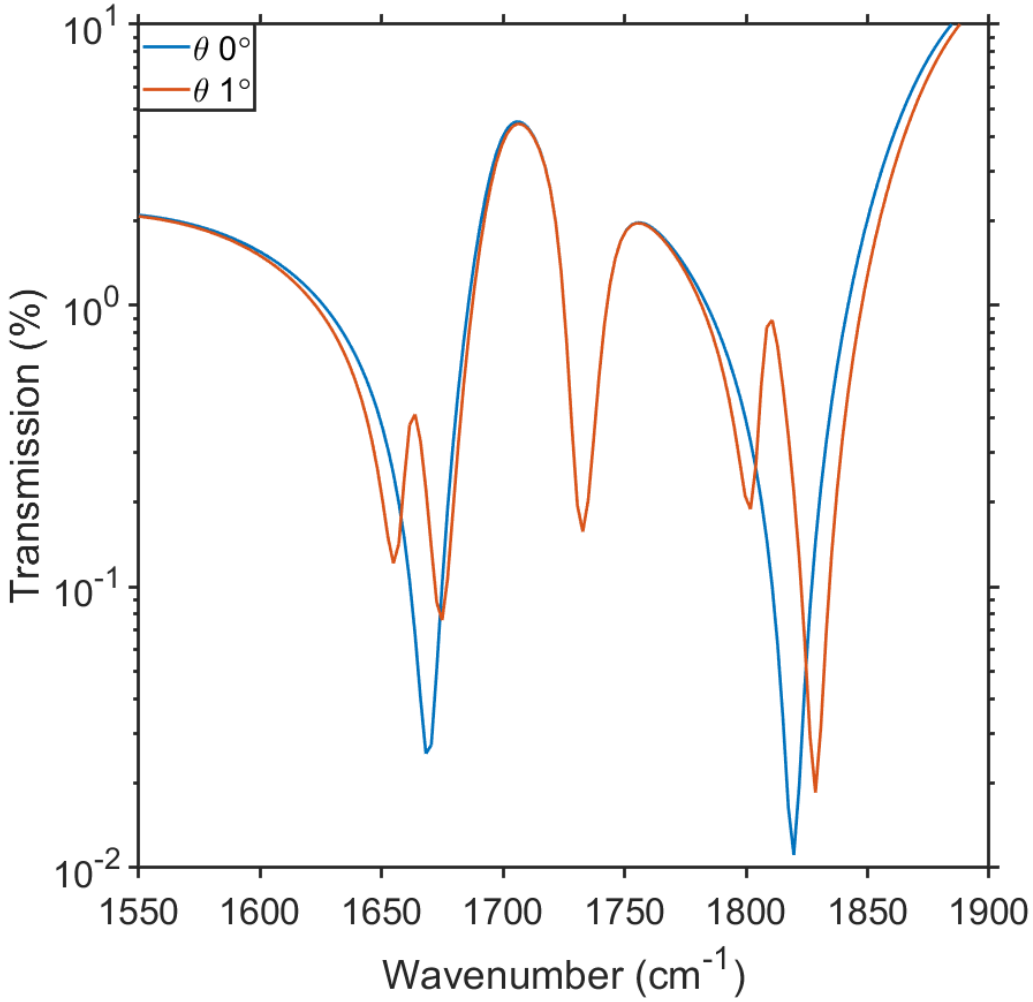

FIGURE 5.3: Coupling to band edges. Calculated transmittance for $\phi = 90°$ for two polar angles of incidence, $\theta = 0°$ (blue) and $\theta = 1°$ (red). The lower band edge at both $\sim 1670\ cm^{-1}$ and $1800\ cm^{-1}$ is only seen for off-normal incidence illumination (red). See text for details.

To be more accurate, the data in Figures 5.2 (b) and 5.3 both show that the polariton modes (rather than simply the plasmon modes) exhibit stop bands. Extending these results by introducing a grating structure in the second (y) direction would offer the prospect of introducing a polariton band gap, and would form a bridge between studies of strong coupling between molecular resonances and surface plasmons on planar surfaces, and the strong coupling

of molecular resonances with the lattice resonances associated with periodic arrays of metallic nanoparticles [22, 74–76].

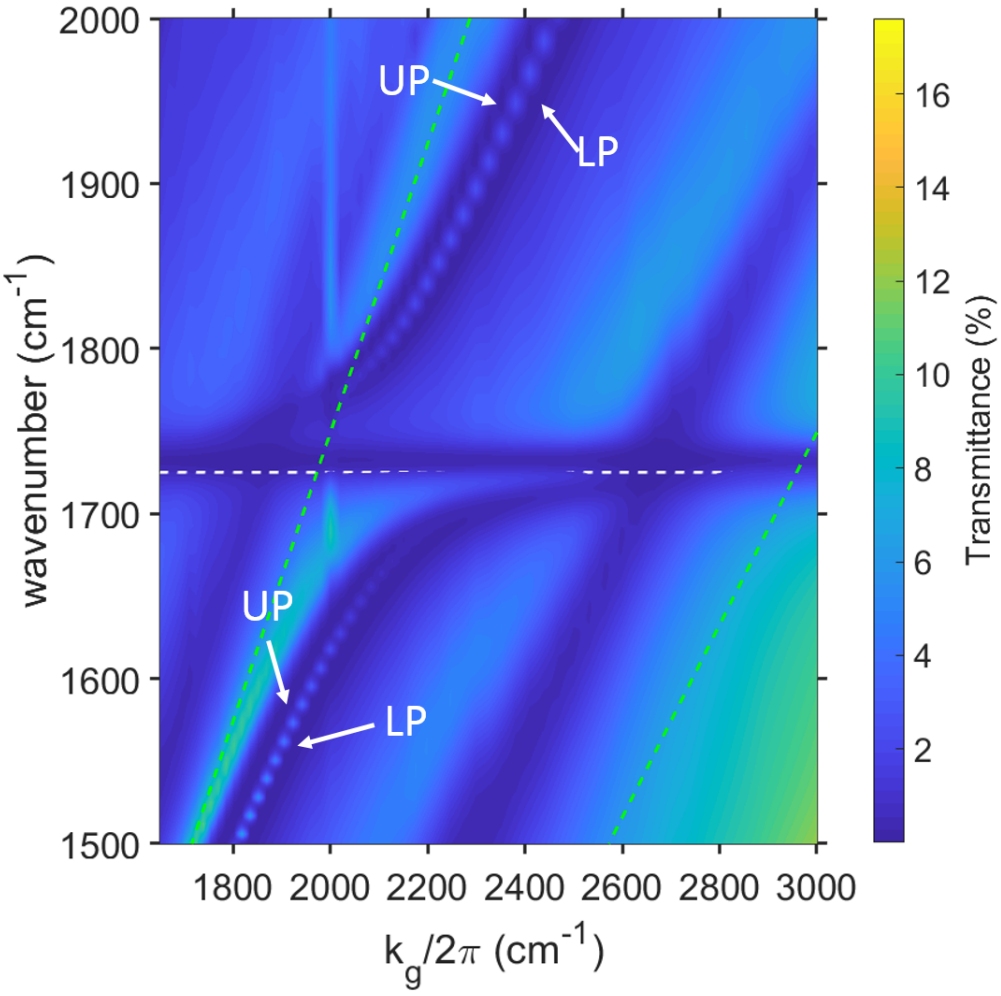

FIGURE 5.4: Effect of grating period. Calculated transmittance spectra for $\phi = 90°$ and for $\theta = 1°$ as a function of grating period. The PMMA thickness was 1.5 μm, and the gap between the metal stripes was kept constant at 1.0 μm. The green dashed lines are the second and third order grating scattered silicon light lines. The somewhat diagonal features (transmittance minima) in the data are associated with these light lines. The vertical feature at $k_g/2\pi \sim 2000 cm^{-1}$ is an artefact of the numerical calculation. upper polariton band edge and lower polariton band edge are mentioned as UP and LP respectively in the figure.

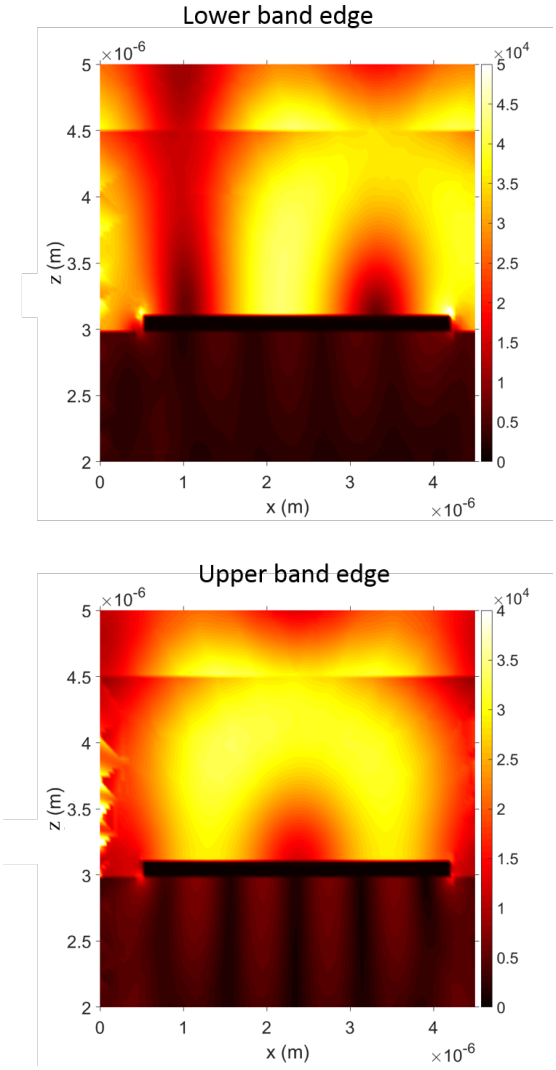

FIGURE 5.5: Electric field distributions. Calculated normalised electric field distributions for light incident at $\theta = 1°$ and $\phi = 0°$ for the lower band edge (1817 cm^{-1}) and the upper band edge (1847 cm^{-1}). The plotted values are the magnitude (norm) of the electric field, relative to the incident field (these enhancements are higher than one would expect in the visible owing to the higher Q of these IR resonances).

I also wanted to find out what happened to the two polariton stop band edges under strong coupling. To do this I again looked at the transmittance, for $\theta = 1°$ and $\phi = 90°$, and varied the period of the grating. This approach has been used successfully before in explorations of strong coupling involving lattice resonances of periodic arrays [77]. I simulated the transmittance, again

using COMSOL, varying the period, but keeping the spacing between the metallic elements fixed at 1 μm. The results of such calculations are shown in Figure 5.4. I see that both the upper and lower band edge undergo an anti-crossing. The associated field distributions, shown in Figure 5.5, show the expected symmetry [40], with the lower band edge having fields concentrated on the metal slab, whilst the upper band edge has field maxima over both metallic and gap regions. As an additional comment, I see in Figure 5.5 the reason why the low transmittance feature at the molecular resonance frequency (1732 cm^{-1}) is always present (see Figures5.2 (a) and 5.2(b)), there are regions on these samples where the field strength in minimal, so that molecules in these regions do not couple to the plasmonic modes and do not therefore undergo strong coupling, something that has been seen before for excitonic resonances [67].

5.3 Summary

In summary I have demonstrated strong coupling between molecular vibrational resonances and surface plasmons in the infrared by exploiting grating coupling. In addition to enabling light to be coupled to the hybrid vibro-plasmon polaritons, the grating nature of the surface also leads to the formation of polariton stop bands. I further showed that both upper and lower stop bands undergo strong coupling. A future study might extend my understanding by exploring the role of 2D periodic structures, e.g. to provide a full band gap. It would for example be interesting to see what would happen if such a gap was centred around the frequency of the molecular vibrational resonance, would the strong coupling be completely blocked? Finally I might add that although I have used a stripe array, a metal film with a modulated surface profile should also work [78], therefore enabling, for example, electrical access. These initial

results on strong coupling involving plasmon band edges would benefit from a more detailed investigation.

In the next chapter, I will study the interaction between a molecular vibrational mode and a coupled plasmon mode, a mode that, like the surface plasmon mode occurs outside light-line.

Chapter 6

Strong coupling beyond the light line

In this chapter, I will focus on interaction between the coupled plasmon mode and a molecular vibrational mode.

6.1 Introduction

The dispersion of microcavity modes is well-known [79, 80], and easily determined through angle-resolved measurements of, for example, reflectance and/or photoluminescence [72, 81]. However, metal-clad microcavities also support a coupled surface plasmon mode, a mode that appears to have been ignored in previous work on strong coupling in metal-clad cavities, probably because it exists beyond the light-line. The coupled plasmon mode may be understood as a hybrid mode associated with what would be two degenerate surface plasmon modes if the metallic mirror surfaces of the cavity were far apart. When the mirrors are separated by a wavelength or less the fields of these modes overlap, and the modes associated with the two surfaces couple together. One of the coupled modes is the standard lowest-order TM mode of a microcavity, which I label here the TM_0 mode, the other is the coupled plasmon mode [82] which

I label the TM_{-1} mode. This coupled plasmon mode, sometimes known as a gap mode plasmon [83, 84], or particle-on-film plasmon [71, 85, 86], or MIM plasmon (metal-insulator-metal) [87–89] is well known and indeed has been important in reaching single molecule strong coupling [90]. The key attribute of this mode in achieving single molecule strong coupling is that the mode has no lower frequency cut-off, enabling an outstanding degree of field confinement to be achieved.

Here I look at a less extreme cavity situation than that used for the single molecule strong coupling mentioned above. I show that the coupled plasmon mode, though so far not seen in typical strong coupling experiments, is nonetheless present, and that it too is strongly coupled to the molecular resonance. Since such modes are beyond the light-line I need to provide some kind of momentum matching, here I do this by introducing a grating structure into the cavity, allowing the coupled plasmon mode to be coupled to incident light – and thus probed – by grating scattering [73]. Furthermore, I show that beyond-the-light-line modes also exist for DBR-based (distributed Bragg reflector) cavities. My results thus highlight the fact that the majority of microcavities used in strong coupling experiments ignore strongly coupled modes that lie beyond the light-line, and that more work is needed to better understand the contribution strong coupling to such modes may make to modified material/chemical properties.

6.2 Strong coupling with coupled plasmon mode

In this chapter I make use of strong coupling between the molecular vibrational resonance of the C=O bond in the polymethylmethacrylate (PMMA) polymer, at 1732 cm^{-1}, and the resonant infrared modes of suitable metallic

micro-structures. Strong coupling involving vibrational resonances [5, 23–31, 44, 61] has been less intensively studied than that of excitonic resonances; however, vibrational resonances have allowed strong coupling to be observed in liquids [32], and in transition metal complexes [31], as well as in liquid crystals [33]. In addition, strong coupling of vibrational resonances has been reported to catalyze and inhibit chemical reactions [34], and to allow the control of the nonlinear infrared properties [35]. For the present work vibrational resonances offer the benefit of narrow linewidth transitions and the advantage of involving longer wavelengths, thus simplifying some of the fabrication tolerances required.

In figure 6.1, I summarize the structures and modes that form the basis of the investigation reported here. The top row shows schematics of the structures considered, the lower row shows numerically calculated dispersion plots to indicate the modes supported by the different structures. I look at two types of confined light field, those associated with the surface plasmon mode of a single metallic interface, figure 6.1a, and those associated with a planar metal microcavity, figure 6.1c & e. For the microcavity I consider two different cavity thicknesses, one that places the usual cavity cut-off at the same frequency as the molecular resonance, figure 6.1c, the other (thinner) only supports the usual lowest order cavity mode for frequencies much higher than the molecular resonance.

The surface plasmon (SP) mode is considered in the left-hand column. The structure I consider consists of a CaF_2 substrate coated with a 30 nm thick planar layer of gold, the structure is completed by adding a 1μm thick film of the polymer PMMA, figure 1a. The dispersion of the modes supported by this structure is shown in figure 1b. Here a Fresnel coefficient formalism [91] was used to calculate the absolute value of the p-polarized amplitude transmission

coefficient, $|t_p|$, which I have plotted as a function of frequency and in-plane wavevector. (The in-plane wavevector, k_x, is the wavevector component in the plane of the structure.) For these calculations the PMMA molecular resonance at 1732 cm^{-1} was represented by a single Lorentzian oscillator, details of this model, together with other parameters used, details are given in the chapter 3. The data in figure 6.1b show the surface plasmon mode, indicated by the bright region. This mode lies, as expected, just beyond thew air light-line (indicated as a blue dashed line). Importantly, a clear anti-crossing of this mode is seen where the mode's frequency matches the frequency of the C=O molecular resonance. This anti-crossing is the result of strong coupling between the surface plasmon mode and the C=O resonance. Although the surface plasmon mode is beyond the light-line, it is not the main focus of the investigation reported here, however, I have begun by examining this mode so as to provide a familiar starting point; indeed, strong coupling between vibrational molecular resonances and surface plasmon modes has been observed before [28, 92, 93].

The structure of the metal-clad microcavity is shown in figure 6.1c, a cavity has been formed by adding an upper layer (30 nm) of gold to the structure used for the surface plasmon investigation, figure 6.1a. For this central column of figure 6.1 the cavity thickness was been chosen to be 2 μm, so as to place the usual fundamental cavity mode resonance close to the molecular resonance of the C=O bond at 1732 cm^{-1}. The dispersion of the modes supported by this structure are shown in figure 6.1d, where, as for figure 6.1b, the absolute value of the p-polarized amplitude has been plotted as a function of frequency and in-plane wavevector. Two modes are seen in these data, and both show an anti-crossing with the molecular resonance. Let us first concentrate on the fundamental cavity mode (TM_0), seen for lower values of the in-plane wavevector, i.e. inside the light-line. The anti-crossing seen here is again

a result of strong coupling between the fundamental cavity mode and the molecular resonance. This combination has been the workhorse of many strong coupling experiments [5, 23], yielding a very clear splitting that produces upper and lower hybrid polariton modes. These hybrid polariton modes lie inside the air light-line (the blue dashed line in figure 6.1d). The second mode lies beyond the air light-line, and importantly does not have a cut-off, i.e. it has now lower frequency limit. This second mode looks similar to the surface plasmon mode seen in figure 1b, this is perhaps not so surprising since this mode is the coupled plasmon mode (TM_{-1}).

The coupled plasmon mode also shows clear evidence of strong coupling, a fuller analysis, including an evaluation of the appropriate Hopfield coefficients, will be discussed below. In previous work on strong coupling employing metal-clad microcavities this mode was not been seen because it lies beyond the light-line. In the remainder of this chapter I will show how grating coupling can be used to gain access to this mode, in this way I am able to show that it *is* strongly coupled, and thus led to consider what role it might play in the way molecules within the cavity behave.

In addition to the usual cavity mode of metal-clad cavities, strong coupling also arises due to the coupled plasmon modes present in such structures. My results indicate that this mode should be taken into account when looking at how strong coupling may be used to alter/create molecular properties via strong coupling.

Before moving to the experimental section I want to consider what happens when I reduce the cavity thickness so that the usual fundamental mode is shifted well above the molecular resonance in frequency. The dispersion of modes present in such a cavity are shown in figure 6.1f. The structure I consider, shown in figure 6.1e, is the same as for figure 6.1c & d except that the thickness

of the PMMA has been halved, from 2 μm down to 1 μm. Although the fundamental cavity mode (TM_0) is no longer seen, the coupled plasmon mode is still present, lying at higher in-plane wavevector values than for the thicker cavity, figure 6.1d, a direct result of the greater degree of field confinement in this thinner cavity. Importantly, a clear anti-crossing signature is seen, again the result of strong coupling. This result will be discussed in more detail below.

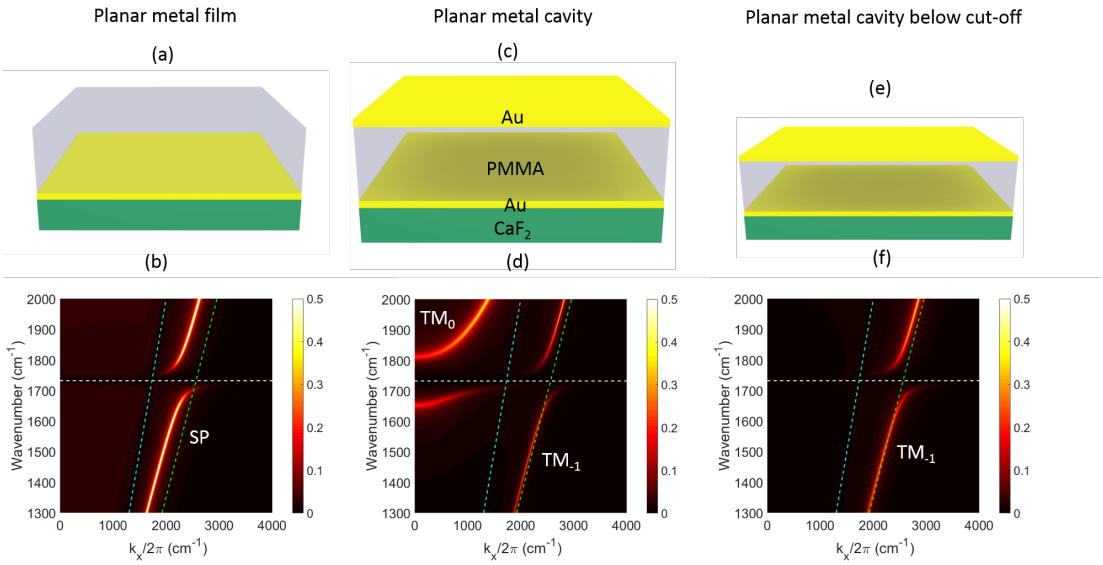

FIGURE 6.1: **Structures and modes investigated**. Top row, schematics of the different structures considered: (a) A single planar gold metal film (30 nm) overlain with a 2 μm polymer PMMA film, supported on a CaF_2 substrate, this structure is used to investigate the surface plasmon mode; (c) Standard microcavity - a 2 μm thick film of PMMA is sandwiched between two 30 nm thick planar gold mirrors, the substrate is CaF_2; (e) A microcavity below the usual cut-off. This structure is the same as for (c) except that here the PMMA thickness is 2 μm, again, the substrate is CaF_2. Bottom row, numerically calculated dispersion plots for the structures shown in the top row. Calculations were based on Fresnel coefficients, and the absolute value of the complex p-polarised amplitude transmission coefficient is shown as a function of frequency (wavenumber) and in-plane wavevector. The modes in the lower row are indicated: SP, surface plasmon; TM_0, standard cavity mode; TM_{-1}, coupled plasmon mode. The horizontal whites dashed line in each dispersion plot indicates the position of the molecular resonance. Also shown in each dispersion plot (bottom row) are two light lines. These are the: air light-line, blue-dashed; and polymer light-line (assuming the C=O resonance is absent), green-dashed. Note that to calculate the dispersion data shown here I set the refractive index of the superstrate and the substrate to be $n = 10$, I did this to avoid the date showing surface plasmon modes associate with the metal/air and metal/substrate interfaces. Further calculations (not shown) indicate that making this choice ($n = 10$) does not significantly alter the dispersion of the modes I are interested in.

Now that I have established the structures and modes for study, figure 6.1, I next consider their experimental investigation. To access modes beyond the

air light-line I make use of grating coupling. I do this making (one of) the gold film(s) in the form of a 1D stripe array, see figure 6.2b & e. Figure 6.2 provides the key information associated with using gratings to couple to the modes I wish to investigate. The central column, figure 6.2b & e, shows the structures I consider: figure 6.2b is a 1D gold stripe array that allows us to explore the surface plasmon mode; figure 6.2e is a metal-clad microcavity where the lower mirror is in the form of a 1D strip array to allow me to explore the cavity coupled plasmon mode. In the left-hand column I show indicative dispersion plots for the two structures. Here I have simply made use of the Fresnel-based data shown in figure 6.1b & f, except that now I have plotted two copies of the data, one shifted by an in-plane wavevector that matches the grating wavevector, $-k_g/2\pi = 2127$ cm^{-1}, the other reversed in wavevector and also shifted, this time by $+k_g$; these two sets thus represent the effect I expect the grating scattering to have on the transmission of incident light. My choice of grating wavevector (grating period = 4.7 μm) was made so as to place the anti-crossing region of the modes I am interested in close to zero in-plane wavevector (normal incidence). In the right-hand column I show a combination of numerically simulated and experimental data. For both plots in the right-hand column, figure 6.2c & f, the left-hand half shows data calculated using COMSOL whilst the right-hand half shows experimental data. For the experimental data I measured the infrared transmission or samples using Fourier transform infrared spectroscopy (Details are in chapter 3). By measuring transmittance spectra as a function of angle of incidence (in the $x-z$ plane, see figure6.2) a dispersion plot can be constructed [5, 23, 94], such plots are shown in figure 6.2c & f.

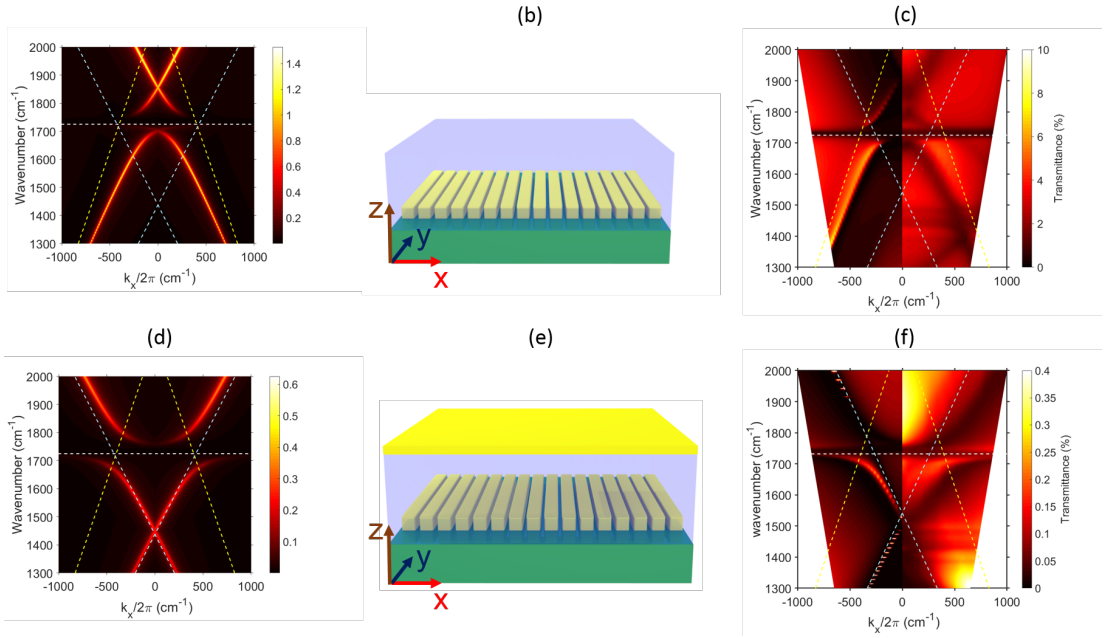

FIGURE 6.2: **Modes supported by structures incorporating gratings.** Top row, surface plasmon (SP) mode. Bottom row, 'below cut-off' microcavity (TM_{-1}) mode (the coupled plasmon mode). Central column, grating structures; shown here are schematics of: upper, 1D metal grating supporting a surface plasmon mode, on top of a CaF_2 substrate, overlain by a 1 μm layer of PMMA; lower, a microcavity incorporating a 1D metal grating as the lower mirror, the cavity is filled by a 1 μm layer of PMMA. The gold films for both structures were 30 nm thick. Left-hand column, calculated grating-scattered dispersion plots. These data were produced by taking the data in figure 1b & f and applying both $+k_g$ and $+k_g$ grating scattering, so as to produce figures 1a & d respectively; details are given in the text. The grating period was taken as 4.7 μm, for which $k_x/2\pi = 1/\lambda_g = 2127\ cm^{-1}$. The $\pm k_g$ scattered air and PMMA light-lines are shown as yellow and light-blue dashed lines respectively. Right-hand column, these dispersion plots are divided into two halves. In the left half, data calculated using COMSOL are shown, in the right half, experimentally measured data are shown. The maximum polar angle for these data is 18°. Details of the grating profile are provided in the Supp Info. As for the calculated dispersion plots, here the $\pm k_g$ scattered air and PMMA light-lines are shown as yellow and light-blue dashed lines respectively.

For both the surface plasmon mode, figure 6.2c, and the coupled plasmon mode associated with the cavity below cut-off, figure 6.2f, I see anti-crossings that agree well with what I expect from my indicative Fresnel-based modelling

(figure 6.2a & d) and my more thorough numerical calculations (figure 6.2c & f).

Having established that strong coupling may occur between molecular resonances and modes beyond the light-line I can begin to look at the implications this may have. One way to explore this is to make use of a coupled oscillators model to look at the contribution the different cavity modes and the molecular resonance make to the polaritons. This is a well known approach, I now adopt this approach to look at a cavity close to the usual cut-off, i.e. the situation shown in figure 6.1c & d. I chose this particular situation since a cavity close to cut-off is the commonly used system, I can thus use it to see how the presence of the TM_{-1} mode beyond the light-line modifies thus commonly adopted picture. As a first step I represent dispersion of the TM_0 and TM_{-1} modes analytically,

6.2.1 Coupled oscillators model

The coupled oscillators model can be represented through the following matrix equation,

$$\begin{pmatrix} E_{\mathrm{TM}_0}(k_x) & 0 & \Omega_1/2 \\ 0 & E_{\mathrm{TM}_{-1}}(k_x) & \Omega_2/2 \\ \Omega_1/2 & \Omega_2/2 & E_{\mathrm{C}=0} \end{pmatrix} \begin{pmatrix} a_{L,M,U} \\ b_{L,M,U} \\ c_{L,M,U} \end{pmatrix} = E_{L,M,U} \begin{pmatrix} a_{L,M,U} \\ b_{L,M,U} \\ c_{L,M,U} \end{pmatrix}. \qquad (6.1)$$

In this equation: $E_{\mathrm{TM}_0}(k_x)$ is the energy of the cavity (TM_0) mode, $E_{\mathrm{TM}_{-1}}(k_x$ is the energy of the coupled plasmon (TM_{-1}) mode, and $E_{\mathrm{C}=0}$ is the energy of the vibrational resonance; $E_{L,M,U}$ are the eigenvalues of the characteristic matrix (left) and are the energies of the three hybrid polaritons, indicated by the subscripts - L for the lower polariton, M for the middle polariton and U for the upper polariton; a, b and c are the (Hopfield) coefficients of the eigenvectors,

they are subject to the condition $|a|^2 + |b|^2 + |c|^2 = 1$, the individual coefficients giving the contribution of the TM_0 mode, the TM_{-1} mode and the vibrational resonance to the three polaritons, L, M, and U. Finally Ω_1 and Ω_2 are the coupling strengths (Rabi-splittings) for the interaction between the TM_0 and the TM_{-1} with the molecular resonance.

The results from solving for the eigenvalues and coefficients of equation 6.1 are shown in figure 6.3. The top row of figure 6.3 is the result of a two coupled oscillators model, one that includes only the cavity (TM_0) mode and the molecular resonance; this provides a useful reference for the three oscillator model involving the (TM_0), the (TM_{-1}) and the molecular resonance in the lower row. For the three oscillator model (lower row), a reasonable match with the experimental data was obtained for Rabi-splittings of $\Omega_1 = \Omega_2 = 150$ cm^{-1}: I made use of the same splitting in the two oscillator model (upper row). These splittings compare with mode widths of cavity mode 60 cm^{-1} and coupled oscillator 75 cm^{-1}. In the left-column of figure 6.3 I present the dispersion of the modes in the two (upper) and three (lower) coupled oscillator systems. Also shown as dashed lines are the dispersion of the uncoupled modes.

The data shown in figure 6.3 allow me to make an initial assessment of the role played by the coupled plasmon mode in strong coupling in a typical microcavity. Looking first at the standard two oscillator model (top right), I see the expected contribution of the molecular resonance to the upper polariton and the lower polariton. There molecular resonance is equally split between the two polaritons at the wavevector corresponding to the crossing point. As the wavevector increases the lower polariton becomes resonance-like, the upper polariton photon-like. If I now look at the three oscillator model–where the influence of the coupled plasmon mode is included–then a rather different picture emerges. There are now three polariton modes, an upper, middle and

lower polariton. In the lower right panel the extent to which the molecular resonance contributes to these three polaritons is shown. At low wavevectors the situation looks very similar to that of the two oscillator system (upper right), however, as the wavevector rises the molecular contribution shifts to the new lower polariton. What consequences might this have? Two possibilities can be readily identified.

First, in considering disordered cavity materials (rather than crystalline)–as is usually the case in experiments, and is certainly the case here for the polymer PMMA– the range of wavevectors over which the lower polariton branch of the two oscillator model makes physical sense is limited, as pointed out by Agarnovich and Lidzey [80]. However, their upper limit on wavevector far exceeds the range over which the cavity (TM_0) mode is the only significant mode. I might therefore expect that, for example, relaxation from initially uncoupled states into the lower polariton will be modified by the presence of the TM_{-1} mode. Second, I need to think about the spatial location of the molecules involved in the different polaritons.This is because the two modes, the cavity (TM_0) mode, and the coupled plasmon (TM_{-1}) mode, have rather different field profiles.

In figure 6.4 I show the field distribution associated with the two modes. On the left, the time-averaged electric field components associated with the TM_0 mode are shown, on the right those for the TM_{-1}. The net electric field near the cavity mirrors is significantly greater for the TM_{-1} mode - molecules near the mirrors will preferentially couple to this mode. It thus looks as though the dynamics of some phenomena associated with strong coupling and the way different molecules couple with different modes both act to make strong coupling in these candidate systems more complex and richer than previously thought. These initial observations needs following up with a more detailed

study.

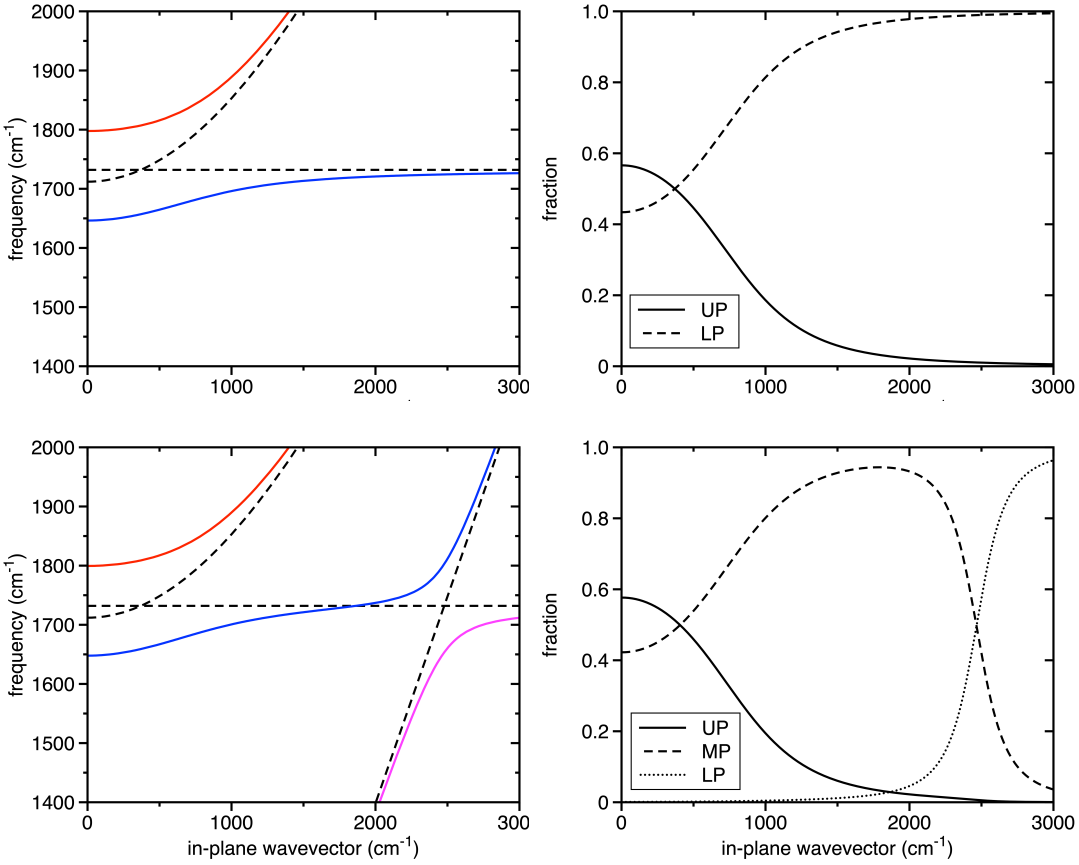

FIGURE 6.3: **Coupled oscillators model.** Left column: calculated dispersion of the polariton bands Top row, upper plot for a cavity mode and the molecular resonance, lower for a cavity mode, a coupled plasmon mode, and a molecular resonance. Right column: Hopfield coefficients for the fraction of molecular resonance in the different polaritons shown in the dispersion plots (left). Figure courtesy of William L. Barnes

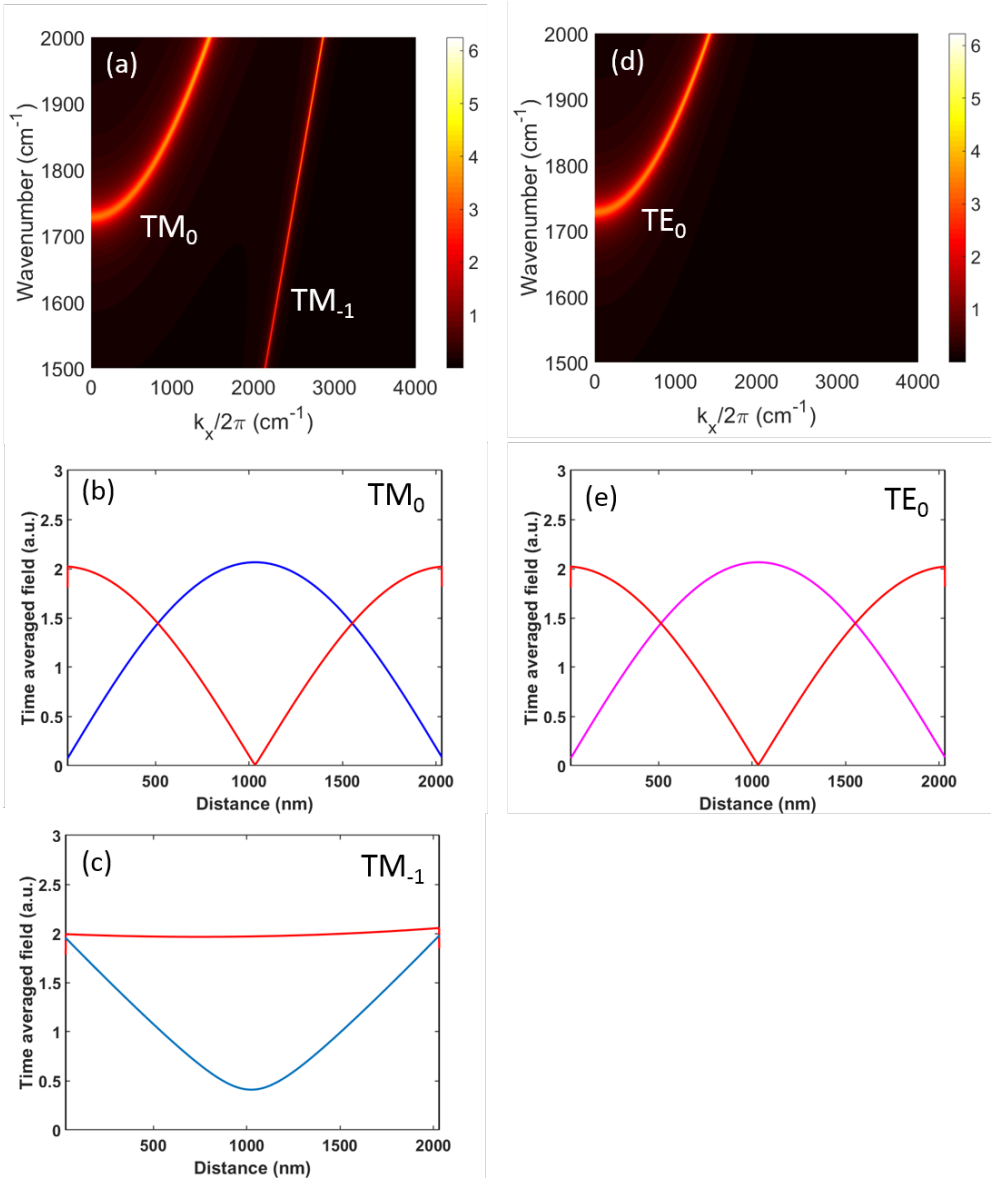

FIGURE 6.4: **Field profiles.** Top row: the absolute value of the complex TM-polarised and TE-polarised amplitude transmission coefficients in the absence of the molecular resonance (vibrational mode) is shown in (a) and (d) respectively, as a function of frequency (wavenumber) and in-plane wavevector. The remaining plots show the time averaged electric fields. (b) and (d) are for the TM_0, (c) TM_{-1} modes, with E_x and E_z in blue and red respectively. (e) is for the TE_0 mode, here with E_y and E_z in magenta and red respectively. The field profiles were calculated at a frequency of 1732 cm^{-1}, and for the following in-plane wavevector values: TM_0 and TE_0 mode at $\sim$ 138 cm^{-1}, TM_{-1} mode at $\sim$ 2450 cm^{-1}.

In Figure 6.3 the calculated dispersion plot of the polariton bands in the

cavity system is shown in top left and in the coupled plasmon system is shown in bottom left. Hopfield coefficients of molecular resonance in the cavity and in the coupled plasmon mode is shown in top right and bottom right respectively. The contribution of the Hopfield coefficient is around $\sim$ 50% for cavity system. The similar contribution is also observed for the coupled plasmon system.

6.2.2 Change in PMMA thickness

In figure 6.5 as I are increasing the thickness of the PMMA layer, the coupled plasmon mode drifts away from air light line. The blue dotted line represents the air-light line. The important characteristic of the coupled plasmon mode for the present work is that it has no lower frequency cut-off, enabling an outstanding degree of field confinement to be achieved. Indeed, this combination of field confinement and no cut-off has been exploited recently to achieve single molecule strong coupling, by placing a molecule in the gap–only a few nm thick–between a planar metal film and an overlying metal particle [90].

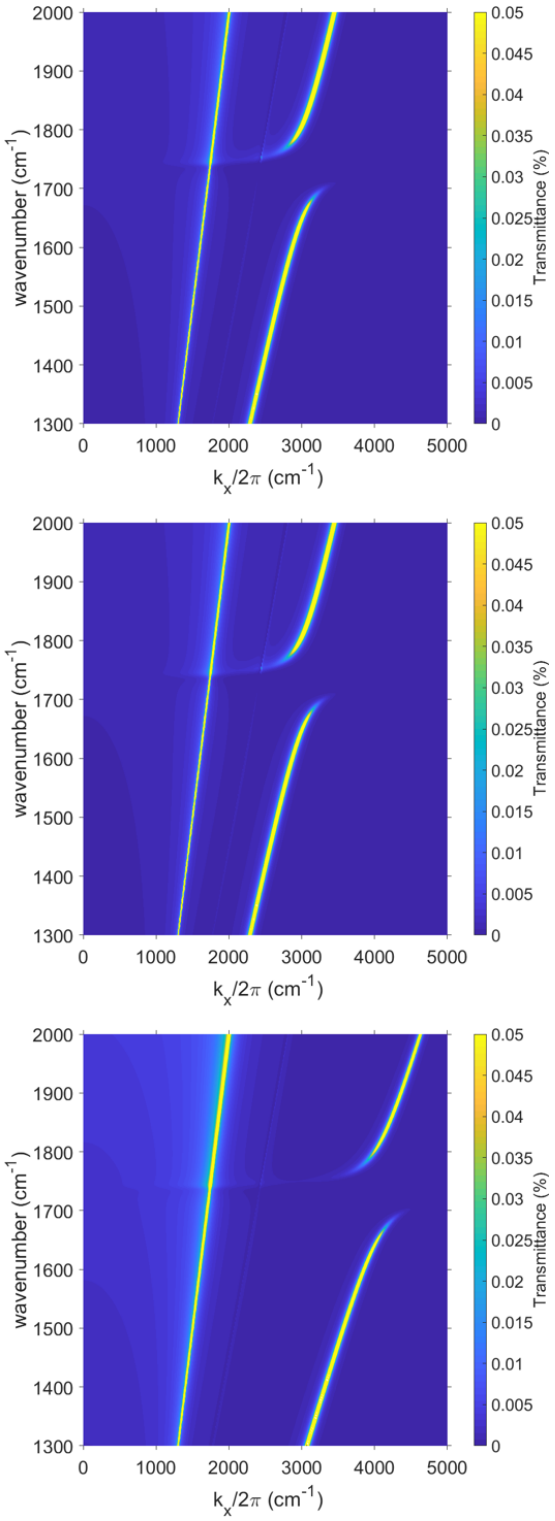

FIGURE 6.5: Dispersion plot showing changing pmma thickness to 1 μm , 100 nm and 30 nm respectively. The Top and the bottom mirrors were kept constant with 30 nm thickness each. As the thickness is increased, the coupled plasmon mode shifts away from light line

6.2.3 Field profiles

In figure 6.4 (panels b & c) we show the calculated field distributions associated with these two modes. For completeness we also show the field distribution for the TE polarised lowest order cavity mode, TE_0 (panel e). Note that there are subtle differences between the dispersion of the TE_0 and TM_0 modes [95], and in addition when the dipole moment associated with a molecular resonance is oriented in the plane of the cavity, the polarisation of the modes that the molecules may couple to also becomes important [96]. The data in figure 6.4 indicate that the net electric field near the cavity mirrors is significantly greater for the TM_{-1} mode, so that molecules near the mirrors will preferentially couple to this mode. It thus looks as though the dynamics of some phenomena associated with strong coupling and the way different molecules couple with different modes both act to make strong coupling in these candidate systems more complex and richer than previously thought.

6.2.4 DBR based cavity

At this point it is also worth looking at cavities made with distributed Bragg reflecting (DBR) mirrors, rather than metallic mirrors, with the aim of investigating whether there are modes in such cavities that also lie beyond the light line, and if so whether they undergo strong coupling. Muallem, *et al*. [97] presented results on strong coupling between molecular vibrational resonances in PMMA and the cavity mode of a DBR-based cavity. They showed that strong coupling to the standard cavity mode occurs using these cavities, much as it does for the usual metal-based cavities. However, their investigation did not go beyond the light-line. Here we extend this investigation to regions beyond the air light-line. Figure 6.6(a) shows a schematic of the structure we consider, employing ZnS and Ge DBR mirrors (see methods for further details). In figure 6.6(b) we show

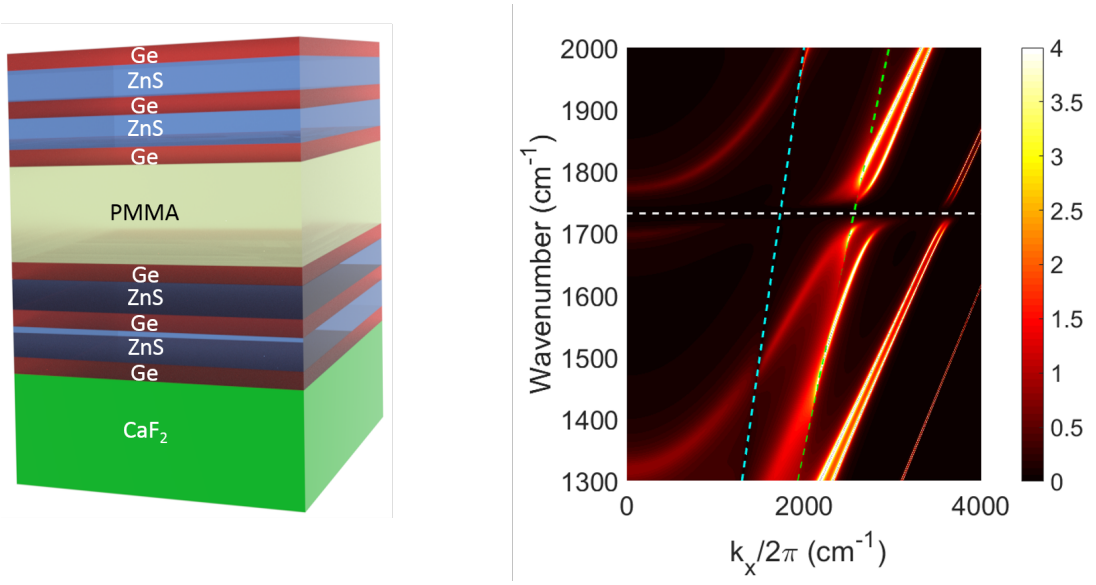

FIGURE 6.6: **DBR-based cavity** (a) Schematic showing DBR cavity structure. (b) Dispersion plot based on Fresnel-type calculations. The absolute value of the TM polarised Fresnel coefficient is shown as a function of frequency (wavenumber) and in-plane wavevector. The blue and green dashed lines represent the air and PMMA light lines respectively. The molecular resonance is shown as a horizontal dashed white line. Layer thicknesses and material parameters for the DBR mirrors are given in the methods section.

a dispersion plot for this structure, calculated using the Fresnel-based approach we used for figures 6.1 and 6.4. As for the metal-clad cavities discussed above, in addition to strong coupling of the standard cavity mode we see that there is also strong coupling between the molecular resonance and the mirror modes of the DBR that lie well beyond the light line.

6.3 Summary

In Summary, the results show that in addition to the usual cavity mode of metal-clad cavities, strong coupling also arises due to the coupled plasmon modes present in such structures. My results indicate that this mode should be taken into account when looking at how strong coupling may be used to alter/create molecular properties via strong coupling.

The next chapter will focus on areas for future work, in which I present some initial results on each topic discussed. I will primarily discuss vibrational strong coupling involving photochromic molecules, increasing the extent of strong coupling, and a three cavity system.

Chapter 7

Future work

A number of ideas and projects emerged during the work on this thesis for which there was insufficient time to complete. Some of these ideas for future work are discussed here. In this chapter, I will briefly mention these ideas and, where possible, present some preliminary results.

7.1 Vibrational strong coupling involving photochromic molecules

Schwartz, T. *et al.* [13] looked at strong coupling in the visible for an interesting system in which the molecules within the cavity were photochromic. They used spiropyran molecules. These molecules, when place in a cavity, showed only weak coupling. However, when the cavity was illuminated with UV light the molecules were transformed from spiropyran to merocyanine . Merocyanine has a strong absorption in the visible, and in this form the cavities showed strong coupling. Importantly, this conversion under UV illumination was reversible - a photochromic process. The Rabi splitting of cavities exhibiting the merocyanine form was around 700 meV. I wanted to see whether there were

differences in the vibrational spectra of the spiropyran/merocyanine forms, and if there were, whether one of them might show strong coupling.

Figure 7.1 shows an infrared spectrum of spiropyran vibrational modes for different UV illumination times. The data show that after shinning UV light, the intensity of certain vibrational modes change. For example, the mode at around 1340 cm^{-1} goes from being a sharp and strong signal to being a weak signal. For the first set of experiments, only 6 minutes of total UV illumination was used, at one minute intervals.

The main idea of the experiment was to put the spiropyran inside the microcavity and monitor the vibrational modes as UV light was applied. As we know from figure 7.1 that UV light changes the intensity of the modes, so we should be able to control the coupling strength to a microcavity mode via UV illumination.

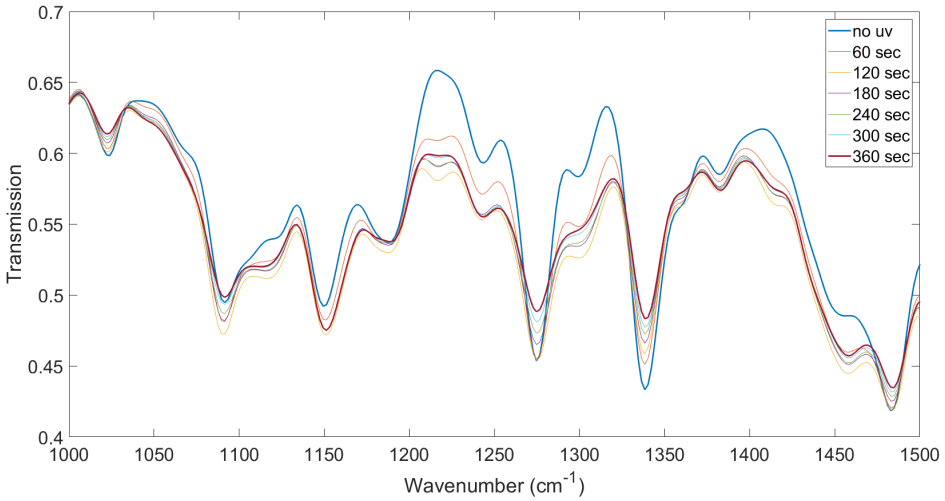

FIGURE 7.1: FTIR transmission spectra of spiropyran taken at different time duration. Initially the first spectrum was taken when no UV light was shone on to the sample. As I started shining UV light, the intensity of few of the vibrational mode started to get shrunk i.e 1340 cm^{-1} and 1275 cm^{-1}

The schematic of the system is shown in figure 7.2 (a) The spectra in orange

in figure 7.2 (b) is the reference transmission spectra of spiropyran on top of silicon substrate. The spectra in blue shows the FTIR transmission of the spiropyran-filled cavity sample. The addition peak around 1275 cm^{-1} may be because of strong coupling between vibrational mode of spiropyran molecule and the cavity mode. Future research might be based on pursuing these results further and looking at what UV illumination conditions are required to achieve strong coupling.

To understand the system better, further study is required.

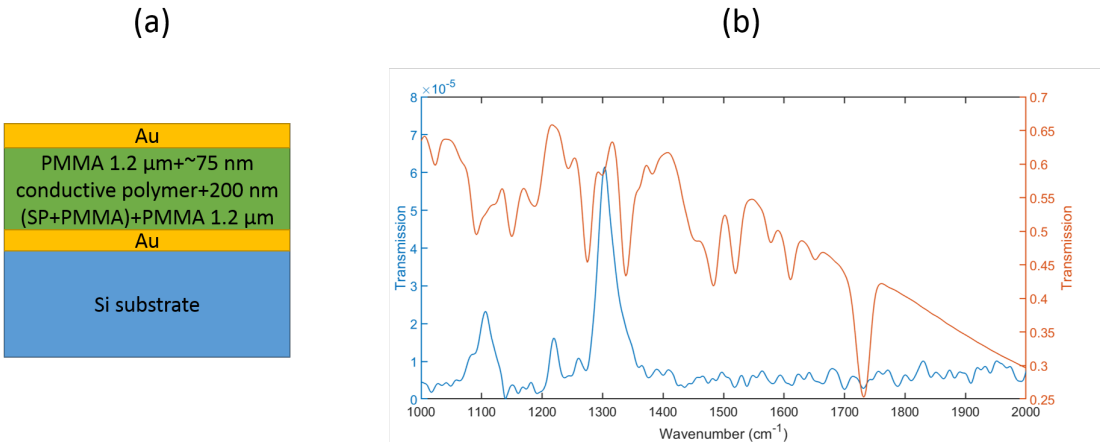

FIGURE 7.2: (a) Schematics of an optical micro-cavity formed of two gold mirrors separated by mixture of spiropyran and pmma. (b) FTIR transmission spectra of spiropyran film is in orange and transmission spectra of spiropyran inside the cavity at zero angle is in blue.

7.2 Increasing the extent of strong coupling

As discussed in the Chapter 4, the coupling strength between confined light and molecule can be increased by adding different molecule vibrational species. This section is further divided into two parts. 1) Increasing the extent of strong coupling in microcavity structure. 2) Increasing the extent of strong coupling in coupled plasmonic structure. I will first begin with microcavity structure.

7.2.1 Increasing the extent of strong coupling in micro-cavity structure

Instead of using PMMA for vibrational mode study, I added PMGI in between two PMMA layers and spun them on top on silicon substrate. Figure 7.3 (b) shows FTIR transmission spectrum of vibrational modes of PMMA and PMGI in solid black line. The numerical calculated transmission spectra is shown in blue dotted line.

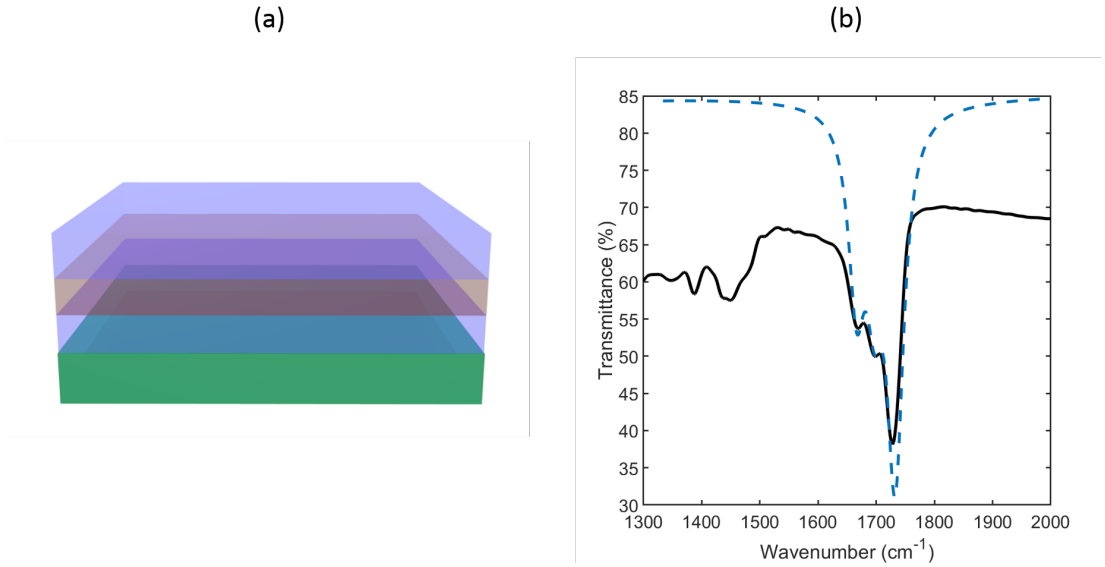

FIGURE 7.3: (a) Schematics of sample geometry. 400 nm of PMGI is sandwiched between two 600 nm PMMA layers. (b) experimental transmission spectra is shown in black solid line and numerically calculated transmission spectra in blue dashed line.

Vibrational modes of PMGI are visible around 1750 cm^{-1} close to C=O vibrational mode of PMMA at 1732 cm^{-1}. The idea is to show that adding more than one vibrational mode of different species at approx. the same frequency will help to increase the vacuum Rabi splitting of the overall system.

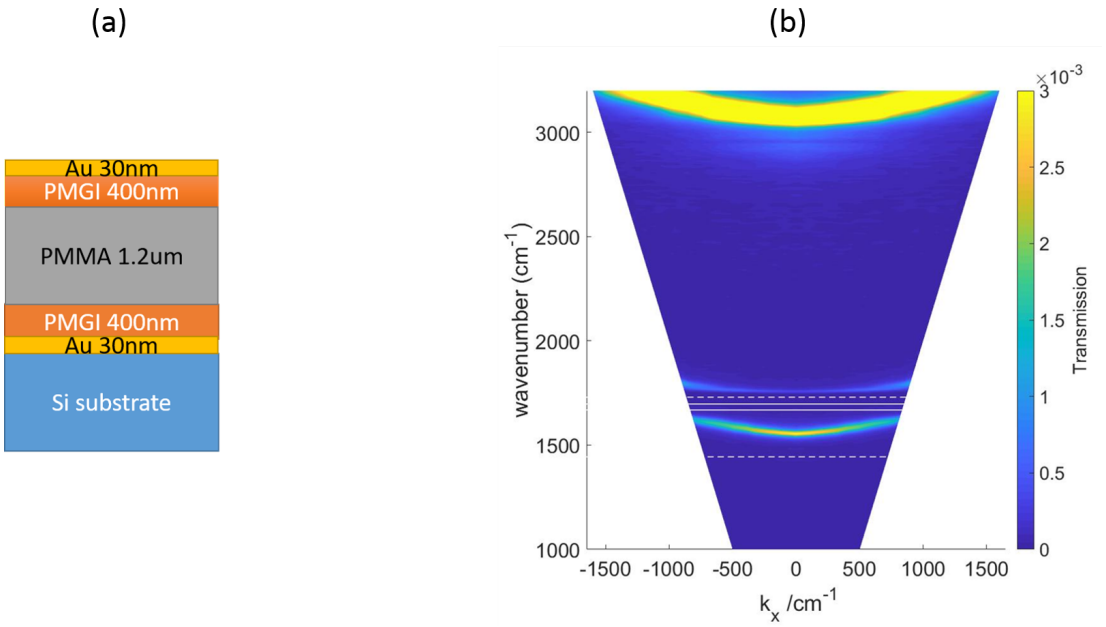

FIGURE 7.4: (a) Schematics of (b) experimentally calculated dispersion spectra of figure 7.4 (a). The white dashed line is C=O vibrational mode of PMMA and the two solid white lines are vibrational modes associated with PMGI

Figure 7.4 (a) shows the schematics of an optical micro-cavity consisting of two gold mirrors and the mixture of PMGI and PMMA sandwiched between them. Using FTIR the dispersion plot of the system, 7.4(a), was acquired and is shown in figure 7.4 (b). The solid white dashed lines are vibrational modes present in PMGI and the dotted white lines show the presence of the PMMA vibrational mode.

An increase in the Rabi splitting by almost 33 % is observed compared to what I observed in chapter 4. Specifically, the Rabi splitting comes around 210 cm^{-1} compared to Rabi splitting around 150 cm^{-1} for just the PMMA.

7.2.2 Increasing the extent of strong coupling in coupled plasmonic structure

Similar to strong coupling of C=O vibrational mode with coupled plasmonic mode discussed in chapter 6, now I will introduce vibrational modes of different species into the system i.e. PMGI.

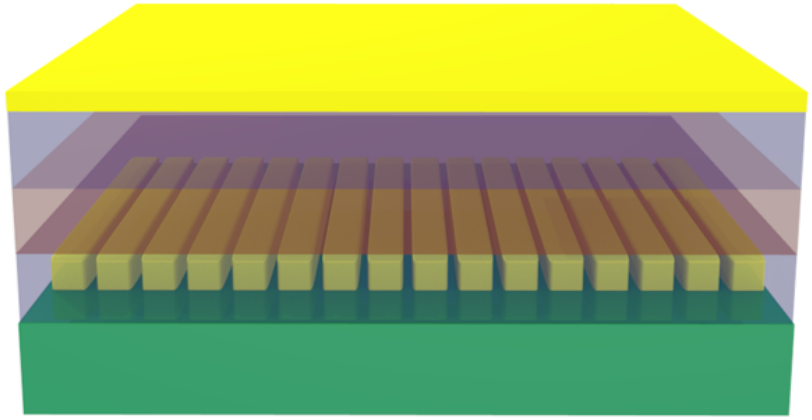

FIGURE 7.5: Schematics of coupled oscillator filled with mixture of PMMA and PMGI.

The schematic of the system is shown in figure 7.5. The 200 nm of PMGI is sandwiched between two 300 nm pmma layers on one dimensional gold grating structure. The pitch is 4.7 μm and the gap is 1 μm. The thickness of bottom as well as the top deposited gold films is 30 nm.

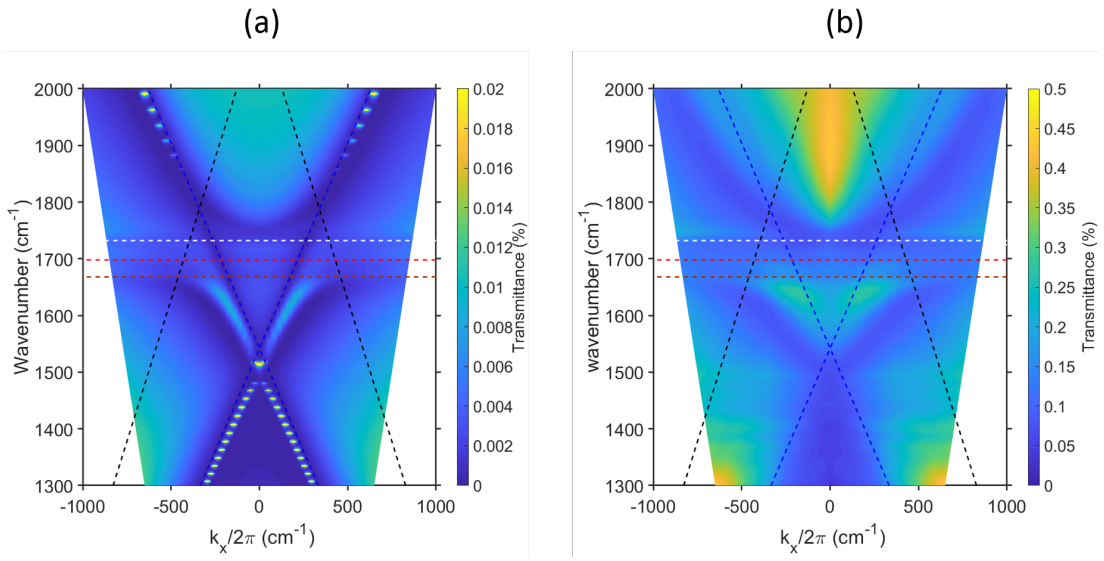

FIGURE 7.6: (a) Numerically calculated transmittance data of coupled plasmon system with mixture of PMGI and PMMA in-between two gold metal layer (b) experimentally measured data of the same system

Figure 7.6 shows the comparison between the numerically and experimentally calculated dispersion plots of figure 7.5 system. Similar to the previous microcavity section, an increase in the Rabi splitting by almost 33 % is observed compare to what I observed in chapter 6. Here, the Rabi splitting also comes to around 210 cm^{-1} compare to 150 cm^{-1} with just the PMMA.

7.3 Strong coupling and Raman spectroscopy

Later in this thesis a modulated Raman technique is discussed, it is used to obtain a better signal to noise ratio specially in the presence of fluorescence. Tunable sacher laser is of 1 W. The laser wavelength is 785 nm and the numerical aperture (NA) is 1.4 oil objective lens. Modulated Raman works through a periodic modulation of the laser excitation wavelength. It has many important features such as multi-channel lock in detection but the most important feature is the stationary fluorescence, and is widely used for medical applications [98,

99]. Strong coupling of molecular vibrations and a micro-cavity mode has been demonstrated using FTIR in chapter 4. Recently, Shalabney et al. [100] reported that the same large Rabi splitting could be seen in Raman scattering measurements of the micro-cavity system .

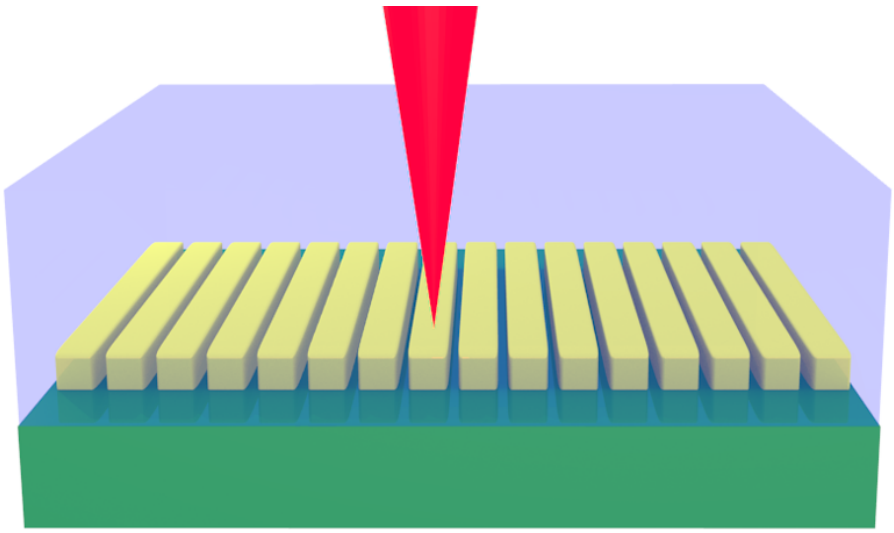

FIGURE 7.7: Schematic of Raman laser on one dimensional gold grating structure

Pushing that idea to further, I looked at a one-dimensional gold grating structure on silicon substrate rather than a microcavity. The idea was to see whether strong coupling between a surface plasmon mode and a vibrational resonance could be seen using the Raman technique. A 1 μm layer of PMMA was spin coated on top of the gold grating. A schematic of the system is shown in figure 7.7 In conventional Raman spectroscopy fluorescence from metals usually leads to a high level of background noise that makes identification of Raman peaks difficult. To avoid this happening, in my experiments I used the technique called modulated Raman [101, 102]. Here, instead of single input wavelength, the modulated Raman has multiple input wavelengths over the span of pico wavelength. Later, the averaged of all the output signals

is calculated and thus it minimises the effect of noise. For this work, I have collaborated with Dr. Mingzohu and Prof. Kishan Dholakia of the St.Andrews University.

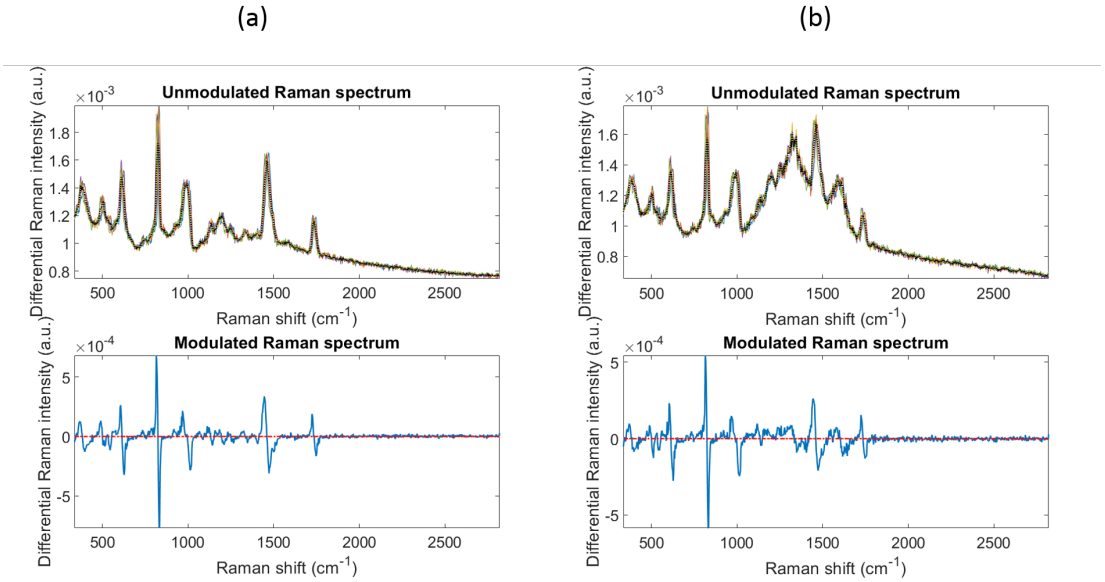

FIGURE 7.8: (a) Modulated Raman signal on top of the gold grating (b) Modulated Raman signal at the edge of gold/PMMA. The top row shows data using the unmodulated technique, the lower row shows data from the modulated-Raman approach.

Figure 7.8 shows some preliminary data, in the top row the data are based on the un-modulated (i.e. standard) Raman technique, the lower row shows the output from the modulated Raman. The laser wavelength used here is 785 nm. The modulated Raman signal at different positions on the sample was recorded every 500 nm along a line scan of the sample. Figure 7.8 (a) shows the modulated Raman signal when the laser is on the metal regions. Only features of the PMMA vibrational modes are present. However, when the laser is at the edge of a metal region, then the an additional peak appears somewhere between 1450 cm^{-1} and 1730 cm^{-1} in figure 7.8 (b). Perhaps this appears due to strong coupling between the vibrational mode and the plasmonic mode because in these regions (edge of metal film) the electric field intensity of the

plasmon mode is expected to be greatest. These are the preliminary results, to understand the system better, further research is required.

7.4 Three cavity system

Three cavity system allows the on-off switching of the coupling rate without perturbing the emitter and without introducing frequency chirps on the emitted photons. This can be used to control Rabi oscillations and also as a gain-modulation method in lasers. Coupling of three in-line cavities with molecular vibration placed in the central cavity (target cavity) is demonstrated below. Similar work has been previously shown by Robert Johne *et al.* [103] theoretically.

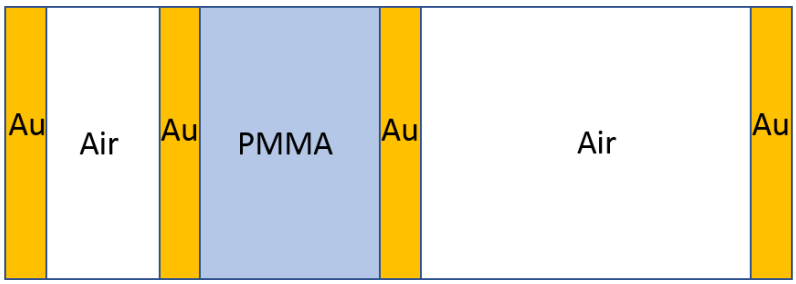

FIGURE 7.9: Schematic of three cavity system is shown. Δ is varied for first and last block.

A schematic of the three cavity system is shown in figure 7.9. Here, PMMA is in the central cavity. Air is used as the spacer in the first and last cavities. Here, I am assuming the frequency of the outer two cavities as $\omega_{l,r}$= ω_t+Δ, where detuning Δ is same for both but a different sign. First I will start will empty three cavity system.

The Hamiltonian for the empty three cavity system is,

$$H_{triplecavity} = \begin{pmatrix} (\omega_t + \Delta) - i\kappa_l & \eta & 0 \\ \eta & \omega_t - i\kappa_t & \eta \\ 0 & \eta & (\omega_t - \Delta) - i\kappa_r \end{pmatrix} \tag{7.1}$$

where, K_r, l, t are the loss rate of the left, the right and the target cavity. η denotes the coupling rate between the adjacent cavities.

Figure 7.10 shows calculated transmission spectra of three cases. In the first case, the value of Δ is kept zero. Thus I observe three peak positions in blue as expected. Second case when Δ is 100 nm. The central peak remains at the same position while the other two peaks shift slightly further away and similar pattern can be observed for the third case when Δ is 200 nm.

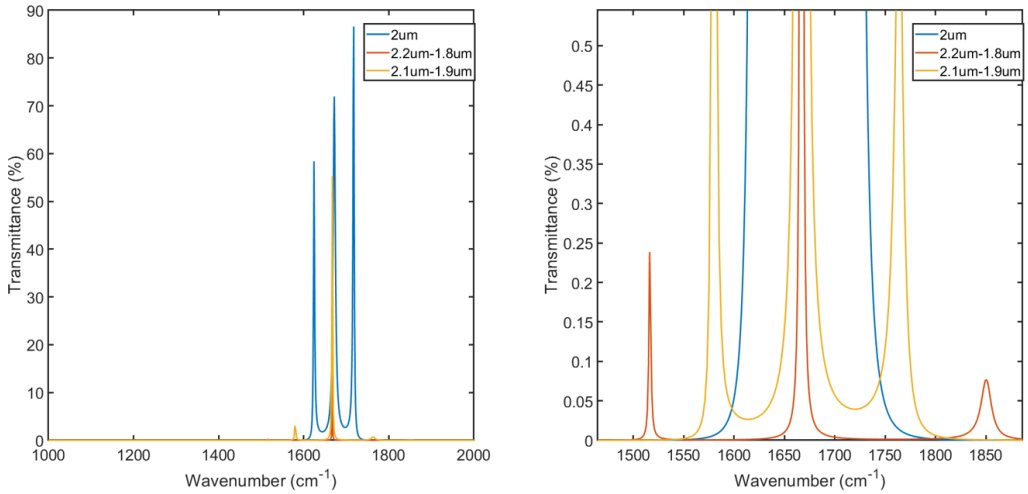

FIGURE 7.10: (a) Transmission spectra of at zero angle. The thickness of gold mirror were kept constant. Three cases 1) PMMA thickness is constant and is 2 μm 2) PMMA thickness of first block is 1.9 μm, 2 μm for the middle block and 2.1 μm for the last block 3) PMMA thickness of first block is 1.8 μm, 2 μm for the middle block and 2.2 μm for the last block (b) Zoomed in version of (a)

A good next step might be to measure the calculated transmission spectra with the vibrational mode inside the central cavity. Then experiments could be

done to verify the numerical calculation.

7.5 Summary

In this chapter, I discussed various ideas which due to insufficient time were remain unfinished. I started with vibrational strong coupling involved in photochromic molecules in the midinfrared region. Photochromic molecules change intensity of their vibrational modes if they are in continuously contact with UV light. Later, I mentioned that we can increase the extent of strong coupling by choosing different materials which have strong vibrational modes close to each other. By that, we could easily extend the strong coupling. Finally, I talked about modulated Raman spectroscopy technique. Traditional Raman spectroscopy faces lots of problem due to background noise from metals. To reduce the background noise and to understand the signal better,

In the next chapter I will summarise all the chapters and the work done in the thesis.

Chapter 8

Summary

In summary, this thesis has presented experimental as well as calculation-based investigations of hybridisation of multiple vibrational modes using confined light fields, vibrational strong coupling with surface plasmons, including the presence of surface plasmon stop bands, and finally strong coupling involving modes beyond the light-line.

In chapter 2, I focused on fundamentals. I started with Surface plasmon and then discussed about various way to couple surface plasmon polaritons with emitters. Later, I discussed about Drude-Lorenz model for metallic and non-metallic such as polymer materials.

Chapter3 was mainly focused on different experiment techniques which were used during my PhD period. In the end of the chapter, I discussed thoroughly different sections in comsol with an example.

In chapter 4, my results showed that distinct molecular vibrational resonances, here associated with C=O, CH_2 and CH_3 may be hybridized by strong coupling each of them to the same cavity/plasmon mode. The extent to which the three vibrational resonances contribute to the upper middle polariton in the cavity system, $\sim 11\%$, is comparable to that in the first report of hybridizing two excitonic resonances via strong coupling [19]. For the case of the plasmon

mode I found that only the coupling with the C=O bond fully met the strong coupling criteria, and that the associated polariton, although involving all three molecular resonances, only did so to the extent of 5%. Nonetheless, it is clear that strong coupling can hybridize multiple different molecular resonances of a single molecular unit, and that consequently strong coupling offers an interesting means by which to control molecular systems. Hybridized vibrational resonances may also be interesting in the context of vibrationally dressed states [12, 69]. A challenge for the strong coupling community is to devise means by which to increase the extent of hybridization possible. Some discussion of this was given in Chapter 7. Increasing the extent of hybridization might be achieved by employing confined light fields that exhibit greater field enhancement than the planar metal-clad cavity used here. Possible routes to achieving this include planar cavities that use dielectric stacks rather than metal mirrors [70], and localised resonances [39]. Care will be needed though since there is often a trade-off between field enhancement and cavity volume to consider [71].

In chapter 5, I demonstrated strong coupling between molecular vibrational resonances and surface plasmons in the infrared by exploiting grating coupling. In addition to enabling light to be coupled to the hybrid vibro-plasmon polaritons, the grating nature of the surface I used also led to the formation of polariton stop bands. I further showed that both upper and lower stop bands undergo strong coupling. A future study might extend my understanding by exploring the role of 2D periodic structures, e.g. to provide a full band gap. It would be interesting for example to see what would happen if such a gap was centred around the frequency of the molecular vibrational resonance, would the strong coupling be completely blocked? Finally I might add that although I have used a stripe array, a metal film with a modulated surface profile should

also work [78], therefore enabling, for example, electrical access. These initial results on strong coupling involving plasmon band edges would benefit from a more detailed investigation.

In chapter 6, my results showed that in addition to the usual cavity mode of metal-clad cavities, strong coupling also arises due to the coupled plasmon modes present in such structures. My results indicate that this mode should be taken into account when looking at how strong coupling may be used to alter/create molecular properties via strong coupling. Vibrational strong coupling provides an interesting alternative to explore a hierarchical approach that mixes both plasmonic and vibrational resonances something I discussed in Chapter 7.

To conclude, a number of advances in our understanding of strong coupling between confined light fields and molecular vibrational resonances have been made, and routes for follow-up investigations identified. It is to be hoped that these new avenues will be explored soon.

Appendix A

Matlab codes

A.1 COMSOL dispersion plot code

```
clear all
%figure()
h=4.135667516e-15;
c=3e8;
n_si=3.48;
n_air=1;
grating = 4500*10^-7; %Grating constant in centi-metres
%k_g= pi/grating;
%period=2*pi/grating;
k_g=1/grating;
%wpmma=1742;

%data = importdata('D:\daily progress\comsol\paper3\4.5um ...
    pitch-1.5um pmma_Ian_new.txt');

data = importdata('D:\daily ...
    progress\comsol\zns_ge_pmma_beyond_light_line.txt');
Nx = length(unique(data(:,1)));
%Nxx=unique(data(:,1));
```

```
18 %Nxx1=unique(data(:,1)):4:96;
19 Ny = length(unique(data(:,2)));
20
21 frequency = h.* data(:,2);% time being
22 kx=sin( data(:,1));
23 y=(data(:,2)./c)*0.01;
24 x=kx.*y;
25 x1=(kx./3.48).*y;
26 sin_x = ((2.*pi.*data(:,2)./c)) .*sin(data(:,1).*pi/180 );
27
28 X = reshape(sin_x,Ny,Nx);
29 %X = reshape(x,Ny,Nx);
30 Y = reshape((data(:,2)./c)*0.01,Ny,Nx);
31 YPMMA=1730;
32 Z = reshape(data(:,3),Ny,Nx);
33
34 %waterfall (X,Y,Z)
35 figure
36  hold on
37  disp_pos= surface(X,Y,Z, 'EdgeColor','none');
38   cl = colorbar;
39   cl.Label.String = 'Transmission';
40   cl.Label.FontWeight = 'bold';
41  disp_neg = surface(-X,Y,Z, 'EdgeColor','none'); %dispersion ...
       for -kx
42
43
44  hold on
45 z_max = max(max(get( disp_pos,'Zdata')));
46
47  % light lines
48
49   x1=-100000:1:100000;
```

```
%

%air
%
%plot(k_g)
% %air_light line
    plot(-(x1-k_g),x1)
    plot(x1-k_g,x1)
%
% %plot(-(x1-k_g),x1,z_max*ones(1,x1))
%
% %plot(-(x1-k_g),x1)
% %plot(x1-k_g,x1)
%
% %si
     plot(-(x1*3.48-k_g),x1)
     plot(x1*3.48-k_g,x1)
% % % % % %
     plot(-(x1*3.48-2*k_g),x1)
     plot(x1*3.48-2*k_g,x1)
% % % % %
     plot(-(x1*3.48-3*k_g),x1)
     plot(x1*3.48-3*k_g,x1)
% % % % %
     plot(-(x1*3.48-4*k_g),x1)
     plot(x1*3.48-4*k_g,x1)
% % %
    plot(-(x1*3.48-5*k_g),x1)
    plot(x1*3.48-5*k_g,x1)
%
 %C=O line
% max_Z = max(Z(:));
% pmma_x = -10000:1:10000;
```

```
% pmma = 1740*ones(1,length(pmma_x));
% pmma_z = max_Z*ones(1,length(pmma_x));

% %
%

%title(strcat('1D-Au 100nm-4.5um',x))
% xlabel('in-plane wavevector k_x/ m^{-1}') % x-axis label
% ylabel('Circular Frequency \omega / rad s^{-1}') % y-axis label
 xlabel(' k_x/2\pi ...
     (cm^{-1})','FontSize',16,'FontWeight','bold') % x-axis label
 xt= get (gca, 'XTick');
 set (gca, 'FontSize', 14,'FontWeight','bold');
 ylabel('Wavenumber ...
     (cm^{-1})','FontSize',16,'FontWeight','bold') % y-axis label
 %surf(peaks)
 set(gcf,'PaperPositionMode','auto')
% end points for light-line
 P1 = [-22222,0,3];
 P2 = [0,22222,3];

  pts = [P1; P2];
% %
%  plot3(pts(:,1), pts(:,2), ...
    pts(:,3),'Color','white','LineWidth',1);
% %

%
% max_Z = max(Z(:));
%  pmma_x = -2000:1:2000;
%
%  pmma = 1730*ones(1,length(pmma_x));
%   pmma1 = 1444*ones(1,length(pmma_x));
```

```
113 %      %pmma2 = 1697*ones(1,length(pmma_x));
114 %       %pmma3 = 1668*ones(1,length(pmma_x));
115 %
116 %  pmma_z = max_Z*ones(1,length(pmma_x));
117 %
118 %   xlim([-2000 2000])
119 %   ylim([1300 2000])
120
121 %angle2=linspace(0,60,500);
122 %cavity_mode_func = 1503.5+0.094*angle2.^2;
123
124 %k=cavity_mode_func.*sin(pi*angle2/180);
125 %k1=(((2*pi).*(cavity_mode_func)).*sin(pi*angle/180))./(2*pi);
126
127 %plot(k,cavity_mode_func);
128 %hold on
129 %plot(-k,cavity_mode_func);
130  set(gca,'linewidth', 2,'fontsize',24)
131    xlim([-2000 2000])
132    ylim([1300 2000])
133    view([180 -90])
```

A.2 FTIR dispersion plot code

```
clear all;
path('D:\daily progress\FTIR\4.7um_longer_angle')
h=4.135667516e-15; %h/e
c=3e10;
c1=3e8/10^-9;
n_si=3.43;
n_air=1;
n_sub = 1.0;
grating = 400e-9;
kx_to_ev = h*c*n_sub*1e6./(1*2*pi);
k_g = h*c./(1*grating);


core = 'au100nm-pmma1um-pitch4.7um-angle';
ext = '.0.dpt';

x='-transmission';


dataSet = 1;

angleMin = 0;
angleMax = 30;
angleStep =2;
angles = [];


raw = [];
dataSet = 0;

```

```
31 for jj = angleMin:angleStep:angleMax
32   dataSet = dataSet + 1;
33
34   %dynamically create the filename to be loaded
35   myfilename = sprintf(strcat(core,'%i',ext), jj);
36
37   %store the relevant angle
38   angles(dataSet) = jj;
39
40   %load the datafile
41   raw(:,:,dataSet) = importdata(myfilename);
42 end
43
44
45 numAngles = dataSet;
46
47
48 numK = size(raw,1);
49
50 angles
51
52
53 freqArr = zeros(numK, numAngles);
54 wavevectorArr = zeros(numK, numAngles);
55 transmissionArr = zeros(numK, numAngles);
56
57
58 for i = 1:numK
59     for j = 1:numAngles
60         freqArr(i,j) = raw(i,1,j);
61     end
62 end
63
```

```
64 %Wavevector; this is a function of both angle and kSpec.
65 for i = 1:numK
66     for j = 1:numAngles
67         wavevectorArr(i,j) = freqArr(i,j)*sind(angles(j));
68     end
69 end
70
71 %Transmission assignment
72 for i = 1:numK
73     for j = 1:numAngles
74        transmissionArr(i,j) = raw(i,2,j);
75     end
76 end
77
78
79 kx_max = max(wavevectorArr(i,j));
80 %kx_min = min(k_x_all);
81 ev_max = max(freqArr(i,j));
82 ev_min = min(freqArr(i,j));
83 %z_max = max(max(get( transmissionArr,'Zdata')));
84 %hold all;
85
86
87  xlim([-2000 2000])
88  ylim([1000 3000])
89  freqAr=transpose(freqArr);
90  freqA= freqAr(:,1);
91
92
93
94 hold on
95 disp_pos=surface(wavevectorArr, freqArr,(transmissionArr ...
      ),'EdgeColor','none');
```

```
96 disp_neg=surface(-wavevectorArr, ...
       freqArr,(transmissionArr),'EdgeColor','none');
97
98
99 x=-2000:10:2000;
100 y=1000:5:3000;
101 height_pos = get(disp_pos,'ZData'); %lower +kx dispersion ...
       plot so lines are visible
102 set(disp_pos,'ZData',height_pos-10)
103 height_neg = get(disp_neg,'ZData'); %and for -kx
104 set(disp_neg,'ZData',height_neg-10)
105 kx = linspace(-kx_max,kx_max);
106 ev_0 = abs(kx_to_ev*kx);
107 plot(kx,ev_0)
108 %+1
109 ev_p1 = abs(kx_to_ev*kx+k_g);
110 plot(kx,ev_p1,'color','m')
111 %-1
112 ev_n1 = abs(kx_to_ev*kx-k_g);
113 plot(kx,ev_n1,'color','m')
114 %+2
115 ev_p2 = abs(kx_to_ev*kx+2*k_g);
116 plot(kx,ev_p2,'color','m')
117 %-2
118 ev_n2 = abs(kx_to_ev*kx-2*k_g);
119 plot(kx,ev_n2,'color','m')
120
121
122 shading interp;
123
124
125
126 %colorbar & settings
```

```
127  cl = colorbar;
128  cl.Label.String = 'Transmission';
129
130 %axes & title
131 %title(strcat('1D-Au 100nm-4.625um',x))
132 % xlabel('in-plane wavevector k_x/ m^{-1}') % x-axis label
133 % ylabel('Circular Frequency \omega / rad s^{-1}') % y-axis label
134 xlabel(' k_x /cm^{-1}','FontSize',16,'FontWeight','bold') % ...
      x-axis label
135 xt= get (gca, 'XTick');
136 set (gca, 'FontSize', 14,'FontWeight','bold');
137 ylabel('Wavenumber ...
      (cm^{-1})','FontSize',16,'FontWeight','bold') % y-axis label
138 hold off;
```

Bibliography

1. Kasprzak, J. *et al.* Bose-Einstein condensation of exciton polaritons. *Nature* **443,** 409–414. ISSN: 1476-4687. https://doi.org/10.1038/nature05131 (2006).
2. Skolnick, M. S. *et al.* Strong coupling phenomena in quantum microcavity structures. *Semiconductor Science and Technology* **13,** 645–669. https://doi.org/10.1088%2F0268-1242%2F13%2F7%2F003 (1998).
3. Fernandez, H. A. *et al.* Electrically tuneable exciton energy exchange between spatially separated 2-dimensional semiconductors in a microcavity. *Applied Physics Letters* **115,** 071103. eprint: https://doi.org/10.1063/1.5110492. https://doi.org/10.1063/1.5110492 (2019).
4. Dovzhenko, D. S. *et al.* Light–matter interaction in the strong coupling regime: configurations, conditions, and applications. *Nanoscale* **10,** 3589–3605. http://dx.doi.org/10.1039/C7NR06917K (8 2018).
5. Shalabney, A. *et al.* Coherent coupling of molecular resonators with a microcavity mode. *Nature Communications* **6,** 1–6. ISSN: 2041-1723. http://dx.doi.org/10.1038/ncomms6981 (2015).
6. Ebbesen, T. W. Hybrid Light–Matter States in a Molecular and Material Science Perspective. *Accounts of Chemical Research* **49,** 2403–2412 (2016).
7. Herrera, F. *et al.* Cavity-Controlled Chemistry in Molecular Ensembles. *Physical Review Letters* **116,** 238301 (2016).

8. Bennett, K. *et al.* Novel photochemistry of molecular polaritons in optical cavities. *Faraday Discussions* **194,** 259–282 (2016).
9. Feist, J. *et al.* Polaritonic Chemistry with Organic Molecules. *ACS Photonics* **5,** 205–216. ISSN: 2330-4022. http://dx.doi.org/10.1021/acsphotonics.7b00680 (2017).
10. Ribeiro, R. F. *et al.* Polariton chemistry: controlling molecular dynamics with optical cavities. *Chemical Science* **9,** 6325–6339 (2018).
11. Hutchison, J. A. *et al.* Modifying Chemical Landscapes by Coupling to Vacuum Fields. *Angewandte Chemie International Edition* **51,** 1592–1596. ISSN: 1433-7851. http://dx.doi.org/10.1002/anie.201107033 (2012).
12. Galego, J. *et al.* Cavity-Induced Modifications of Molecular Structure in the Strong-Coupling Regime. *Physical Review X* **5,** 041022 (2015).
13. Schwartz, T. *et al.* Reversible Switching of Ultrastrong Light-Molecule Coupling. *Physical Review Letters* **106,** 196405 (2011).
14. Feist, J. *et al.* Extraordinary Exciton Conductance Induced by Strong Coupling. *Physical Review Letters* **114,** 196402 (2015).
15. Coles, D. M. *et al.* Polariton-mediated energy transfer between organic dyes in a strongly coupled optical microcavity. *Nature Materials* **13,** 712–719 (2014).
16. Zhong, X. *et al.* Non-Radiative Energy Transfer Mediated by Hybrid Light-Matter States. *Angewandte Chemie International Edition* **55,** 6202–6206 (2016).
17. Georgiou, K. *et al.* Control over Energy Transfer between Fluorescent BODIPY Dyes in a Strongly Coupled Microcavity. *ACS Photonics* **5,** 258–266 (2017).
18. Zhong, X. *et al.* Energy Transfer between Spatially Separated Entangled Molecules. *Angewandte Chemie International Edition* **56,** 9034–9038 (2017).

19. Lidzey, D. G. *et al.* Photon-Mediated Hybridization of Frenkel Excitons in Organic Semiconductor Microcavities. *Science* **288,** 1620–1623 (2000).
20. Slootsky, M. *et al.* Room Temperature Frenkel-Wannier-Mott Hybridization of Degenerate Excitons in a Strongly Coupled Microcavity. *Physical Review Letters* **112,** 076401 (2014).
21. Baieva, S. *et al.* Strong coupling between surface plasmon polaritons and -carotene in nanolayered system. *The Journal of Chemical Physics* **138,** 044707 (2013).
22. Vakevainen, A. I. *et al.* Plasmonic surface lattice resonances at the strong coupling regime. *Nano Letters* **14,** 1721–1727 (2014).
23. Long, J. P. *et al.* Coherent coupling between a molecular vibration and Fabry-Perot optical cavity to give hybridised states in the strong coupling limit. *ACS Photonics* **2,** 130–136 (2015).
24. Simpkins, B. S. *et al.* Spanning Strong to Weak Normal Mode Coupling between Vibrational and Fabry–Pérot Cavity Modes through Tuning of Vibrational Absorption Strength. *ACS Photonics* **2,** 1460–1467 (2015).
25. Vergauwe, R. M. A. *et al.* Quantum Strong Coupling with Protein Vibrational Modes. *The Journal of Physical Chemistry Letters* **7,** 4159–4164 (2016).
26. Muallem, M. *et al.* Strong light-matter coupling between a molecular vibrational mode in a PMMA film and a low-loss mid-IR microcavity. *Annalen der Physik* **528,** 313–320 (2015).
27. Dunkelberger, A. D. *et al.* Modified relaxation dynamics and coherent energy exchange in coupled vibration-cavity polaritons. *Nature Communications* **7** (2016).
28. Memmi, H. *et al.* Strong coupling between surface plasmon polaritons and molecular vibrations. *Physical Review Letters* **118,** 126802 (2017).

29. Ahn, W. *et al.* Vibrational Strong Coupling Controlled by Spatial Distribution of Molecules within the Optical Cavity. *ACS Photonics* **5,** 158–166 (2017).
30. Chervy, T. *et al.* Vibro-Polaritonic IR Emission in the Strong Coupling Regime. *ACS Photonics* **5,** 217–224 (2017).
31. Casey, S. R. *et al.* Vibrational Strong Coupling of Organometallic Complexes. *The Journal of Physical Chemistry C* **120,** 28138–28143 (2016).
32. George, J. *et al.* Liquid-Phase Vibrational Strong Coupling. *The Journal of Physical Chemistry Letters* **6,** 1027–1031 (2015).
33. Hertzog, M. *et al.* Voltage-Controlled Switching of Strong Light-Matter Interactions using Liquid Crystals. *Chemistry - A European Journal* **23,** 18166–18170 (2017).
34. Thomas, A. *et al.* Ground-State Chemical Reactivity under Vibrational Coupling to the Vacuum Electromagnetic Field. *Angewandte Chemie* **128,** 11634–11638 (2016).
35. Dunkelberger, A. D. *et al.* Ultrafast Transmission Modulation and Recovery via Vibrational Strong Coupling. *The Journal of Physical Chemistry A* **122,** 965–971 (2018).
36. Xiang, B. *et al.* Two-dimensional infrared spectroscopy of vibrational polaritons. *Proceedings of the National Academy of Sciences* **115,** 4845–4850 (2018).
37. Dorfman, K. E. *et al.* Multidimensional photon correlation spectroscopy of cavity polaritons. *Proceedings of the National Academy of Sciences* **115,** 1451–1456 (2018).
38. Plumhof, J. D. *et al.* Room-temperature Bose-Einstein condensation of cavity exciton-polaritons in a polymer. *Nature Materials* **13,** 247. https://doi.org/10.1038/nmat3825 (2013).

39. Wan, W. *et al.* Strong coupling between mid-infrared localized plasmons and phonons. *Optics Express* **24,** 12367 (2016).

40. Barnes, W. L. *et al.* Physical origin of photonic energy gaps in the propagation of surface plasmons on gratings. *Physical Review B* **54,** 6227–6244 (1996).

41. Andrew, P. *et al.* Surface-plasmon energy gaps and photoabsorption. *Journal of Modern Optics* **44,** 395–406 (1997).

42. Kitson, S. C. *et al.* Surface-plasmon energy gaps and photoluminescence. *Physical Review B* **52,** 11441–11445 (1995).

43. Lidzey, D. G. *et al.* Strong exciton-photon coupling in an organic semiconductor microcavity. *Nature* **395,** 53 EP –. https://doi.org/10.1038/25692 (1998).

44. Muallem, M. *et al.* Strong Light-Matter Coupling and Hybridization of Molecular Vibrations in a Low-Loss Infrared Microcavity. *The Journal of Physical Chemistry Letters* **7,** 2002–2008 (2016).

45. Flatten, L. C. *et al.* Electrically tunable organic–inorganic hybrid polaritons with monolayer WS2. *Nature Communications* **8,** 14097 (2017).

46. Shahbazyan, T. V. Exciton–Plasmon Energy Exchange Drives the Transition to a Strong Coupling Regime. *Nano Letters,* DOI:10.1021/acs.nanolett.9b00827 (2019).

47. Törmä, P. *et al.* Strong coupling between surface plasmon polaritons and emitters: a review. *Reports on Progress in Physics* **78,** 013901 (2015).

48. Ebbesen, T. W. Hybrid Light–Matter States in a Molecular and Material Science Perspective. *Accounts of Chemical Research* **49.** PMID: 27779846, 2403–2412. eprint: https://doi.org/10.1021/acs.accounts.6b00295. https://doi.org/10.1021/acs.accounts.6b00295 (2016).

49. Yu, X. *et al.* Strong Coupling in Microcavity Structures: Principle, Design, and Practical Application. *Laser & Photonics Reviews* **13,** 1800219. eprint:

https://onlinelibrary.wiley.com/doi/pdf/10.1002/lpor.201800219. https://onlinelibrary.wiley.com/doi/abs/10.1002/lpor.201800219 (2019).

50. Jackson, J. D. *Classical electrodynamics* 3rd ed. ISBN: 9780471309321. http://cdsweb.cern.ch/record/490457 (Wiley, New York, NY, 1999).
51. Oughstun, K. E. *et al.* On the Lorentz-Lorenz formula and the Lorentz model of dielectric dispersion. *Opt. Express* **11,** 1541–1546. http://www.opticsexpress.org/abstract.cfm?URI=oe-11-13-1541 (2003).
52. Törmä, P. *et al.* Strong coupling between surface plasmon polaritons and emitters: a review. English. *Reports on Progress in Physics* **78,** 1–34. ISSN: 0034-4885 (2015).
53. Agranovich, V. M. *et al.* Cavity polaritons in microcavities containing disordered organic semiconductors. *Phys. Rev. B* **67,** 085311. https://link.aps.org/doi/10.1103/PhysRevB.67.085311 (8 2003).
54. Wang, S. *Strong light-molecule coupling : routes to new hybrid materials* PhD thesis (Theoretical and/or physical chemistry, Université de Strasbourg, 2015).
55. Olmon, R. L. *et al.* Optical dielectric function of gold. *Physical Review B* **86,** 235147 (2012).
56. Edwards. in (ed Palik, E.) 547–569 (Academic Press Inc., 1985).
57. Malitson, I. H. A redetermination of some optical properties of calcium fluoride. *Applied Optics* **2,** 1103–1107 (1963).
58. Gaffney, J. S. *et al.* in *Characterization of Materials* 1–33 (American Cancer Society, 2012). ISBN: 9780471266969. eprint: https://onlinelibrary.wiley.com/doi/pdf/10.1002/0471266965.com107.pub2. https://onlinelibrary.wiley.com/doi/abs/10.1002/0471266965.com107.pub2.
59. To, I. Introduction to COMSOL Multiphysics.

60. *Electromagnetic interactions in one-dimensional metamaterials* PhD thesis (University of Exeter, author = Seetharaman, Sathya Sai, year = 2018).
61. Crum, V. F. *et al.* Photon-mediated hybridization of molecular vibrational states. *Physical Chemistry Chemical Physics* **20,** 850–857 (2018).
62. Dintinger, J. *et al.* Strong coupling between surface plasmon-polaritons and organic molecules in subwavelength hole arrays. *Physical Review B* **71** (2005).
63. Nagai, H. Infrared spectra of stereoregular plymethyl methacrylate. *Journal of Applied Polymer Science* **7,** 1697–1714 (1963).
64. Luxmoore, I. J. *et al.* Graphene–Metamaterial Photodetectors for Integrated Infrared Sensing. *ACS Photonics* **3,** 936–941 (2016).
65. Bellessa, J. *et al.* Strong Coupling between Surface Plasmons and Excitons in an Organic Semiconductor. *Physical Review Letters* **93,** 036404 (2004).
66. Hooper, I. R. *et al.* in (eds Richardson, N. V. *et al.*) chap. 4 (Elsevier BV, 2014).
67. Vasa, P. *et al.* Real-time observation of ultrafast Rabi oscillations between excitons and plasmons in metal nanostructures with J-aggregates. *Nature Photonics* **7,** 128–132 (2013).
68. Tropf, L. *et al.* Investigating the Onset of the Strong Coupling Regime by Fine-Tuning the Rabi Splitting in Multilayer Organic Microcavities. *Advanced Optical Materials* **6,** 1800203 (2018).
69. Herrera, F. *et al.* Theory of Nanoscale Organic Cavities: The Essential Role of Vibration-Photon Dressed States. *ACS Photonics* **5,** 65–79 (2017).
70. Kapon, O. *et al.* Vibrational Strong Light–Matter Coupling Using a Wavelength-Tunable Mid-infrared Open Microcavity. *The Journal of Physical Chemistry C* **121,** 18845–18853 (2017).
71. Chikkaraddy, R. *et al.* Single-molecule strong coupling at room temperature in plasmonic nanocavities. *Nature* **535,** 127–130 (2016).

72. Bisht, A. *et al.* Collective Strong Light-Matter Coupling in Hierarchical Microcavity-Plasmon-Exciton Systems. *Nano Letters* **19,** 189–196 (2018).
73. Ricthie, R. H. *et al.* Surface-plasmon resonance effect in grating diffraction. *Physical Review Letters* **21,** 1530–1533 (1968).
74. Rodriguez, S. *et al.* Surface lattice resonances strongly coupled to Rhodamine 6G excitons: tuning the plasmon-exciton-polariton mass and composition. *Optics Express* **21,** 27411 (2013).
75. Wang, W. *et al.* The rich photonic world of plasmonic nanoparticle arrays. *Materials Today* **21,** 303–314 (2018).
76. Kravets, V. G. *et al.* Plasmonic Surface Lattice Resonances: A Review of Properties and Applications. *Chemical Reviews* **118,** 5912–5951. ISSN: 1520-6890. http://dx.doi.org/10.1021/acs.chemrev.8b00243 (2018).
77. Moilanen, A. J. *et al.* Active Control of Surface Plasmon–Emitter Strong Coupling. *ACS Photonics* **5,** 54–64 (2017).
78. Chang, Y. *et al.* Strong and weak coupolings in molecular vibration-plasmon hybrid structures. *Optics Express* **27,** 1479–1487 (2019).
79. Savona, V. *et al.* Exact quantum calculation of polartion dispersion in semiconductor microcavities. *Solida State Communications* **95,** 673–678 (1995).
80. Agranovich, V. M. *et al.* Cavity polaritons in microcavities containing disordered organic semiconductors. *Physical Review B* **67,** 085311 (2003).
81. Arena, A. *et al.* Silicon-based organic-inorganic microcavity and its dispersion curve from angle-resolved photoluminescence. *Applied Physics Letters* **72,** 2571–2573 (1998).
82. Smith, L. H. *et al.* Field profiles of coupled surface plasmon-polaritons. *Journal of Modern Optics* **55,** 2929–2943. eprint: https://doi.org/10.1080/09500340802271250. https://doi.org/10.1080/09500340802271250 (2008).

83. Lei, D. Y. *et al.* Revealing Plasmonic Gap Modes in Particle-on-Film Systems Using Dark-Field Spectroscopy. *ACS Nano* **6.** PMID: 22256972, 1380–1386. eprint: https://doi.org/10.1021/nn204190e. https://doi.org/10.1021/nn204190e (2012).

84. Gramotnev, D. K. *et al.* Nanofocusing of electromagnetic radiation. *Nature Photonics* **8,** 13–22 (2013).

85. Li, G.-C. *et al.* Plasmonic particle-on-film nanocavities: a versatile platform for plasmon-enhanced spectroscopy and photochemistry. *Nanophotonics* **7,** 1865–1889 (2018).

86. Baumberg, J. J. *et al.* Extreme nanophotonics from ultrathin metallic gaps. *Nature Materials* **18,** 668–678 (2019).

87. Economou, E. N. Surface plasmons in thin films. *Physical Review* **182,** 539–554 (1969).

88. Kurokawa, Y. *et al.* Metal-insulator-metal plasmon nanocavities: Analysis of optical properties. *Phys. Rev. B* **75,** 035411. https://link.aps.org/doi/10.1103/PhysRevB.75.035411 (3 2007).

89. Dionne, J. A. *et al.* Plasmon slot waveguides: Towards chip-scale propagation with subwavelength-scale localization. *Physical Review B* **73** (2006).

90. Chikkaraddy, R. *et al.* Single-molecule strong coupling at room temperature in plasmonic nanocavities. *Nature* **535,** 127 EP –. https://doi.org/10.1038/nature17974 (2016).

91. Azzam, R. M. A. *et al. Ellipsometry and polarised light* (North-Holland (Amsterdam), 1977).

92. Menghrajani, K. S. *et al.* Vibrational strong coupling with surface plasmons and the presence of surface plasmon stop bands. *ACS Photonics* **0,** null. eprint: https://doi.org/10.1021/acsphotonics.9b00662. https://doi.org/10.1021/acsphotonics.9b00662 (0).

93. Wan, W. *et al.* Strong coupling between mid-infrared localized plasmons and phonons. *Opt. Express* **24,** 12367–12374. http://www.opticsexpress.org/abstract.cfm?URI=oe-24-11-12367 (2016).

94. Menghrajani, K. S. *et al.* Hybridization of Multiple Vibrational Modes via Strong Coupling Using Confined Light Fields. *Advanced Optical Materials* **0,** 1900403. eprint: https://onlinelibrary.wiley.com/doi/pdf/10.1002/adom.201900403. https://onlinelibrary.wiley.com/doi/abs/10.1002/adom.201900403.

95. Graf, A. *et al.* Near-infrared exciton-polaritons in strongly coupled single-walled carbon nanotube microcavities. *Nature Communications* **7** (2016).

96. Gao, W. *et al.* Continuous transition between weak and ultrastrong coupling through exceptional points in carbon nanotube microcavity exciton–polaritons. *Nature Photonics* **12,** 362–368 (2018).

97. Muallem, M. *et al.* Strong Light-Matter Coupling and Hybridization of Molecular Vibrations in a Low-Loss Infrared Microcavity. *The Journal of Physical Chemistry Letters* **7.** PMID: 27159242, 2002–2008. eprint: https://doi.org/10.1021/acs.jpclett.6b00617. https://doi.org/10.1021/acs.jpclett.6b00617 (2016).

98. Hanlon, E. B. *et al.* Prospects forin vivoRaman spectroscopy. *Physics in Medicine and Biology* **45,** R1–R59. https://doi.org/10.1088%2F0031-9155%2F45%2F2%2F201 (2000).

99. Kong, K. *et al.* Raman spectroscopy for medical diagnostics — From in-vitro biofluid assays to in-vivo cancer detection. *Advanced Drug Delivery Reviews* **89.** Pharmaceutical applications of Raman spectroscopy – from diagnosis to therapeutics, 121 –134. ISSN: 0169-409X. http://www.sciencedirect.com/science/article/pii/S0169409X15000447 (2015).

100. Shalabney, A. *et al.* Enhanced Raman Scattering from Vibro-Polariton Hybrid States. *Angewandte Chemie International Edition* **54,** 7971–7975.

eprint: https://onlinelibrary.wiley.com/doi/pdf/10.1002/anie.201502979. https://onlinelibrary.wiley.com/doi/abs/10.1002/anie.201502979 (2015).

101. Chen, M. *et al.* Depth-resolved multimodal imaging: Wavelength modulated spatially offset Raman spectroscopy with optical coherence tomography. *Journal of Biophotonics* **11.** e201700129 jbio.201700129, e201700129. eprint: https://onlinelibrary.wiley.com/doi/pdf/10.1002/jbio.201700129. https://onlinelibrary.wiley.com/doi/abs/10.1002/jbio.201700129 (2018).

102. Chen, M. *et al.* The Use of Wavelength Modulated Raman Spectroscopy in Label-Free Identification of T Lymphocyte Subsets, Natural Killer Cells and Dendritic Cells. *PLOS ONE* **10,** 1–14. https://doi.org/10.1371/journal.pone.0125158 (May 2015).

103. Johne, R. *et al.* Control of the electromagnetic environment of a quantum emitter by shaping the vacuum field in a coupled-cavity system. English. *Physical Review A : Atomic, Molecular and Optical Physics* **91,** 063807–1/5. ISSN: 1050-2947 (2015).